The Design and Validation of a Multi-Layer Model of Human Skin

A thesis submitted for the degree of

Doctor of Philosophy

of the Higher Education Authority of Ireland

by

Cormac Oliver Flynn

BE, MSME

Department of Mechanical and Electronic Engineering

School of Engineering

Institute of Technology, Sligo

April 2007

Supervisor

Dr B.A.O. McCormack

Contents

iv

List of Figures

List of Tables

Preface

This thesis describes original work, which has not been submitted for a degree at any other institution. The investigations were carried out in the Department of Mechanical and Electronic Engineering, Institute of Technology, Sligo, Ireland during the period November 2003 to March 2007, under the supervision of Dr Brendan A.O. McCormack.

Cormac Flynn
4th April 2007

Acknowledgements

I would like to express my sincere thanks to Dr Brendan McCormack for his continuous support and supervision throughout this project.

Many thanks also to Ger Reilly for advice and for ensuring that I was facilitated in terms of finance, software and equipment.

Thanks to Gordon Muir for technical advice and for producing the experimental rigs to a very high quality.

I am very grateful to Eamonn Price for making available the laser profilometer system and being able to help and advise me on its use at a moment's notice. Without him, I would be measuring the wrinkles with a metre stick.

Thanks to Ray Tobin for technical advice on the experimental equipment … and for passing the ball to me on occasion in indoor-soccer.

My thanks to Dr John Hession for advice received throughout my studies and for help with presentations. The knowledge gained on farming in Mayo is appreciated too.

Thanks to Anthony Kitchin and Brendan Murray for the supply of animal skin and John Comiskey for coming to the rescue on more than one occasion when there were printing emergencies.

Thanks to my colleagues in the research lab, both past and present: Shane O'Neill, Anthony Lang, Ashkan Safari, Hamid Khalili Parsa, Chan Yong Chun and Bahman Honori. The wide variety of backgrounds and the one or two international incidents made it an enjoyable and interesting environment to work in.

Sincerest thanks to Tara Peterson for the continuous support and friendship, especially when I hit the wall on more than one occasion.

Much appreciation goes out to my brothers and sisters – Ronan, Muiris, Meadhbh and Ciara. Their emotional support and belief in me ensured I reached the end without too many additional wrinkles on my face.

Finally, my thanks to my Mam and Dad. They have always supported me in anything I undertake, and for that, I am forever grateful.

Abstract

Human skin is a complex multi-layered material consisting of the epidermis, dermis and underlying hypodermis. For several decades, much effort has gone into the development of mathematical and computer models of skin. A physically accurate and realistic model of skin has applications in several diverse areas from artificial skin design to computer animation.

There are many numerical models of skin in existence, which accurately simulate several of the skin's complex mechanical characteristics. However, many of these models assume skin to be a homogeneous material and thus ignore the individual contribution of each layer. While these single-layer models may be adequate when simulating skin under homogeneous loading conditions, a multi-layer model is needed to simulate skin under more complex deformations such as wrinkling – a phenomenon common to all human skin.

A multi-layer finite element model of skin, consisting of the stratum corneum, dermis and hypodermis, has been proposed to simulate skin under deformations that cause it to wrinkle. The stratum corneum is represented by a neo-Hookean function, the dermis by an orthotropic-viscoelastic function and the hypodermis by a Yeoh strain energy function with a Prony series to model viscoelasticity. *In vivo* wrinkling experiments on volar forearm skin were conducted to validate the skin model.

Results from this study show that a model representing the stratum corneum, dermis and hypodermis more accurately simulates the wrinkling of skin than single-layer models. The three-layer model represents a significant improvement over existing single and two-layer models. The model shows that the natural tension or pre-stress in living skin plays a significant role in the formation of wrinkles – a larger pre-stress delays the initiation and reduces the size of the wrinkles. The model predicts that a stiffer stratum corneum and a greater collagen fibre density increase the size of wrinkles – occurrences that are observed in aging skin. The model also predicts that larger wrinkles occur when they are parallel to the Langer's lines in the skin.

The model has also been used to explore the wrinkle formation around contracting healing scars. Comparison between the results of finite element analyses and simplified experiments of contracting scars show that the pre-stress and the orthotropic nature of skin play a significant role in the orientation of the wrinkles.

Chapter 1

Preamble

Human skin, the outermost layer on the human body, has been the subject of many experiments since Langer (1861) punctured the skin of cadavers to study its anisotropic characteristics. The emergence of tissue biomechanics as a major research area in the 1960s saw the first mathematical models of skin (Lanir, 1987). Since then, analytical and numerical models of increasing sophistication have been developed to simulate various complex properties of skin measured in experiments. The development of accurate models of human skin is of benefit to several diverse areas of science and technology.

Skin models can guide in the design and development of artificial skin substitutes used to replace human skin lost due to (i) large body surface area burns; (ii) chronic wounds such as venous, diabetic and pressure ulcers; (iii) dermatological conditions; and (iv) surgical procedures such as the removal of malignant lesions (Ramos-e-Silva and Ribeiro de Castro, 2002). There are many skin substitutes on the market. They can be divided into materials that are totally non-biological, such as Opsite and Duoderm and those that have a presence of some biological component, such as Dermagraft, Transcyte, Alloderm and Integra (Jones *et al.*, 2002). The goal of any skin substitute would be to replicate the function of the real skin it is replacing. It is also important that the material mimics behaviour such as wrinkling when subject to small in-plane compressive stresses. This is particularly important in the case of facial skin substitutes used in maxillofacial surgery where wrinkling is the key to providing human-like realism (Bellamy *et al.*, 2003). The material and geometric properties of a model that simulates skin when stretched or wrinkled could be used as the inputs into the design of these skin substitutes. As well as developing artificial materials for skin replacement therapy, there is a strong need in the pharmaceutical industry to develop

in vitro substitutes for the design and testing of drug delivery devices such as hypodermic needles (Shergold *et al.*, 2006) or transdermal patches (Davis *et al.*, 2004). An accurate skin model would aid in the design of such substitutes.

There are a wide variety of incision and suturing techniques in use for conducting specific surgical procedures on different parts of the body. The techniques take into account many factors including the local orientation of the relaxed skin tension lines (Borges, 1989) and the physique of the patient (Lott-Crumpler and Chaudhry, 2001). A well-sutured surgical incision should result in well-healed wound with minimal scarring and loss of function. In some cases, such as chronic wounds, the healing process leads to an over-production of collagen, which can lead to contraction of the scar (Stadelmann *et al.*, 1998). Although this contraction process can be beneficial in reducing the size of the wound, it can cause cosmetic deformity of the surrounding skin. As well as being visually undesirable, the deformities can be an indication of adverse stress fields. Adverse stress fields and wrinkling in the region of the healing wound can lead to loss of blood circulation and an unsightly scar. A model that could accurately predict the behaviour of skin in the region of sutured incisions and healing wounds of varying shape in different areas of the body would be a useful tool. It would allow a surgeon to choose the optimum suture pattern that minimises the scarring from an incision in a specific area on a particular patient. The chosen incision and suturing technique is largely dependent on the acquired experience of the surgeon (Cerda, 2005). Such a tool would reduce the need for further operations to revise any undesirable scarring.

Another application of a human skin model is the area of surgery simulation used for training (Bro-Nielsen, 1998). A model that accurately replicates the behaviour of skin when it is cut with a scalpel would provide the training surgeon with a behavioural sense of reality. The model would also provide accurate input to the haptic interfaces used to simulate a physical sense of touch for the surgeon (Mahvash and Hayward, 2001). The development of surgery simulation allows for the possibility of telemedicine, where a surgeon could perform procedures on a patient located anywhere in the world.

Human skin is highly visible and considerable aesthetic value is attributed to it. Consequently, people put significant effort into maintaining the appearance of their skin. Over 21 billion dollars were spent on cosmetic products worldwide in 2001 (Kumar, 2005). Moisturisers are applied; hyaluronic acid and botulinum toxin A

(Botox) are injected; and lasers are used to remove or reduce the appearance of wrinkles (Koch, 1997; Moore, 2002). Cosmetic surgical procedures such as face-lifts and blepharoplasties are carried out to remove sagging or excess skin in the facial area. The different types of wrinkles have different causes and so it is necessary to have different treatment protocols for them (Pierard *et al.*, 2003). An accurate physical model of skin could be used to study the wrinkling and aging of skin. The mechanical properties and geometries of each layer in the model could be varied to study the effects they have on the wrinkling of skin. The effect of prestress on the development of wrinkles in the skin can also be quantified. These insights could aid in the development of more effective cosmetic products and techniques to reduce wrinkling. In plastic surgery, the patient-specific data could be input into the model to plan the best approach for a procedure.

Human skin models can be of use in the field of forensic science. Recent finite-element models simulate gunshot injuries to the cranium but they ignore skin and other soft tissues (Mota *et al.*, 2003). Skin would have a dissipative effect on the energy from the impact of the bullet. Physical artificial models have been developed to analyse gunshot and blunt object trauma to the human heads (Thali *et al.*, 2002a; 2002b; 2002c). Finite element simulations consisting of skin models would complement and extend the results of such physical models. Indeed, computer models could be used to analyse scenarios that are too difficult to set up in a laboratory. Such models could aid in the forensic analysis of bite-marks on victims, which are sometimes used to convict or exonerate a suspect (Atsu *et al.*, 1998). Bite-marks are a result of a dynamic process where the teeth, skin, biter and victim are all moving simultaneously. Thali *et al.* (2003) stated that the two-dimensional techniques, which are most commonly used to analyse bite-marks, introduce distortion and therefore three-dimensional techniques should be employed. A three-dimensional multi-layer model of skin could be a valuable tool in such analyses. Accurate models could also aid in the reconstruction of faces from skeletal remains. Traditional techniques involve the construction of a physical clay model. The time required to complete such a model is on the order of weeks. Many existing computer modelling techniques use purely geometric methods to build a reconstruction of the face (Kahler *et al.*, 2003; Subke *et al.*, 2006). Facial features such as wrinkles are added in an artistic fashion. Including the physical properties of the skin in such models could improve the reconstruction and aid in the identification process.

3

There is a vast array of consumer products that interact with the human skin in some fashion. As the cost of computers decrease and their computational power increases, there is a growth in the use of computer models to aid in the design and development of these products (Murrell, 2006). An example of such a product is the feminine pad, which is defined as a Class 2 medical device by the US Food and Drug Administration (2005). As a result of its classification, the development and testing of new designs is subject to special controls, which prolong the time before the product can be sold on the market. Proctor and Gamble (Cincinnati, Ohio, USA) have adapted computer modelling techniques to simulate the pad against the skin in the pelvic area and observe its deformation as the body moves. They have investigated the possibility of correlating the contact pressure between the pad and the skin with the comfort experienced by the user (Macura *et al.* (2005)). These modelling tools have cut down on the development time of new designs. Lengthy protocols that have to be followed when testing on volunteers have been reduced. As a result new products appear on the market more quickly. This approach could also be taken in the design of other personal care products such as sticky plasters and razors. Indeed, skin modelling has aided in the design of razors and shavers (Hendriks, 2005). An important phenomenon in shaving is doming, which is defined as the penetration of the skin into the slits between the blades. A skin model, which can simulate accurately the doming effect, may result in better razors and shavers that cut the hair even shorter without cutting the skin itself.

In recent years, computer animation has played an increasingly important role in the entertainment industry. Computer animation has been used in parts of films to create special effects – Terminator 2, The Matrix and Forrest Gump. Entire films have also been produced using computer animation, such as Toy Story, Shrek and Monsters, Inc. A major challenge in computer animation is to create human characters that look physically realistic. Much of this realism is dependent on how well the skin is animated along with its finer details such as the wrinkles and folds that occur when the skin is deformed. Many computer animation models are purely geometrically based (Park and Hodgins, 2006; Zhang *et al.*, 2006). They do not take into account the mechanical properties of the skin. In taking a geometrical approach, the more subtle details such as the wrinkling and furrowing are more difficult to replicate (Terzopoulos and Waters, 1990). Bando *et al.* (2002) developed a method whereby the user could specify the direction, depth and width of the wrinkles on a skin model

4

surface. The success of this type of approach is quite dependent on the artistic ability of the user. There are several animation models that are anatomically-based and take into account the mechanical and geometrical properties of the muscles but little or no attention is given to the skin (Albrecht *et al.*, 2003; Tsang *et al.*, 2005). The use of a physically-based multi-layer model of skin in animation models would enhance the quality of computer generated human characters.

Chapter 2

Literature Review

2.1 Introduction

This chapter first outlines the anatomy of human skin, detailing the physical and mechanical properties of each layer. A review of the existing skin models in the literature is carried out as well as experimental literature in the area of modelling of skin wrinkling. The chapter concludes with the aims, hypotheses and objectives of this thesis.

2.2 Anatomy of biological skin

Human skin is part of the integument along with accessory structures such as hair, nails, glands, nerves and blood vessels. It is one of the largest organs in the human body with an average area of 2 m² in an average adult (Leider and Buncke, 1954; Odland, 1991) and serves a variety of functional roles including – providing a protective barrier against the external environment; containment of body fluids and organs; regulation of fluid and heat loss; and the synthesis of vitamin D when exposed to sunlight.

It is a complex stratified material consisting of several distinct layers. The basic structure of skin, shown in Figure 2.1, consists of the epidermis as the top-most layer with the dermis underneath. The subdermal layer, known as the hypodermis or subcutaneous tissue is not usually considered part of the skin. Skin thickness and the relative thicknesses of each layer vary according to age, gender, race and also depending where on the body the skin is situated. Skin in the back, buttock and sole area are the thickest on the body at about 2.0 mm. The eyelid and inguinal skin are among the thinnest on the body at about 0.5-0.6 mm (Barker, 1951; Lee and Hwang, 2002).
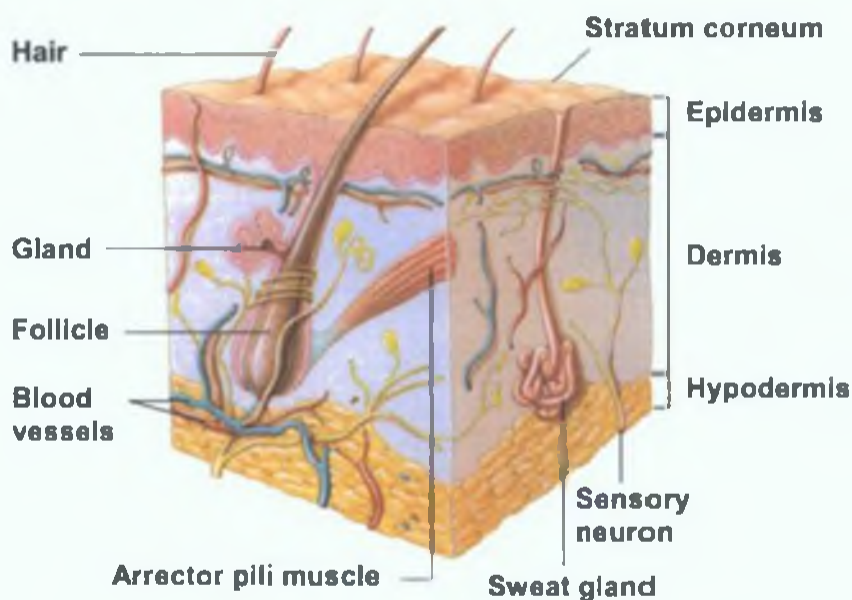
Figure 2.1: The basic structure of skin (Adapted from Chynoweth (2006))

2.2.1 The epidermis

The epidermis is a stratified squamous consisting of cells, cellular debris and varying amounts of water. It is divided further into several sub-layers shown in Figure 2.2; starting from the inside: the basal layer (stratum basale), the spinous cell layer (stratum spinosum), the granular layer (stratum granulosum), the clear layer (stratum lucidum) and the horny layer (stratum corneum). The principal cell type in the epidermis is called the keratinocyte and they are attached to each other by cellular attachments known as desmosomes. Keratinocytes are produced in the basal layer. The cells in this layer reproduce once every 200 to 400 hours, when one daughter cell remains in the basal layer and one migrates up to the spinous layer (William, 2003). This layer contains two to six rows of keratinocyte cells, which change from columnar to polygonal in shape. The cells begin to differentiate and keratinise. The cells pass from the spinous to the granular layer, where they continue to keratinise and start to flatten. The cell nuclei also begin to degrade. In the stratum lucidum, the cell nuclei completely disintegrate. Keratinisation increases and the cells flatten further before displacing upwards to the outermost – the stratum corneum (Odland, 1991). The stratum corneum is the thickest of all the epidermal layers. It prevents excessive water loss from the body while protecting it from harmful external materials (William, 2003). It is a tough, flexible tissue consisting of several layers of dead keratinised

7

Figure 2.2: Schematic of the human epidermis (Adapted from William (2003))

cells, known as corneocytes. The cells of the stratum corneum are continuously sloughed off the top by abrasion while being produced from the layers below. Koutroupi and Barbenel (1990) described it as being in a state of dynamic equilibrium and almost unique among tissues in that failure is a normal part of its process. The normal human epidermis replaces itself in a period of 45 to 75 days (Odland, 1991).

The surface of the stratum corneum is not flat and smooth but is covered by a network of grooves as seen in Figure 2.3. The horizontal direction is curved upwards, while the direction of the grooves or creases is in towards the dermal layer (Ferguson and Barbenel, 1981; Koutroupi and Barbenel, 1990; Schellander and Headington, 1974).

The stratum corneum is often treated as a separate membrane in the field of transdermal drug delivery because it is the biggest obstacle of all the skin layers (William, 2003). The layers beneath the stratum corneum are sometimes referred to as the 'living' or 'viable' epidermis.

The thickness of the epidermis varies from about 4% of the total thickness of the skin in the back region and up to over 40% on the sole of the foot and palm of the hand to protect against abrasion (Lee and Hwang, 2002). The thickness of the stratum corneum varies from 10 to 40 μm (Batisse *et al.*, 2002; William, 2003; Wu *et al.*, 2006b; Yuan and Verma, 2006).
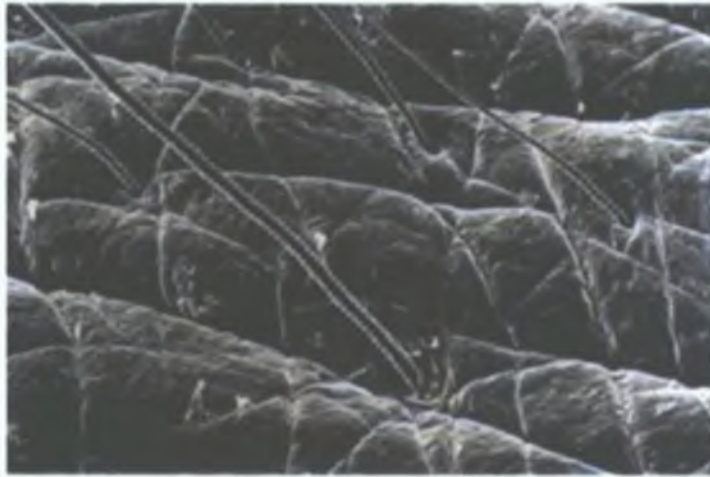
Figure 2.3: Scanning electron microscope image of the surface of the stratum corneum with hair (Image from Gray (1997))

2.2.2 The dermis

The dermis is a dense network of collagen, reticulin, and elastin fibres imbedded in a semigel matrix of ground substance. Approximately 75% of the dry weight of dermal tissue consists of strong, stiff collagen fibres, while the rubber-like elastin and the semi-fluid ground substance make up 4% and 20% of the dry-weight, respectively. Only trace amounts of reticulin are found in adult skin (Wilkes *et al.*, 1973). Collagen fibres are arranged in bundles ranging in diameter from 1 to 40 µm. These in turn are composed of fibrils whose mean diameter is on the order of 100 nm. Elastin fibres form a delicate scattered network lying between the collagen (Oxlund *et al.*, 1988). Unlike collagen fibres, they do not have a fibrillar substructure and range in diameter from 0.5 to 8 µm. The semi-fluid ground substance is an amorphous mass of proteoglycans and water. The water molecules are not free and are bonded by hygroscopic hyaluronic acid, which is a component of the proteoglycans (Wilkes *et al.*, 1973).

The dermis is usually subdivided into two further layers – the papillary dermis and the reticular dermis. The papillary dermis is thinner and lies adjacent to the epidermis. It contains a less dense distribution of elastin and collagen fibres and proportionally a greater amount of ground substance (Odland, 1991).

The dermis varies in thickness from 0.5mm in the eyelid and inguinal regions to 2.0 mm in the back region (Lee and Hwang, 2002).

9

2.2.3 The hypodermis

The hypodermis or subcutaneous tissue is not considered part of the skin. Its principal functions are to provide thermal insulation to the body, protect against mechanical shock and store energy. The principal blood vessels and nerves access the skin through this layer (William, 2003). It consists of mainly of adipose or fat cells and loosely arranged fibres, which connect with the dermis. There is no clear boundary between this layer and the dermis. The hypodermis provides the flexible connection between the skin and the other internal soft tissues. The hypodermis is loosely attached to the dermis by way of vertical fibrous septae and reasonable mobility of the skin is allowed over most parts of the body[*]. These septae often have to be cut during surgery in order to be able to pull a wound together and close it with sutures (Bezzant, 2000). The lobules or chambers of adipose tissue are separated by strands of collagen fibres or septae. When these chambers become excessively filled with fat, the attachment points of the dermis to the hypodermis are more obvious because the surface of the skin appears dimpled (Scheinfeld, 2004). This appearance is known as gunoid lipodystrophy or cellulite (Smalls *et al.*, 2005). The thickness of the hypodermis varies in different parts of the body; it being the thinnest on the eyelids and the thickest on the abdomen (Cohen and Wood, 2000).

2.2.4 The epidermal-dermal junction

The area of attachment between the dermis and the epidermis is known as the basement membrane zone or epidermal-dermal junction. The basal layer of the epidermis comprises of the lamina lucida, which is about 20 nm thick, and the lamina densa. Anchoring filaments are believed to traverse the lamina lucida and down and back from the lamina densa. Collagen fibrils pass through these anchors from the dermis and insert into the lamina densa. These anchors create a firm attachment between the dermis and epidermis (Odland, 1991).

The interface between the epidermis and the dermis is also not flat but undulating as can be seen in the SEM scans of Brown (1973) in Figure 2.4. The projections of dermis to the surface above are known as dermal papillae. The undulant contours increase the area of contact between the layers of skin, and help to prevent the

---

[*] Information retrieved from www.mc.vanderbilt.edu/histology/labmanual2002/labsection2 on 4th April 2006

10
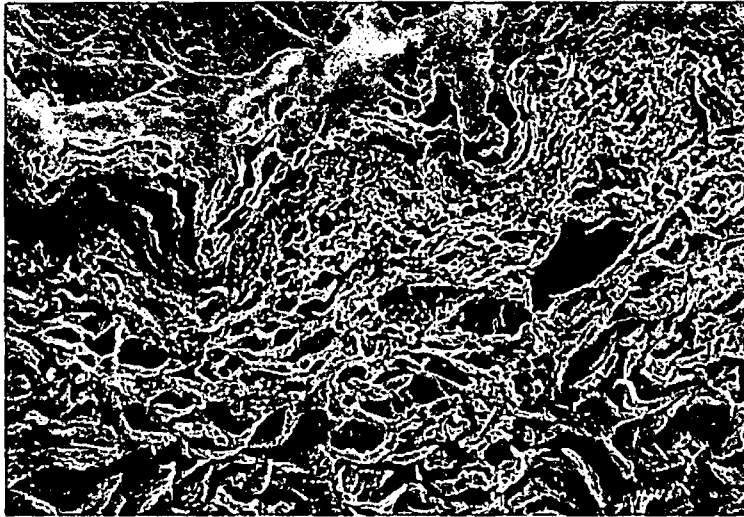
Figure 2.4: Scanning electron microscope image of a cross-section of human skin showing the undulating interface between the epidermis and dermis (Image from Brown (1973))

epidermis from being sheared off thus enhancing the firmness of attachment at the epidermal-dermal junction (Odland, 1991).

2.2.5 Skin accessories

The skin accessories such as the blood vessels, lymphatic vessels, glands, hair and nerves are described in more detail in Appendix A.

2.3 Constitutive behaviour of biological skin

A material as complex as skin would be expected to exhibit complex mechanical behaviour. Experimental tests on skin have shown it to be highly nonlinear (Lanir and Fung, 1974), anisotropic (Daly, 1982; Lanir and Fung, 1974; Schneider, 1982) and viscoelastic (Del Prete et al., 2004; Har-Shai et al., 1996; Silver et al., 2001). In vivo tests have shown skin to exhibit creep and stress relaxation (Wan Abas, 1994; Daly, 1982; Khatyr et al., 2004). Har-Shai et al. (1996) demonstrated the hysteresis effect of facial skin when cyclically loaded. The mechanical properties of skin can be related to the structure of the various layers. Table 2.1 contains a summary of the experimental tests carried out on whole skin or its components.

Table 2.1: Summary of mechanical properties from experimental studies of whole skin, skin components or hypodermis tissue

Author(s)	Soft tissue studied	Test	Key mechanical property findings
Park and Baddiel (1972)	Pig stratum corneum	Uniaxial tension *in vitro*	Young's modulus 6 MPa (@ 100% RH) to 1-4 GPa (@ 30% RH)
Koutroupi and Barbenel (1990)	Human stratum corneum	Uniaxial tension *in vitro*	Young's modulus 0.21 GPa (@ 76% RH)
Wu *et al.* (2006b)	Human stratum corneum	Uniaxial tension *in vitro*	Young's modulus 5 MPa (@ 100% RH) to 1000 MPa (@ 45% RH)
Yuan and Verma (2006)	Porcine stratum corneum	Nano-indentation *in vitro*	Young's modulus 50 MPa (wet) to 200 MPa (dry)
Shergold *et al.* (2006)	Pig skin	Unconfined compression	Stress at strain of -40% varies from 2 to 60 MPa as strain rate increases from 0.004 to 4000 s^{-1}
Ankersen *et al.* (1999)	Pig back and belly skin	Uniaxial tension *in vitro*	15 MPa stress @ 42% strain for back skin – almost isotropic; 19 MPa stress @ 30% strain in longitudinal direction for belly skin – 6MPa stress @ 96% strain in transverse direction
Pan *et al.* (1998)	Human breast skin	Uniaxial tension *in vitro*	Young's modulus increases from 2 kPa @ 0% strain to 30 kPa @ 50% strain
Wan Abas (1994)	Human forearm and abdomen skin	Uniaxial and biaxial tension *in vivo*	Terminal stiffness varied from 3.0 to 5.7 kN/m; Stress relaxed 5% (Uniaxial) to 10% (Biaxial) over 400s when subjected to strains of 0.15 (Uniaxial) and 0.11 (Biaxial)
Silver *et al.* (2001)	Human skin and dermis	Uniaxial tension *in vitro*	Young's modulus 0.1 MPa up to strains of 40%; increases to 18.6 MPa at strains above 40%
Daly (1982)	Human skin	Uniaxial tension *in vitro*; compression *in vivo*	Young's modulus 5kPa up to strains of 40%; increases to 30 MPa above 0.7 strain
Khatyr *et al.* (2004)	Human forearm skin	Uniaxial tension *in vivo*	Stress relaxation from 27.5 kPa to 20.0 kPa @ unspecified deformation over 30s
Miller-Young *et al.* (2002)	Human heel fat pads	Unconfined compression *in vitro*	9.2 kPa compressive stress @ 50% deformation;Stress relaxation from 21.3 kPa to 5.4 kPa @ 40% deformation over 60s
Wu *et al.* (2006a)	Porcine skin and hypodermis	Unconfined compression *in vitro*	Compressive stress relaxed by 40 to 60% over 30s
Zheng and Mak (1996)	Porcine skin and hypodermis	*In vitro* compression	Force required to compress tissue 15% decreases from 2 to 1.2 N over 10s

2.3.1 Mechanical properties of the epidermis

The stratum corneum is the major load-bearing component of the epidermis (Koutroupi and Barbenel, 1990). The mechanical properties are highly dependent on the amount of water the layer has absorbed and the temperature in the environment. Water in the stratum corneum breaks down the hydrogen bonds in the keratin thus plasticizing it (Park and Baddiel, 1972; Takahashi *et al.*, 1980).

Park and Baddiel (1972) carried out a series of tensile tests of pig's ear stratum corneum at different controlled relative humidities. They reported the Young's Modulus of stratum corneum varied from about 1-4 GPa at 30% RH; 200MPa at 75% RH; and 6 MPa at 100% RH.

Koutroupi and Barbenal (1990) carried out a series of mechanical tensile tests on human stratum corneum and found it to be a relatively stiff, inextensible and isotropic tissue compared with other soft tissues. The stress relaxation was only a minor phenomenon when compared to its presence in the dermis. The load-extension behaviour of the stratum corneum was found to be non-linear but the initial compliant phase was much smaller than for soft-connective tissues. The Young's Modulus was measured as 0.21 GPa for the linear portion of the stress-strain curve. They also determined that the strain at which failure occurred in the stratum corneum was less than the limit strain of skin. This would suggest the hypothesis that the surface patterns act as a reserve of skin thus allowing it to stretch during normal function.

The experiments of Ferguson and Barbenel (1981) support this hypothesis. They conducted *in vivo* uniaxial stretching experiments on forearm skin, where casts were made of the surface of the skin surface before and during the stretching using silicone rubber and epoxy resin. Surface profile and roughness characteristics of the casts were measured using a mechanical profilometer. They showed that as the skin was stretched, its surface became smoother. They found that in directions where the limit strain of the skin was higher, the average peak-to-valley height was higher and the mean spacing was lower. Their results also show that the skin surface patterns have a directionality, which allows the stratum corneum to extend with the underlying layers.

More recently, tensile studies carried out by Wu *et al.* (2006b) measured Young's moduli of stratum corneum decreasing from ~1000 to 5 MPa with increasing hydration. Yuan and Verma (2006) measured the elastic modulus of dry stratum

corneum to be 200 MPa and the elastic modulus of wet stratum corneum to be 50 MPa. Their method of testing was microindentation.

No reports could be found in the literature describing the mechanical properties of the living epidermis. Hendriks (2005) performed experiments to characterise mechanical behaviour of the epidermis and the upper dermis but not the living epidermis on its own.

2.3.2 Mechanical properties of dermis

The highly non-linear behaviour of skin can be attributed in large part to the structure of the dermal layer. Figure 2.5 shows a typical stress-strain curve from a uniaxial test on abdominal skin (Brown, 1973). The non-linear behaviour can be divided into three phases. The first phase is characterised by low-stiffness. In this phase the collagen network is undulated and unaligned and does not contribute significantly to the mechanical properties. The initial low stiffness response of skin can be attributed to the elastin network (Daly, 1982). In the second phase, the collagen fibres begin to align and straighten in the direction of the applied load. As a result, the stiffness of the skin increases. In the third phase, the collagen network is hypothetically aligned and straightened. Further extension of the skin requires extension of the collagen fibres. The high stiffness of the skin in this region is similar
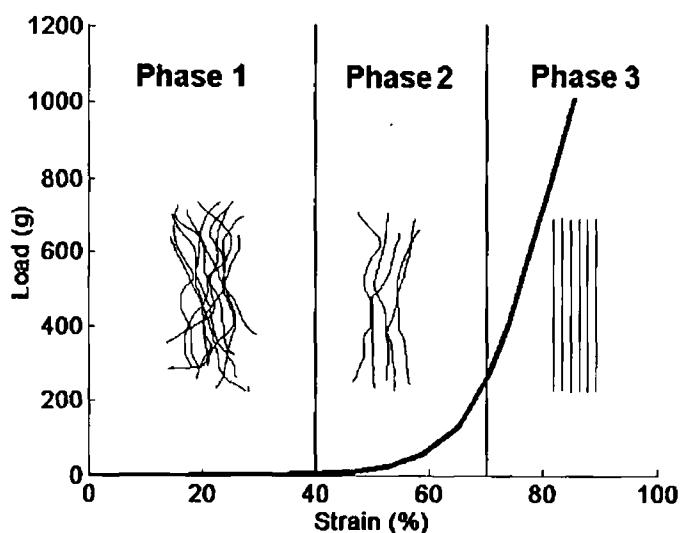
Figure 2.5: Load-strain response of an *in vitro* uniaxial test of human abdominal skin. In Phase 1, the collagen fibres are straightening out but not carrying load; In Phase 2, some fibres are straight and are starting to carry the load; In the final Phase 3, most of the fibres are straight and are carrying the load. Data reproduced from Brown (1973)

to that of pure collagen (Wilkes *et al.*, 1973). The elastic behaviour of skin is facilitated by the elastin network, which provides a return spring mechanism for the collagen fibres (Daly, 1982). This property varies with age. The Young's modulus of the dermis varies widely depending on the amount of deformation, the age and condition of the subject and also the type of test used to obtain the result. In a review of mammalian tissues, Silver *et al.* (1992) report Young's moduli of skin at failure ranging from 6 to 40 MPa.

The dermis in general is an anisotropic material – its behaviour is direction-dependent. Dupuytren (1834) first investigated the directional effects in skin. Langer (1978) punctured the skin of cadavers with conically pointed instruments and found elliptical splits were produced. The lines of the major axes of these slits are known as Langer's Lines. The skin's mechanical anisotropy follows the same pattern of Langer's Lines and stretches the least in the direction of the lines. It has been concluded that the collagen and elastin fibres form an irregular multidirectional system in which there is a preferential orientation in the lines' direction (Lanir, 1987). This implies that when a sample is stretched in the direction of minimum extensibility the fibre networks align along the load axis at lower strains (Wilkes *et al.*, 1973). Lanir and Fung (1974) demonstrated anisotropy with biaxial tension tests on rabbit skin. Figure 2.6 shows the results of tests on a sample of rabbit skin when orientated such that the stretch is applied along the length of the body and subsequently applied along the width of the body.

The mechanical properties of skin are time-dependent. Lanir and Fung (1974) have shown that biaxial tension tests of rabbit skin carried out at different strain-rates produce slightly different stress-strain curves. Their tests also show the viscoelastic nature of skin with significant hysteresis loops in stress-strain relations as seen in Figure 2.6. Wan Abas (1994) demonstrated stress relaxation under constant strain *in vivo* in human forearm skin as shown in Figure 2.7. Viscoelastic effects in skin are very noticeable for strains corresponding to the region when collagen fibres are carrying part of the load (Daly, 1982) although Pereira *et al.* (1991) report that viscoelastic effects are also present in the initial large strain-low stress region. The viscoelastic response of skin has been attributed in part to the relative movement between the alignable collagen network and the proteoglycan ground substance in the dermis. Stress relaxation following a step increase in the strain on a sample is thought to be due to the collagen fibres assuming an equilibrium position over a period of time

15
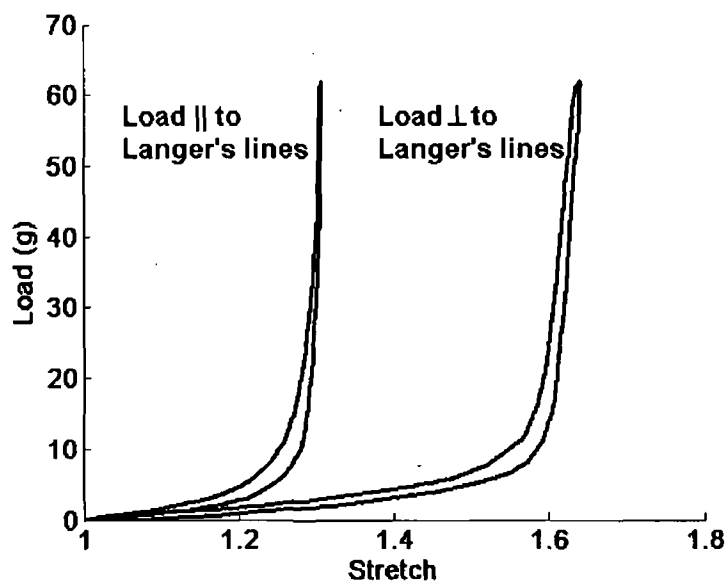
Figure 2.6: Biaxial stretch tests on *in vitro* rabbit skin. There is a different response depending on whether the load is applied parallel or perpendicular to the Langer's lines in the skin. There is also a significant amount of hysteresis when the skin is loaded and unloaded. Data reproduced from Lanir and Fung (1974)
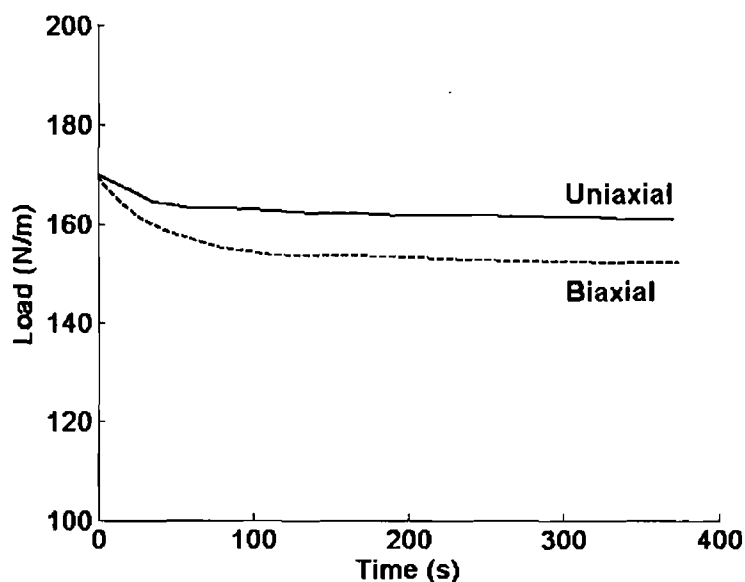
Figure 2.7: Uniaxial and biaxial stress relaxation tests on *in vivo* human forearm skin. Data reproduced from Wan Abas (1994)

while the ground substance is squeezed through the gaps between the fibres. The higher the stress level, the more closely the fibres are packed together, the narrower the space available for the ground substance to squeeze through (Wilkes *et al.*, 1973).

It is known that soft tissues subject to successive cyclic tests yield different results over the first few cycles but the results converge as the number of cycles increase

16

(Fung, 1993). This phenomenon is known as preconditioning and several experimental studies have shown this behaviour in skin (Lanir and Fung, 1974; Wan Abas, 1994; Har-Shai *et al.*, 1996). Preconditioning in skin can be attributable to the collagen fibres in the dermis reorientating in response to the cyclical load. Eventually, after a number of cycles a steady-state is reached where no further reorientation takes place unless the upper or lower limits of the cycling are changed (Fung, 1993).

2.3.3 Mechanical properties of the hypodermis

In comparison to the epidermis and dermis, there is little reported data in the literature regarding the mechanical properties of the hypodermis.

Gerling *et al.* (2003) assumed a linear-elastic hypodermis in their finger-tip model with a Young's modulus of 34 kPa and Poisson's ratio of 0.48. Chabanas *et al.* (2003) also assumed linear-elasticity when modelling soft tissue deformations. Their hypodermis model had a Young's modulus of 15 kPa and a Poisson's ratio of 0.49.

Miller-Young *et al.* (2002) performed unconfined compression tests on human heel fat pads and found it exhibited nonlinear, viscoelastic behaviour. They measured a quasi-static stress of 9.2 kPa at 50% deformation. When rapidly compressed to 40% deformation, the stress relaxed from 21.3 to 5.4 kPa over one minute. The fat pads were determined to be isotropic under compression but they did speculate that anisotropy would probably be observed under shear loading due to its structure. Human heel fat is different to other human adipose tissues with a higher ratio of unsaturated to saturated fatty acids. This results in a soft tissue with a lower viscosity than other fatty tissues.

Wu and Dong (2005) modelled the hypodermis of the finger-tip using the biphasic model of Mow *et al.* (1980). They stated that the hydraulic permeability of this tissue had not been measured to date so they assumed it to have a similar permeability to articular cartilage. They also used the human heel fat results of Miller-Young *et al.* (2002) discussed earlier to generate material parameters for their model.

More recently, Wu *et al.* (2006a) conducted unconfined compression tests of porcine skin/hypodermis specimens. The stress relaxation results were consistent with the results of the human calcaneal fat pad discussed earlier. The compressive stress relaxed by 40 to 60% over 30 seconds.

Zheng and Mak (1996) conducted indentation experiments on porcine specimens consisting of a fat and muscle layer. They showed the compressive stress increased

non-linearly to a peak of about 10 kPa when the deformation in the fat layer was about 10%. When held at a deformation of 10% the stress relaxed to about 5 kPa after about 10 seconds.

2.4 Modelling Literature

2.4.1 Models of biological skin

Single-layer constitutive models

Many models have been previously developed to replicate the response of skin to different deformations. The models differ in terms of their functional form and their underlying assumptions. They can be divided into two categories: (1) phenomenologically based models, which are based on observed behaviour only and have no direct physical connection with the underlying mechanism responsible for that behaviour; (2) physically based models, which establish a connection between the microstructure of skin and its mechanical behaviour. Some phenomenological models are mathematically simple and therefore straightforward to implement (Barbenel and Evans, 1977; Miller, 2000; Tong and Fung, 1976). However the parameters in these models tend to have little physical meaning (Holzapfel *et al.*, 1996; Rubin and Bodner, 2002). The form of the model can also change depending on the type of test and the material being tested and so phenomenological models may not accurately represent the material in reality under all conditions such as a uniaxial model by Ridge and Wright (1965).

One of the first microstructurally based models was introduced by Lanir (1979a; 1979b; 1983) for flat, collagenous tissues. He considered a network of linearly elastic elastin and a network of linearly viscoelastic collagen to produce a nonlinear viscoelastic model. No experimental data were fitted to the model. Shoemaker *et al.* (1986) derived a physically based nonlinear viscoelastic model applicable to two-dimensional or membranous orthotropic soft tissues. The stress was due to the sum of compliant and stiff fibrous components in the tissue. The compliant stress was assumed to depend on the strain rate components based on a linear viscoelastic law. The stress due to the stiff fibrous component depended on the strain and the orientation of the stiff fibres in the membrane. Experimental biaxial tests on human skin were fitted to the model with limited success. One deficiency was that the model tended to predict a more abrupt change in slope at the 'elbow' region of the stress-

18

strain curve compared with the experimental data. One advantage of the physically based models described here is that the model parameters are physically meaningful. However, the models can be mathematically complex and can be unwieldy to work with in practice (Bischoff, 2001).

Bergstrom and Boyce (1998; 2001) developed an isotropic viscoelastic model for elastomers that was applied to soft biological tissues with some success. This three-dimensional physical model consists of a hyperelastic network in parallel with a time-dependent network, where the fibres are assumed to diffuse along their lengths. This diffusion relaxes the overall stress in the network over time. This theory was originally proposed by de Gennes (1971) and further developed by Doi and Edwards (1986) and is known as reptation dynamics because the movement is likened to the creeping movement of snakes. Fyhrie and Barone (2003) used reptation dynamic theory in their linear viscoelastic model to simulate stress relaxation of cartilage. A drawback of the Bergstrom-Boyce model is that it does not capture the anisotropy of skin. Bischoff *et al.* (2002) developed a hyperelastic orthotropic model that was used to fit the biaxial tension tests of Lanir and Fung (1974) among others. Both these models are mathematically straightforward compared with other physically-based models. Both models contain parameters that are microstructurally based and can be related to material measurements in the laboratory. Both models have been successfully implemented into finite element models enabling more complex boundary value problems to be examined.

Bischoff *et al.* (2004) proposed a model, which contained the orthotropic feature of their earlier model and the viscoelastic approach of the Bergstrom-Boyce model. The model was used to simulate the biaxial tension and stress relaxation rabbit skin tests of Lanir and Fung (1974). Although, reasonable agreement was observed between model and experiment, it could probably have been improved if some of the material parameters were not limited to fixed values.

Multi-layer models

The models for skin described previously essentially model the dermal layer of skin, which is assumed to dominate its mechanical properties. They do not provide details about the influence of the epidermis and sub-dermal layers.

Magnenat-Thalmann *et al.* (2002) developed a three-layer two-dimensional model, to simulate the wrinkling and folding of skin when deformed. Their incompressible

19

three-layer model consisted of the stratum corneum, a combined epidermal/papillary dermal layer and the reticular dermal layer. Each layer was assumed to be linear-elastic, which is only true for very small deformations. Their simple model captured qualitatively several of the wrinkling characteristics of skin, such as a stiffer and thicker stratum corneum results in larger wrinkles. However, they did not make any quantitative comparisons with experiments on real skin. They also did not include in the model the natural tension or pre-stress present in living human skin.

Zhang et al. (2004) developed a multi-layer facial skin model to simulate realistic facial expressions. They assumed a phenomenological non-linear elastic constitutive equation for the epidermis, dermis and hypodermis. The two parameters in their non-linear spring were adjusted to approximately match the mean stress-strain response of facial tissue. For the epidermal layer, the parameters were set higher to model the higher stiffness, while they are set lower to reflect the more supple dermis and hypodermis. The anisotropic and viscoelastic properties of skin were ignored. The pre-stress in the skin was not explicitly accounted for. There was no quantitative comparison of the facial expressions modelled with real expressions.

Hendriks et al. (2003; 2006) carried out a series of numerical-experimental studies on human skin. They developed a multi-layer finite element model of skin consisting of two layers representing the epidermis and papillary dermis as one layer and the reticular dermis as the second. The constitutive behaviour of each layer was described by an extended Mooney equation. A pilot two-layer model representing a combined epidermal/dermal layer and a subdermal fat layer was also built. Tests demonstrated that the subdermal layer had little influence on the overall model results for this particular case of suction. The anisotropy and viscoelasticity of skin was ignored in this study and there was no prestress in the skin at the start of each analysis. The effect of the stratum corneum layer was also assumed to be negligible for this particular case study.

Several multi-layer skin models have been developed to investigate the biomechanics of human and animal fingertips. Some of these models assumed each layer in the skin to be isotropic and linear elastic (Dandekar et al., 2003; Gerling and Thomas, 2003). Others developed multi-layer models of fingertips where the bone, subcutaneous tissue, skin and nail were represented but the skin itself was modelled as a single layer (Serina et al., 1998; Wu and Dong, 2005).

Finite element models of wound closure

Several finite element models have been developed to look at the stress fields around closed wounds of various shapes. Several of these models were two-dimensional and considered the skin as a single layer, ignoring its non-linear stress-strain behaviour and ignoring the underlying hypodermis (Lott-Crumpler and Chaudhry, 2001; Retel *et al.*, 2001). Kirby *et al.* (1998) developed a three-dimensional model but the skin was still assumed to be a strictly linear elastic. They did account for the hypodermis using a method first proposed by Larrabee and Galt (1986). The attachment of the skin to the hypodermis was modelled by linear elastic springs. The finite element analysis work of Yoshida *et al.* (2000; 2001) modelled the extrusion of skin when sutured using different methods. They used a simple linear isotropic constitutive law for skin. A layer of elements was included below the skin elements to model contact between the skin and subcutaneous layers.

None of the models described above account for the pre-stress in the skin when simulating the closure of wounds. The pre-stress would be an important factor in wound healing (Bucalo and Iriondo, 1995; Cacou and Muir, 1995).

2.4.2 Modelling wrinkling

In the previous section, many models of skin were discussed and several of them have been implemented into finite element analyses. Relatively few finite element skin models, however, have been developed to study wrinkling – a feature common to all human skin. The model of Magnenat-Thalmann *et al.* (2002) has already been discussed in the previous section. No other finite element models developed for skin wrinkling were found in the literature. Wrinkling is a phenomenon that occurs in many engineering applications such as the stamping of sheet metal parts (Weili *et al.*, 2002), solar sails for deep space exploration (Tessler *et al.*, 2005), stretchable interconnects in electronics (Lacour *et al.*, 2004) and the design of clothing patterns with textiles (Jing *et al.*, 2005). As a result, many studies have been carried out attempting to simulate wrinkling in various situations.

Several approaches have been developed that can be used to determine regions in membranes where wrinkling may occur, including tension field theory and relaxed-strain energy methods (Steigmann, 1990; Pipkin, 1994; Haughton and McKay, 1995). Danielson and Natarajan (1975) applied tension field theory to the closure of an elliptical hole in stretched skin and determined the regions where the maximum and

minimum stresses occur – important factors in wound healing. Both of these approaches cannot, however, predict the finer details of the wrinkles such as the amplitude and wavelength (Tessler *et al.*, 2005).

Several analytical models have been proposed to predict the amplitude, wavelength and length of wrinkles formed in various situations. These include the wrinkles formed in an elastic membrane under tension (Cerda and Mahadevan, 2003); the wrinkles around a contracting 'scar' in latex membranes (Geminard *et al.*, 2004; Cerda, 2005); and the wrinkles in a square solar sail membrane under tension (Wong and Pellegrino, 2006b). While these models predicted the size of the wrinkles with reasonable accuracy, they all assumed the membranes were isotropic and linear elastic, which is not true in the case of human skin.

One of the earliest applications of the finite element method to wrinkling problems was carried out by Miller *et al.* (1985). Since then, many finite element wrinkling models have been developed using implicit schemes, where either eigenvalues were calculated (Miyamura, 2000; Wong and Pellegrino, 2006a) or the presence of negative principal stresses and strains monitored (Stanuszek, 2003; Raible *et al.*, 2005) to predict possible wrinkle-shapes in membranes under various loads. Other implicit methods involved imposing pseudo-random geometric perturbations in the out-of-plane direction to initiate wrinkling in the membrane (Tessler *et al.*, 2005).

Several studies have used finite element schemes involving explicit time integration to simulate wrinkling (Kawka *et al.*, 2001; Wang *et al.*, 2004; De Magalhaes Correia and Ferron, 2004). Implicit codes that use schemes like the Newton-Raphson method require the inversion of the tangent stiffness matrix. In wrinkling and buckling problems, this matrix is near-singular and so inversion can lead to difficulties with convergence. Explicit schemes do not require the inversion of a tangent stiffness matrix. No geometrical perturbations are necessary to start the wrinkling. The drawback of explicit schemes is that the time-step to advance the solution is usually very small and so very long run-times may be necessary. This problem can be minimised without significantly changing the results of wrinkling analyses by increasing the density of the material in the model (Wang *et al.*, 2004). This technique is known as mass-scaling. Wang *et al.* (2004) concluded the use of an explicit finite element scheme was a more robust method to predict wrinkling than other implicit static methods.

2.5 Clinical Literature

2.5.1 Skin wrinkling

Wrinkling is a phenomenon common to all human skin. When skin is pinched it causes temporary wrinkles to develop that disappear when the skin is released. On the face, certain wrinkles are important for communication and self-expression (Magnenat-Thalmann *et al.*, 2002). If our foreheads did not furrow when we frowned or wrinkles did not extend from the corner of our mouths when we smiled, our expressions would be blander (Hatzis, 2004). Wrinkles also allow the free movement of joints. Examples include the wrinkles on the skin at finger joints and the elbow. As skin ages, its ability to return to its original shape when deformed is diminished and permanent wrinkles develop over time (Batisse *et al.*, 2002). Indeed, because society closely associates wrinkles in skin with loss of youth and increasing age, there is considerable motivation for investigations of wrinkles in an effort to understand their formation and determine methods to reduce their appearance.

2.5.2 Classification of wrinkles

According to Pierard *et al.* (2003) and Lemperle *et al.* (2001), there does not appear to be a consensus on the definition and classification of wrinkles. They can be divided into five categories - (i) crinkles, (ii) glyphic wrinkles, (iii) linear facial wrinkles and (iv) gravitational wrinkles.

Crinkles (also known as atrophic wrinkles) occur in aged skin and appear as very fine micro-wrinkles on the surface (Kligman *et al.*, 1985; Pierard *et al.*, 2003). Crinkles are not permanent and disappear when the skin is lightly stretched.

Glyphic or elastotic wrinkles are permanent and appear on skin areas that receive large amounts of solar radiation such as the sides and back of the neck and on the cheeks (Pierard *et al.*, 2003; Hatzis, 2004).

Linear facial or expressional wrinkles appear on the face such as frown-lines on the forehead and the grooves radiating from the outer corner of the eye (Lemperle *et al.*, 2001). Their orientation is perpendicular to the direction of the underlying muscle fibres. In young elastic skin, linear facial wrinkles disappear immediately after the expression is relaxed. With increasing age, they begin to remain after relaxation and become permanent.

2.5.3 Causes of wrinkles

The different types of wrinkles described previously develop as a result of changes in the skin structure.

Clinical studies have supported the hypothesis that skin wrinkling progresses with age because the stratum corneum gets stiffer (Batisse *et al.*, 2002). In addition to this, exposure to ultraviolet B radiation deteriorates the keratin intermediate filaments in the stratum corneum resulting in more wrinkling (Sano *et al.*, 2005).

There appears to be a conflict as to whether an increase or decrease in the collagen fibre density in the dermis leads to increased wrinkling. The work of Oba and Edwards (2006) showed a correlation between the destruction of the collagen fibres and an increase in wrinkling. According to Pierard *et al.* (2003), as skin ages there is a loss of collagen fibres in the reticular dermis and hypodermis and this leads to atrophic wrinkles. While a decrease in collagen fibre density would be in agreement with other reports in the literature, this decrease has been said to occur in the upper or papillary dermis (Batisse *et al.*, 2002). It has also been observed that the collagen fibre density in the dermis as a whole increases as skin ages (Lavker *et al.* cited in Silver *et al.* (2001)).

The loss of the natural tension in the skin with age is also the cause of increased wrinkling. This is particularly true in the case of gravitational wrinkles mentioned earlier (Pierard *et al.*, 2003).

Hatzis (2004) reported that crinkles develop as a result of the loss of elastic fibres that keep the epidermis firmly attached to the dermis. Kligman *et al.* (1985) observed that the undulating epidermal-dermal junction also flattens.

Expressional or linear facial wrinkles are as a result of repeated contractions occurring at the same point. These contractions cause the hypodermal septae, which anchors the skin to the underlying fascia, to thicken and shorten over time (Hatzis, 2004). Tsukahara *et al.* (2004) proposed that repeated facial movements may increase wrinkle depth from morning to afternoon.

2.5.4 Measurement of wrinkles

Mechanical profilometry has been used to measure skin topographies since the 1950s (Fischer *et al.*, 1999). The process involves generating silicone replica impressions of the skin surface and then scanning the replicas by drawing a stylus across the surface (Ferguson and Barbenel, 1981; Lemperle *et al.*, 2001). A

disadvantage with the mechanical stylus profilometer approach is that profile of the skin surface cannot be measured directly but only through the use of replicas. The quality of the results, therefore, is dependent on the quality of the replica. Care has to be taken so that air-bubbles do not form in the replica material and that contact between the replica material and the subject does not change the profile of the wrinkles (Jacobi *et al.*, 2004). There is also evidence that the replica material may not penetrate to the bottom of deep narrow wrinkles (Akazaki *et al.*, 2002).

Optical profilometry techniques have been used to measure skin wrinkles either through silicone replicas (Tsukahara *et al.*, 2004) or *in vivo* (Akazaki *et al.*, 2002; Jacobi *et al.*, 2004). Most optical profilometry methods involve directing a light source onto the skin or replica surface at a specified angle and detecting the reflection using a charge-coupled device (CCD) camera. The height of the wrinkles is obtained by triangulation of the images obtained. These systems generally only have a small range of measurement (less than 1 mm) and so are only suitable for measuring very fine wrinkles (Fischer *et al.*, 1999).

Another profilometry technique used in skin topography is interference fringe projection (Lagarde *et al.*, 2001) but, as with optical profilometry, the depth of field is very shallow at less than 1 mm.

Laser profilometry methods either use dynamic focussing or the theory of triangulation to provide a three-dimensional measurement of the skin surface (Lagarde *et al.*, 2001). The main advantage of laser profilometry is the large vertical range of measurement – up to 6 mm (Leveque, 1999).

Parameters are calculated from the profiles measured by the different techniques described. The parameters most frequently used to quantify the size of the wrinkles on the skin surface are the same as some of those used to characterise the surface of metals – the average roughness, the maximum peak-to-valley height (or maximum range) and the mean spacing between peaks (Gadelmawla *et al.*, 2002). Hatzis (2004) defined several parameters in relation to the wrinkle volume but calculating them is a lengthy multi-stage procedure requiring the generation of replicas. The parameters have not yet seen wider use.

Some researchers have developed qualitative scales of wrinkling. For example, Lemperle *et al.* (2001) produced a qualitative scale of wrinkling from 0 to 5, where 0 described skin with no wrinkles and 5 described very deep wrinkles and redundant folds. Batisse *et al.* (2002) produced a photographic reference chart with 6 different

levels of wrinkling. While these approaches are useful guides for providing qualitative evaluations of the wrinkles on skin, they cannot be used for obtaining objective quantitative data on wrinkle profiles.

2.6 Aim, hypothesis and objectives of the thesis

Although there are numerous models of soft tissues that can be applied to skin, they are mostly single-layer models that ignore the individual contribution of each layer in the skin. Many of the multi-layer models have been developed for fingertip applications and assume isotropic linear elastic properties for each skin layer.

Despite there being a large body of work on the study of wrinkling, there is a dearth of studies in the literature that model the wrinkling of skin. The existing models of skin wrinkling assume linear elastic material properties for each layer; ignore anisotropy and viscoelasticity; and also ignore the prestress or resting tension inherent in living human skin. There is also little or no validation of the wrinkling models against experimental tests.

Human skin is a non-linear, orthotropic and viscoelastic material. Equally important is the fact that the different layers of skin have distinct mechanical properties. Therefore, any model of skin should take those factors into consideration in order to make realistic predictions as to the behaviour of skin under wrinkling conditions.

The aim of this thesis is to develop a more realistic model than available in the literature of the mechanical behaviour of skin when it is subjected to loads and deformations that cause it to wrinkle.

It is hypothesised that in order to accurately simulate the wrinkling of skin, it is necessary to have a multi-layer model representing the epidermis, dermis and hypodermis. In addition to this, a constitutive model that accounts for the orthotropic and viscoelastic properties is necessary to accurately represent the dermis. It is further hypothesised that the pretension in skin is also an important parameter that may have a strong influence on the characteristics of the wrinkles.

In order to achieve these hypotheses, several objectives were defined:

The first objective was the development of a mechanical model of skin. The model would be multi-layer consisting of the epidermis, dermis and underlying hypodermis. It would also be orthotropic and viscoelastic.

The second objective was to evaluate the model. The model would be tested against (a) experimental results in the literature and (b) experiments developed in this study that wrinkle skin under controlled conditions.

The third objective was to apply the model to the case-study of a healing scar. The accuracy of the model was evaluated using (a) experiments and models in the literature and (b) experimental models of healing scars developed in this study.

Chapter 3

Development of Theoretical Models

3.1 Introduction

In this chapter, the models used for the various layers in the skin and hypodermis are developed. The models are used to simulate experiments on skin in the literature. They are evaluated by comparing their results with those of the experiments and, in some cases, other previously published models. Details on the implementation of the models into finite element analyses are also given.

3.2 Modelling the epidermis

As mentioned in Sections 2.2.1 and 2.3.1, the stratum corneum is the thickest of the epidermal layers and is also the major load bearing component of the epidermis. For this reason and also the lack of experimental data, the 'living' or 'viable' epidermis is ignored and only the stratum corneum is included in the skin model.

3.2.1 Modelling the stratum corneum

For the constitutive model of the stratum corneum, the material is assumed to be isotropic and viscoelastic effects are negligible. This follows the observations of Koutroupi and Barbenal (1990) in their tests on human stratum corneum. Figure 3.1 shows a uniaxial stress-strain response of human stratum corneum from their experiments.

The neo-Hookean hyperelastic function is chosen to model the stratum corneum, assuming the material has a linear stress-strain response. The strain energy potential is given by

$$W = C_{10}(I_1 - 3) + \frac{1}{D_1}(J - 1)$$

(3.1)

28

where C_{10} and D_1 are material parameters, $J = \lambda_1 \lambda_2 \lambda_3$ is the volume ratio and I_1 is the first strain invariant and is defined using the principal stretches λ_1, λ_2 and λ_3

$$I_1 = \lambda_1^2 + \lambda_2^2 + \lambda_3^2 \tag{3.2}$$

The Cauchy stress is calculated from the relationship $T = \lambda_i / J \dfrac{\partial W}{\partial \lambda_i}$.

3.2.2 Material parameter selection

The material parameters for the neo-Hookean function, C_{10} and D_1, are chosen such that its slope is similar to the slope of the experimental data at strains greater than 1%. In this case the experimental data is the uniaxial stress-strain data of Koutroupi and Barbenal (1990) shown in Figure 3.1. C_{10} can be converted to a Young's modulus, E, by the relation $E = 6C_{10}$. In this case, the equivalent Young's modulus is 240 MPa for the neo-Hookean model.

3.2.3 Varying the mechanical properties of the stratum corneum model

In Section 2.3.1, it was mentioned that the mechanical properties of the stratum corneum vary according to its level of hydration. The Young's Modulus of the stratum corneum ranges from 5 MPa to about 4 GPa. Therefore, when evaluating the multi-layer model of skin, it would be necessary to vary the properties of the stratum corneum to quantify its effect on the behaviour of the whole skin. Table 3.1 show the material parameters for the stratum corneum at different relative humidities.
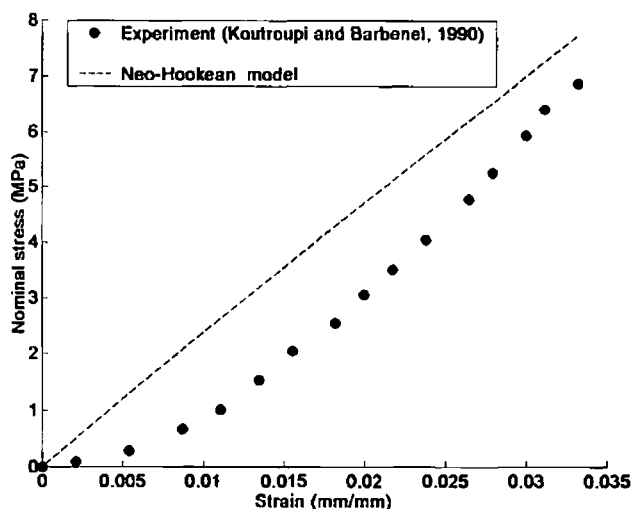
Figure 3.1: Uniaxial tensile tests of human stratum corneum. Neo-Hookean model parameters are in Table 3.1

Table 3.1: Material parameters for the stratum corneum at different relative humidities and Young's Moduli. Source of the RH and Young's Modulus data can be found in

RH (%)	Young's Modulus (MPa)	C_{10} (MPa)	D_1 (MPa)
30	960	160	0.00025
75	240	40	0.00101
100	6	1	0.0405

3.3 Modelling the dermis

As discussed in Section 2.3.2, the dermis has a non-linear stress-strain response and displays orthotropic and viscoelastic characteristics. The constitutive model that will be developed in the following sections is very similar to the rheological network model proposed by Bischoff *et al.* (2004). The differences in the model will be discussed where they arise.

3.3.1 Constitutive model development

In developing an orthotropic viscoelastic constitutive model for skin it is treated as a continuum consisting of two networks acting in unison. A simplified rheological representation of the model is shown in Figure 3.2. This is a similar approach to that taken by Bergstrom and Boyce (1998) when developing their isotropic viscoelastic model for elastomers and soft biological tissues. Network A represents a portion of the collagen-elastin fibres in the dermal layer that are in equilibrium. Network B represents the fraction of the collagen fibres in skin that are moving relative to the ground substance and other collagen fibres to achieve a lower stress state.

The total Cauchy stress acting on the skin is the sum of the stresses in each network

$$T = T_A + T_B \tag{3.3}$$

The total deformation gradient, F, is equal to the deformation gradients in each network

$$F = F_A = F_B \tag{3.4}$$

The model will be described by first developing the constitutive relationships in Network A and then developing the kinematic and constitutive relationships in Network B.

30
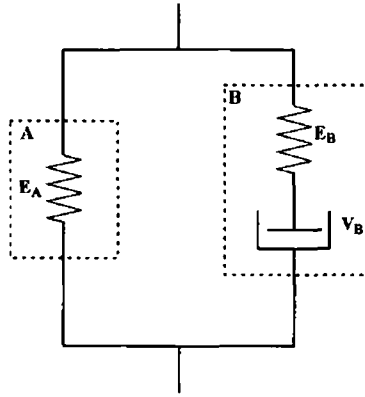
Figure 3.2: Rheological representation of skin showing two networks acting in unison

Constitutive behaviour of network A

Network A consists of a hyperelastic element and is the same as that developed by Bischoff *et al.* (2002a). The element is based on an assembly of eight fibres within a unit cell as in Figure 3.3(a). One end of each fibre is fixed to the corner of the cell while the other end is fixed to a point in the centre of the cell. The cell's orientation is specified initially by the unit vectors **a**, **b** and **c**, and rotates affinely with the imposed deformation. The orientation and dimensions of the cell contribute to the orthotropic nature.

Each individual fibre in the cell is assumed to contain N_A freely jointed rigid links each of length l as in Figure 3.3(b). The undeformed and deformed fibre lengths (r and R, respectively) are normalised with respect to the rigid link length l, such that $\rho_A = r/l$ and $P = R/l$. The vector descriptions $P_A^{(i)}$ of each of the fibres in the undeformed unit cell where i denotes the fibre number are

$$P_A^{(1)} = -P_A^{(5)} = \frac{a_A}{2} a_A + \frac{b_A}{2} b_A + \frac{c_A}{2} c_A$$

$$P_A^{(2)} = -P_A^{(6)} = \frac{a_A}{2} a_A + \frac{b_A}{2} b_A - \frac{c_A}{2} c_A$$

$$P_A^{(3)} = -P_A^{(7)} = \frac{a_A}{2} a_A - \frac{b_A}{2} b_A + \frac{c_A}{2} c_A \tag{3.5}$$

$$P_A^{(4)} = -P_A^{(8)} = \frac{a_A}{2} a_A - \frac{b_A}{2} b_A - \frac{c_A}{2} c_A$$

The normalised undeformed length of each fibre can be found from the geometry of the unit cell and is
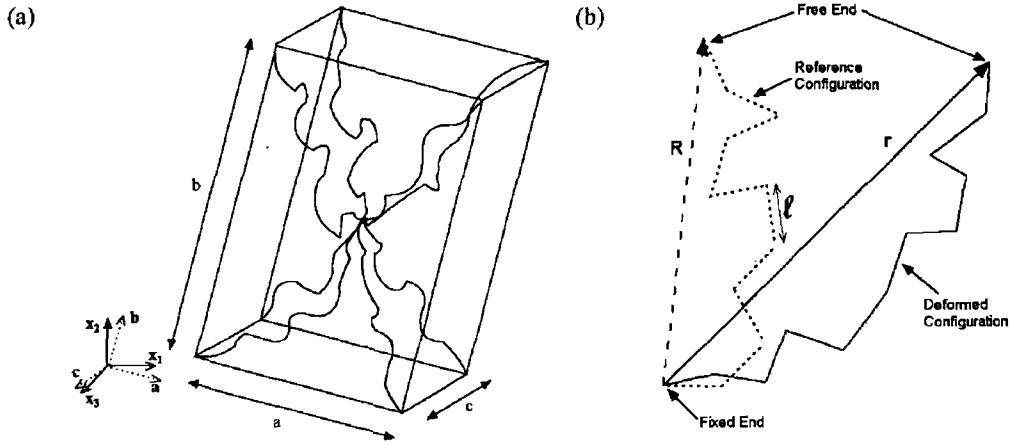
Figure 3.3: (a) 8-chain, three-dimensional orthotropic unit cell; (b) representation of a single fibre as a series of N freely jointed links of length l (adapted from Bischoff *et al.* (2002a))

$$P_A = \frac{1}{2}\sqrt{a_A^2 + b_A^2 + c_A^2} \qquad (3.6)$$

It is assumed that the undeformed length of each fibre is equal to the root-mean-square of the undeformed fibre length so that $\sqrt{N_A} = P_A = \sqrt{a_A^2 + b_A^2 + c_A^2}/2$. The deformed length, $\rho_A^{(i)}$, of each fibre is

$$\rho_A^{(i)} = \sqrt{\mathbf{P}_A^{(i)\mathrm{T}}\mathbf{C}_A\mathbf{P}_A^{(i)}} \qquad (3.7)$$

where $\mathbf{C}_A = \mathbf{F}_A^{\mathrm{T}}\mathbf{F}_A$ is the right Cauchy-Green strain tensor for Network A.

Bischoff *et al.* (2004) derived the model using the deviatoric components of the deformation gradient given by

$$\widetilde{\mathbf{F}}_A = J^{-1/3}\mathbf{F}_A \qquad (3.8)$$

The right Cauchy-Green strain tensor is then given by $\widetilde{\mathbf{C}}_A = \widetilde{\mathbf{F}}_A^{\mathrm{T}}\widetilde{\mathbf{F}}_A$. The deformed fibre length in terms of deviatoric components, $\widetilde{\rho}_A^{(i)}$ is related to Equation 3.7 by

$$\widetilde{\rho}_A^{(i)} = J^{-1/3}\rho_A^{(i)} \qquad (3.9)$$

Deriving the model in this way, results in a strain energy function consisting of volume-changing and volume-preserving components. While this approach can avoid possible numerical difficulties when modelling almost incompressible materials such as soft tissues (Holzapfel, 2000), it is still valid to derive the model by not decomposing the deformation gradient into deviatoric and volumetric components (Bergstrom and Boyce, 1998). With this in mind, the orthotropic-viscoelastic model

32

derived in this section does not use the deviatoric components of the deformation gradient.

Referring back to Figure 3.3(b), in the undeformed state one end of the fibre is fixed while the other end is located at **R**. Next consider the fibre is deformed and the probability that the free end occupies a volume dv at a location **r** as developed by Kuhn and Grun (1942, cited in Bischoff *et al.* (2002)) is given by the non-Gaussian probability distribution function

$$\ln p(r) = p_0 - N\left(\frac{r}{Nl}\beta_r + \ln\frac{\beta_r}{\sinh\beta_r}\right)$$ (3.10)

where p_0 is a constant, $r = |\mathbf{r}|$, $\beta_r = L^{-1}(r/Nl)$, and $L(x) = \coth x - 1/x$ is the Langevin function.

Gaussian statistics are employed in constitutive models when there are only small extensions of the fibre. For larger extensions of the fibre, non-Gaussian or Langevin statistics must be used in order to preserve accuracy. The inverse Langevin function β_r is shown in Figure 3.4. As r/Nl approaches unity, β increases towards infinity.

The entropy of the fibre is a function of the number of possible configurations it can take and is given by

$$s_{fibre} = k\ln\Omega$$ (3.11)

where k is the Boltzman's constant and is equal to 1.38×10^{-23} J/K and Ω is the number of possible configurations of the fibre. The number of configurations is proportional to the probability $p(r)$ so from Equations 3.10 and 3.11

$$s_{fibre} = k\left[C - N\left(\frac{r}{Nl}\beta_r + \ln\frac{\beta_r}{\sinh\beta_r}\right)\right]$$ (3.12)

where C is a constant.

The change in entropy of the fibre when brought from the undeformed state to the deformed state is

$$\Delta s_{fibre} = k\left[N\left(\frac{R}{Nl}\beta_R + \ln\frac{\beta_R}{\sinh\beta_R}\right) - N\left(\frac{r}{Nl}\beta_r + \ln\frac{\beta_r}{\sinh\beta_r}\right)\right]$$ (3.13)

From thermodynamics, the change in strain energy of the fibre when brought from the undeformed to the deformed state is given by

$$\Delta w = -\theta\Delta s_{fibre}$$ (3.14)

33
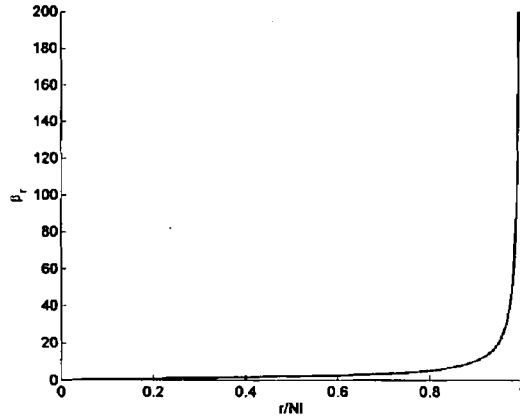
Figure 3.4: Inverse Langevin function

where θ is the absolute temperature. Substituting 3.13 into 3.14 gives the change in strain energy of an individual fibre when brought from the undeformed to the deformed state

$$\Delta w(r) = k\theta N \left[\left(\frac{r}{Nl}\beta_r + \ln\frac{\beta_r}{\sinh\beta_r} \right) - \left(\frac{R}{Nl}\beta_R + \ln\frac{\beta_R}{\sinh\beta_R} \right) \right] \qquad (3.15)$$

Normalising the deformed and undeformed fibre lengths such that $\rho = r/l$ and $P = R/l$ gives

$$\Delta w(\rho) = k\theta N \left[\left(\frac{\rho}{N}\beta_\rho + \ln\frac{\beta_\rho}{\sinh\beta_\rho} \right) - \left(\frac{P}{N}\beta_P + \ln\frac{\beta_P}{\sinh\beta_P} \right) \right] \qquad (3.16)$$

From symmetry arguments the strain energy of all the fibres in the unit cell is

$$w_{entropy} = w_0 + 2\sum_i^4 w(\rho^{(i)}) \qquad (3.17)$$

where w_0 is the non-zero strain energy of the undeformed fibres.

An examination of Equation 3.16 shows that strain energy of a fibre $w(\rho)$ is a monotonically increasing function. Examining Equation 3.17 it is seen that $w_{entropy}$ is minimised when $\rho^{(i)}$ is zero. In general a body is in a stress-free state when the strain energy is minimised. Physically, the unit cell is in a stress-free state when the eight fibres are at their undeformed lengths. Therefore, the strain energy of the unit cell should be at a minimum when the fibres are undeformed. If not then this is a physically unrealistic situation. To enforce this requirement an extra term is added to Equation 3.17. This term is denoted $w_{repulsion}$ as it represents a mutual repulsion of the fibres from one another. It is given by

34

$$W_{repulsion} = -\frac{2}{P}\left(\frac{dw(\rho)}{d\rho}\right)_{\rho=P} \ln\left(\lambda_a^{a^2} \lambda_b^{b^2} \lambda_c^{c^2}\right) \qquad (3.18)$$

where $\lambda_a = \sqrt{\mathbf{a^T Ca}}$, $\lambda_b = \sqrt{\mathbf{b^T Cb}}$, and $\lambda_c = \sqrt{\mathbf{c^T Cc}}$ represent the stretches along the principal material axes. The strain energy of the unit cell is therefore

$$w = w_0 + 2\sum_i^4 w(\rho^{(i)}) - \frac{2}{P}\left(\frac{dw(\rho)}{d\rho}\right)_{\rho=P} \ln\left(\lambda_a^{a^2} \lambda_b^{b^2} \lambda_c^{c^2}\right) \qquad (3.19)$$

The unit cell in Figure 3.3(a) can be homogenised to form a macroscopic three-dimensional strain energy function. Assuming a fibre density of n fibres per unit volume and noting that there are eight chains per cell, the strain energy per unit volume is given by

$$W = \frac{n}{8}\left(w_{entropy} + w_{repulsion}\right) \qquad (3.20)$$

A bulk compressibility term is added to account for the ground substance in the skin. This expression takes the form

$$W_{Bulk} = \frac{B}{\alpha^2}\{\cosh[\alpha(J-1)]-1\} \qquad (3.21)$$

where B is the bulk modulus and $J = \det \mathbf{F}$ is the volume change associated with the deformation. Skin is almost incompressible so α is set equal to unity. Substituting Equations 3.19 into 3.20 and adding Equation 3.21 gives the strain energy function per unit volume

$$W(x) = W_0 + \frac{n}{4}\left[\sum_i^4 w(\rho^{(i)}) - \frac{1}{P}\left(\frac{dw(\rho)}{d\rho}\right)_{\rho=P} \ln\left(\lambda_a^{a^2} \lambda_b^{b^2} \lambda_c^{c^2}\right)\right] + B\{\cosh(J-1)-1\} \qquad (3.22)$$

where W_0 is a constant related to the strain energy of undeformed fibres.

Substituting for the strain energy function of a fibre, $w(\rho^{(i)})$, from Equation 3.16 into Equation 3.22 gives the final form of the strain energy function developed by Bischoff et al. (2002)

$$W_A(x) = W_{A0} + \frac{n_A k\theta}{4}\left[N_A \sum_i^4 \left(\frac{\rho_A^{(i)}}{N_A}\beta_{\rho A}^{(i)} + \ln\frac{\beta_{\rho A}^{(i)}}{\sinh\beta_{\rho A}^{(i)}}\right) - \frac{\beta_{P_A}}{P_A}\ln\left(\lambda_{Aa_A}^{a_A^2} \lambda_{Ab_A}^{b_A^2} \lambda_{Ac_A}^{c_A^2}\right)\right] +$$
$$B\{\cosh(J_A - 1)-1\} \qquad (3.23)$$

where A refers to Network A. The second Piola-Kirchhoff stress tensor is given by

$$\mathbf{S}_A = \frac{dW_A}{d\mathbf{E}_A} \qquad (3.24)$$

where $E_A = \frac{1}{2}\left(F_A^T F_A - I\right)$ is the Lagrangian strain field for Network A. The Cauchy stress tensor T_A can be calculated from the second Piola-Kirchhoff stress tensor as

$$T_A = \frac{1}{J_A} F_A S_A F_A^T \qquad (3.25)$$

Constitutive behaviour of network B

Network B is also based on an assembly of eight fibres within a unit cell. It has material axes (a_B, b_B and c_B) and dimensions (a_B, b_B and c_B). Similarly to Network A, each fibre is assumed to contain N_B rigid links of length l. Therefore the normalised vector description and length of the fibres are similar to Equations 3.5 and 3.6. The deformation gradient of Network B, F_B, can be further decomposed into an elastic and viscous component

$$F_B = F_{Be} F_{Bv} \qquad (3.26)$$

where F_{Be} and F_{Bv} are the deformation gradients for the elastic and viscous elements in Network B respectively.

Concentrating on the elastic element of Network B, its normalised deformed length, $\rho_{Be}^{(i)}$, is given by

$$\rho_{Be}^{(i)} = \sqrt{P_B^{(i)T} C_{Be} P_B^{(i)}} \qquad (3.27)$$

where $C_{Be} = F_{Be}^T F_{Be}$ is the right Cauchy-Green strain tensor for the elastic element in Network B.

Similar to the deformation gradient in Network A, Bischoff *et al.* (2004) used the deviatoric components of the deformation gradient such that

$$\tilde{F}_{Be} = J^{-1/3} F_{Be} \qquad (3.28)$$

As with the constitutive model development of Network A, this approach was not taken in the current development – the only disadvantage being the possible numerical difficulties at very large strains.

A strain energy function for the elastic element in Network B can be derived in a similar manner to the elastic element for Network A and is given by

36

$$W_{Be}(x) = W_{Be0} +$$

$$\frac{n_B k\theta}{4}\left[N_B \sum_i^4 \left(\frac{\rho_{Be}^{(i)}}{N_B}\beta_{\rho Be}^{(i)} + \ln\frac{\beta_{\rho Be}^{(i)}}{\sinh\beta_{\rho Be}^{(i)}}\right) - \frac{\beta_{P_B}}{P_B}\ln\left(\lambda_{Bea_B}^{a_B^2}\lambda_{Beb_B}^{b_B^2}\lambda_{Bec_B}^{c_B^2}\right)\right] + \qquad (3.29)$$

$$B\{\cosh(J_{Be}-1)-1\}$$

where all terms have similar meanings to the corresponding terms for Network A. Using Equation 3.29, the second Piola-Kirchhoff stress tensor in Network B is

$$\mathbf{S}_B = \frac{dW_{Be}}{d\mathbf{E}_{Be}} \qquad (3.30)$$

where $\mathbf{E}_{Be} = \frac{1}{2}\left(\mathbf{F}_{Be}^T\mathbf{F}_{Be} - \mathbf{I}\right)$ is the Lagrangian strain field for the elastic element in Network B. The Cauchy stress tensor $\mathbf{T}_B$ can be calculated from the second Piola-Kirchhoff stress tensor as

$$\mathbf{T}_B = \frac{1}{J_{Be}}\mathbf{F}_{Be}\mathbf{S}_B\mathbf{F}_{Be}^T \qquad (3.31)$$

In order for Equation 3.31 to be evaluated the deformation gradient $\mathbf{F}_{Be}$ needs to be determined. The total velocity gradient of Network B is

$$\mathbf{L}_B = \dot{\mathbf{F}}_B\mathbf{F}_B^{-1} \qquad (3.32)$$

where $\dot{\mathbf{F}}_B = \frac{\partial \mathbf{F}_B}{\partial t}$.

This velocity gradient can be decomposed into elastic and viscous components

$$\mathbf{L}_B = \mathbf{L}_{Be} + \mathbf{L}_{Bv} \qquad (3.33)$$

Substituting 3.26 into 3.32 and comparing with 3.33 gives

$$\mathbf{L}_{Be} = \dot{\mathbf{F}}_{Be}\mathbf{F}_{Be}^{-1} \qquad (3.34)$$

$$\mathbf{L}_{Bv} = \mathbf{F}_{Be}\dot{\mathbf{F}}_{Bv}\mathbf{F}_{Bv}^{-1}\mathbf{F}_{Be}^{-1} \qquad (3.35)$$

The velocity gradient can be decomposed into a symmetric part $\mathbf{D}_{Bv}$ and a skew-symmetric part $\mathbf{W}_{Bv}$ such that

$$\mathbf{L}_{Bv} = \mathbf{D}_{Bv} + \mathbf{W}_{Bv} \qquad (3.36)$$

$\mathbf{D}_{Bv}$ is the rate of deformation tensor and $\mathbf{W}_{Bv}$ is the spin tensor of Network B. Following Boyce et al. (1989), $\mathbf{W}_{Bv}$ can be set to zero without loss in generality. Equating 3.35 and 3.36 and rearranging gives

$$\dot{\mathbf{F}}_{Bv} = \mathbf{F}_{Be}^{-1}\mathbf{D}_{Bv}\mathbf{F}_{Be}\mathbf{F}_{Bv} \qquad (3.37)$$

An expression is needed for the rate of shape change of Network B, $\mathbf{D}_{Bv}$. Bergstrom and Boyce (1998) constitutively prescribed it by

$$\mathbf{D}_{Bv} = \gamma_B \mathbf{N}_B \qquad (3.38)$$

where γ_B is an effective creep rate and $\mathbf{N}_B$ is the direction of the driving stress state and is given by

$$\mathbf{N}_B = \frac{1}{\sqrt{2}\tau_B} \mathbf{T}_B' \qquad (3.39)$$

where $\mathbf{T}_B' = \mathbf{T}_B - trace[\mathbf{T}_B]\mathbf{I}/3$ is the deviatoric part of the driving stress $\mathbf{T}_B$ and $\tau_B = \sqrt{trace[\mathbf{T}_B'\mathbf{T}_B']/2}$ is the equivalent effective shear stress.

The effective creep rate of Network B, γ_B, is derived using reptation theory. A simplified illustration of the process is shown in Figure 3.5. An arbitrary stress is applied to the sample of fibres. In order to achieve a more relaxed state, the highlighted fibres must deform. However, its movement is constrained by the other fibres in the network. It is limited to moving along its length, snake-like, to arrive at a more relaxed configuration. Bergstrom and Boyce (1998) developed an expression for the effective creep rate of polymer fibres that is dependent on the fibre stretch and the stress level in the sample:

$$\gamma_B = C_1 \left[\rho_{Bv}^{(i)} - 1 + \varepsilon \right]^{C_2} \tau_B^m \qquad (3.40)$$

where $\rho_{Bv}^{(i)} = \sqrt{trace(\mathbf{F}_{Bv}\mathbf{F}_{Bv}^T)/3}$ is the normalised deformed length of the viscous element in Network B. C_1, C_2, and m are material constants. Both C_1 and m are positive, while C_2 lies between 0 and -1. ε is a parameter introduced to avoid

(a) Deformed network of fibres at time t (b) Deformed network at time $t+dt$
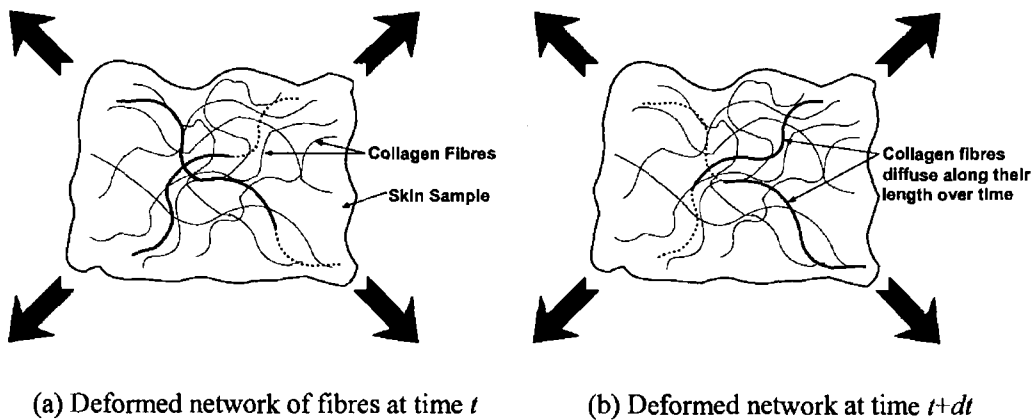
Figure 3.5: Reptation theory: Skin sample under an arbitrary stress; over time the collagen fibres diffuse along their lengths to achieve a more relaxed state

numerical difficulties when $\rho_{Bv}^{(i)}$ is close to 1.0 (Bergstrom and Boyce, 2001). It is usually set to 0.001.

To summarise, when a skin sample is strained a deformation field develops given by Equation 3.4. The total stress in the skin sample is given by the sum of the stresses in the collagen Networks A and B, which are given by Equations 3.25 and 3.31 respectively. The creep rate of the collagen fibres in Network B is found using Equation 3.40 which enables the velocity gradient to be calculated using Equation 3.37. Integrating the velocity gradient gives the deformation gradient of the viscous component of B allowing an updated elastic component of the deformation gradient to be calculated using Equation 3.26.

3.3.2 Application of the constitutive model

The orthotropic viscoelastic model developed in the previous section is used to simulate several uniaxial and biaxial tests. The experimental data is taken from the rabbit skin tests of Lanir and Fung (1974), the human skin tests of Schneider (1982) and Wan Abas (1994), the pig skin tests of Ankerson *et al.* (1999) and Shergold *et al.* (2006) and also compression tests of monkey liver reported in Miller (2000) following Bergstrom and Boyce (2001). The equations of the model developed above are first applied to the specific cases of uniaxial and biaxial deformation.

Uniaxial and biaxial deformation

For both uniaxial and biaxial deformations where the model is applied, the material axes (a_A, b_A, c_A) and (a_B, b_B, c_B) are aligned with the global coordinate axes (X_1, X_2, X_3). The total deformation gradient is given by

$$\mathbf{F} = \begin{pmatrix} \lambda_1 & 0 & 0 \\ 0 & \lambda_2 & 0 \\ 0 & 0 & \lambda_3 \end{pmatrix} \quad (3.41)$$

where λ_1, λ_2 and λ_2 are the principal material stretches.

Since $\mathbf{F} = \mathbf{F}_A$, substituting 3.41 into 3.25 gives the Cauchy stresses in Network A

$$T_{A11} = \frac{n_A k \theta a_A^2}{4 J_A} \left[\frac{\lambda_1^2 \beta_{\rho_A}}{\rho_A} - \frac{\beta_{P_A}}{\sqrt{N_A}} \right] + B \sinh(J_A - 1)$$

$$\quad (3.42)$$

$$T_{A22} = \frac{n_A k \theta b_A^2}{4 J_A} \left[\frac{\lambda_2^2 \beta_{\rho_A}}{\rho_A} - \frac{\beta_{P_A}}{\sqrt{N_A}} \right] + B \sinh(J_A - 1)$$

39

$$T_{A33} = \frac{n_A k\theta c_A^2}{4J_A}\left[\frac{\lambda_3^2 \beta_{\rho_A}}{\rho_A} - \frac{\beta_{P_A}}{\sqrt{N_A}}\right] + B\sinh(J_A - 1)$$

From Equation 3.7 the normalised deformed length of all eight fibres in Network A are equal and is

$$\rho_A = \frac{\sqrt{a_A^2 \lambda_1^2 + b_A^2 \lambda_2^2 + c_A^2 \lambda_3^2}}{2} \tag{3.43}$$

From Equations 3.4, 3.26 and 3.41 it can be shown that

$$\lambda_i = \lambda_{Bei}\lambda_{Bvi} ; \quad i = 1,2,3 \tag{3.44}$$

where λ_{Bei} and λ_{Bvi} are the elastic and viscoelastic components of the principal material stretches of Network B respectively.

The Cauchy stresses in Network B can be calculated in a similar manner to Network A and are given by

$$T_{B11} = \frac{n_B k\theta a_B^2}{4J_{Be}}\left[\frac{\lambda_{Be1}^2 \beta_{\rho_{Be}}}{\rho_{Be}} - \frac{\beta_{P_B}}{\sqrt{N_B}}\right] + B\sinh(J_{Be} - 1)$$

$$T_{B22} = \frac{n_B k\theta b_B^2}{4J_{Be}}\left[\frac{\lambda_{Be2}^2 \beta_{\rho_{Be}}}{\rho_{Be}} - \frac{\beta_{P_B}}{\sqrt{N_B}}\right] + B\sinh(J_{Be} - 1) \tag{3.45}$$

$$T_{B33} = \frac{n_B k\theta c_B^2}{4J_{Be}}\left[\frac{\lambda_{Be3}^2 \beta_{\rho_{Be}}}{\rho_{Be}} - \frac{\beta_{P_B}}{\sqrt{N_B}}\right] + B\sinh(J_{Be} - 1)$$

where $\rho_{Be} = \sqrt{a_B^2 \lambda_1^2 + b_B^2 \lambda_2^2 + c_B^2 \lambda_3^2}\big/2$ is the deformed elastic length of Network B.

Equations 3.37, 3.38 and 3.39 yield rate expressions for the viscoelastic component of the principal stretches

$$\dot{\lambda}_{Bv1} = \frac{\gamma_B}{\sqrt{2}\tau_B} T_{B11}'\lambda_{Bv1}$$

$$\dot{\lambda}_{Bv2} = \frac{\gamma_B}{\sqrt{2}\tau_B} T_{B22}'\lambda_{Bv2} \tag{3.46}$$

$$\dot{\lambda}_{Bv3} = \frac{\gamma_B}{\sqrt{2}\tau_B} T_{B33}'\lambda_{Bv3}$$

where $T_{B11}' = \frac{2T_{B11} - T_{B22} - T_{B33}}{3}, T_{B11}' = \frac{-T_{B11} + 2T_{B22} - T_{B33}}{3}$ and $T_{B33}' = \frac{-T_{B11} - T_{B22} + 2T_{B33}}{3}$.

The creep rate of Network B is given by Equation 3.40 and the normalised deformed length of the viscous element is

40

$$\rho_{Bv} = \sqrt{\frac{\lambda_{Bv1}^2 + \lambda_{Bv2}^2 + \lambda_{Bv3}^2}{3}} \qquad (3.47)$$

The above equations are solved for the total Cauchy stress given an applied stretch λ_l in uniaxial and biaxial extension. The procedure during a given time-step is given in Figure 3.6.
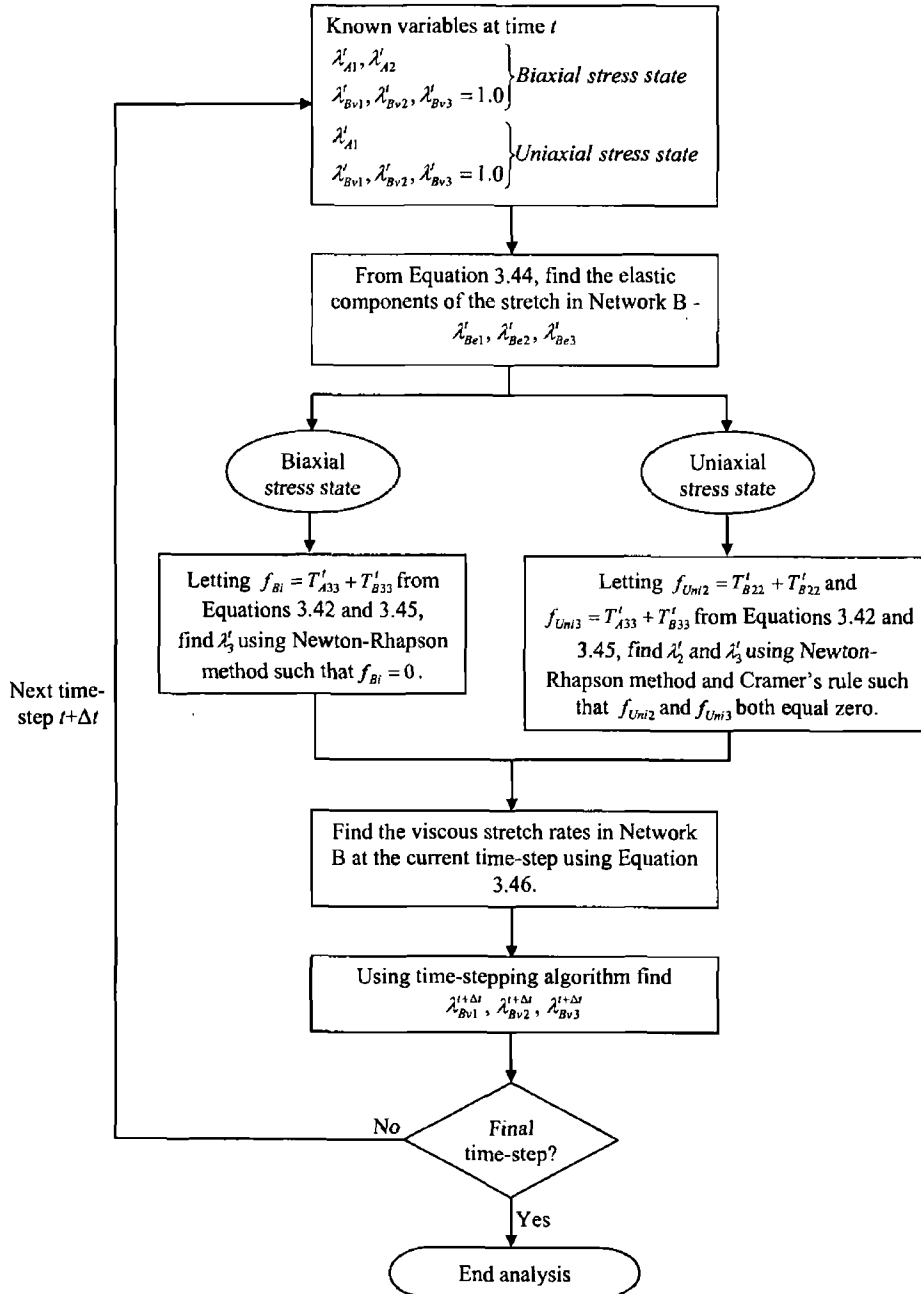
Figure 3.6: Sequence of steps for solving uniaxial and biaxial deformations

41

Uniaxial and biaxial stretching of rabbit skin in vitro

The model was fitted to experimental data from a series of *in vitro* uniaxial and biaxial tests on rabbit skin (Lanir and Fung, 1974). The skin specimens were fully relaxed before any loads were applied. For the uniaxial tests the specimen was stretched in one direction while no load was applied in the other direction. For the biaxial test the specimen was stretched in one direction while the dimension in the other direction was held constant. The rate of stretching was assumed to have been 2 mms^{-1} although Lanir and Fung (1974) state that three strain-rates of 0.02, 0.2 and 2.0 mms^{-1} were used. The orthotropic nature of the skin was demonstrated by applying the stretch in the longitudinal direction and then the transverse direction. The width and length of the sample was 35 mm. The thickness of the sample was not stated in the paper, and it was assumed to have been 1.5 mm. The results of the fitting of the orthotropic-viscoelastic model to the experimental data are shown in Figure 3.7(a) and Figure 3.7(b), along with the material parameters. The parameter values were adjusted iteratively so that the error between the model and experiment were minimised. This was achieved with the aid of the FMINSEARCH function in MATLAB Version 6.5 (The MathWorks, Inc., Natick, MA, USA), which uses the Nelder-Mead simplex method to find the minimum of a function of several variables. The Nelder-Mead algorithm is explained in more detail in Appendix D. The error between the experimental and predicted data and the R^2 value for the orthotropic-viscoelastic model are given in Table 3.2. The error and R^2 value are defined as

$$Error = \frac{\sum_{i=1}^{N}|P(i) - E(i)|}{\sum_{i=1}^{N}|P(i)|} \times 100\% \qquad (3.48)$$

$$R^2 = 1 - \frac{\sum_{i=1}^{N}(P(i) - E(i))^2}{\sum_{i=1}^{N}(P(i) - \overline{E})^2} \qquad (3.49)$$

where N is the number of data points, $P(i)$ is the ith value predicted by the model, $E(i)$ is the corresponding experimental data value and $\overline{E}$ is the mean of the experimental data.
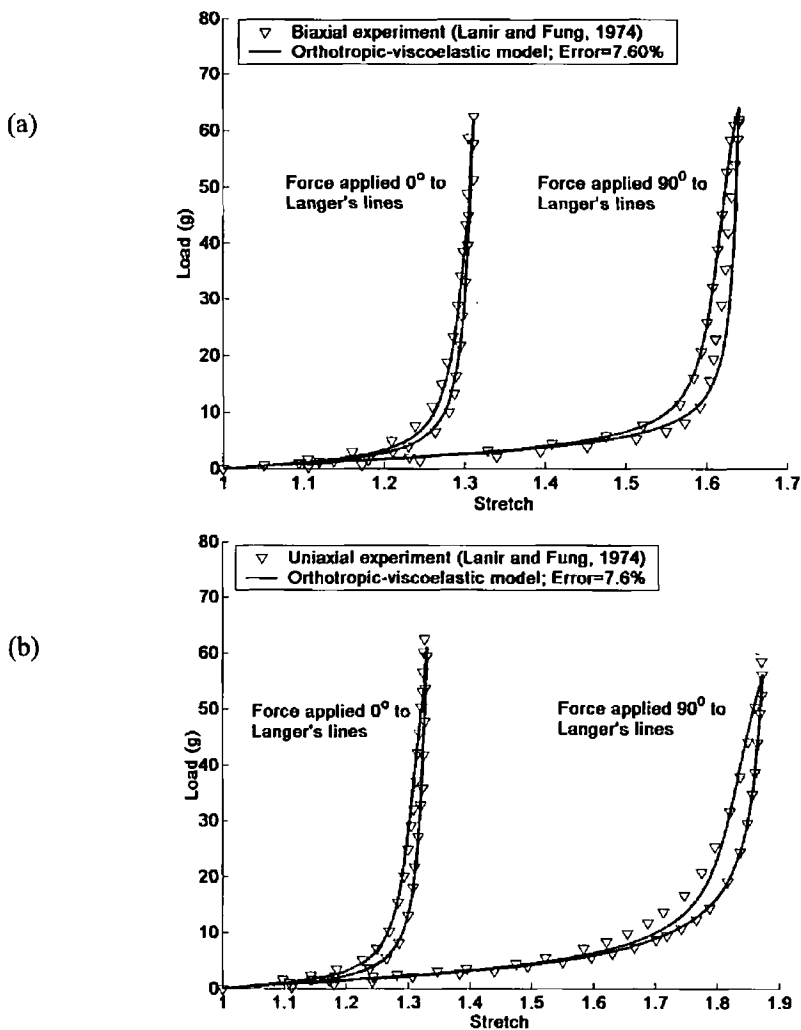
Figure 3.7: Comparison of models to experimental biaxial and uniaxial stretch tests of a rabbit skin sample in two normal directions; Orthotropic-viscoelastic model parameters: $n_A = 3.286 \times 10^{22}$; $n_B = 1.373 \times 10^{22}$; $(a_A, b_A, c_A) = (2.735, 1.385, 1.302)$; $(a_B, b_B, c_B) = (1.059, 1.479, 1.200)$; $B = 50$ kPa; $C_1 = 0.0018186$ s^{-1}(kPa)$^{-m}$; $C_2 = -0.022$; $m = 1.301$

For comparison with other models, the error of fit and the R^2 value of the Bergstrom and Boyce (1998) and the Bischoff et al. (2002a; 2004) models are also displayed in Table 3.2.

Preconditioning

The phenomenon of preconditioning was investigated using the rabbit skin material parameters shown in Figure 3.7. The model was subjected to multiple cycles of uniaxial and biaxial loading both perpendicular to and parallel to the Langer's lines. The strains and strain rate were the same as those used by Lanir and Fung (1974) in

Table 3.2: Error measure and R^2 values, for models applied to rabbit skin experiments of Lanir and Fung (1974). Note that the values of the Bergstrom-Boyce model are calculated for one direction only.

Model	Error (%)	R^2
Orthotropic-viscoelastic	7.6	0.975
Bergstrom and Boyce (2001)	13.8	0.936
Bischoff *et al.* (2002a)	19.5	0.887
Bischoff *et al.* (2004)	30.0	0.79

Figure 3.7. The first seven load-stretch cycles of each test are shown in Figure 3.8. It can be seen that for increasing cycles the level of hysteresis decreases. The slope of the load-stretch curve also decreases resulting in a more compliant skin model. After the seventh cycle, the amount of hysteresis was negligible and the load-stretch curves of each cycle were almost the same.

To investigate the effect of preconditioning on the material parameters, the rabbit skin data in Figure 3.7 was also simulated using a fully-preconditioned model. The results are shown in Figure 3.9(a) and Figure 3.9(b). The model was subjected to twenty cycles of loading and unloading. The strains and strain-rates were the same as before. There was a larger error of fit for the preconditioned model than for the unpreconditioned model of Figure 3.7. The material parameters have also changed significantly. The largest changes were in the viscoelastic parameters – C_1 changed by -95% and C_2 changed by 31%.

Material parameter study

The effect of varying n_A, n_B, C_1, C_2 and m on the response of the model of rabbit skin under uniaxial and biaxial tension was studied. The greater the density of the collagen fibres in the dermis (n_A and n_B), the stiffer the load-stretch response of the model (Figure 3.10(a) and Figure 3.10(b)). In addition, as n_B increased relative to n_A, a greater amount of hysteresis was observed in the loading cycle due to there being a greater density of fibres reptating in the network. Increasing the viscoelastic parameters C_1, C_2 and m had the effect of reducing the overall stress in the sample in the locking region (Figure 3.10(c), Figure 3.10(d) and Figure 3.10(e)). Studying Equation 3.40, an increase in any of these three parameters increases the creep rate of the fibres in the viscoelastic network thus reducing the stress. These parameters have
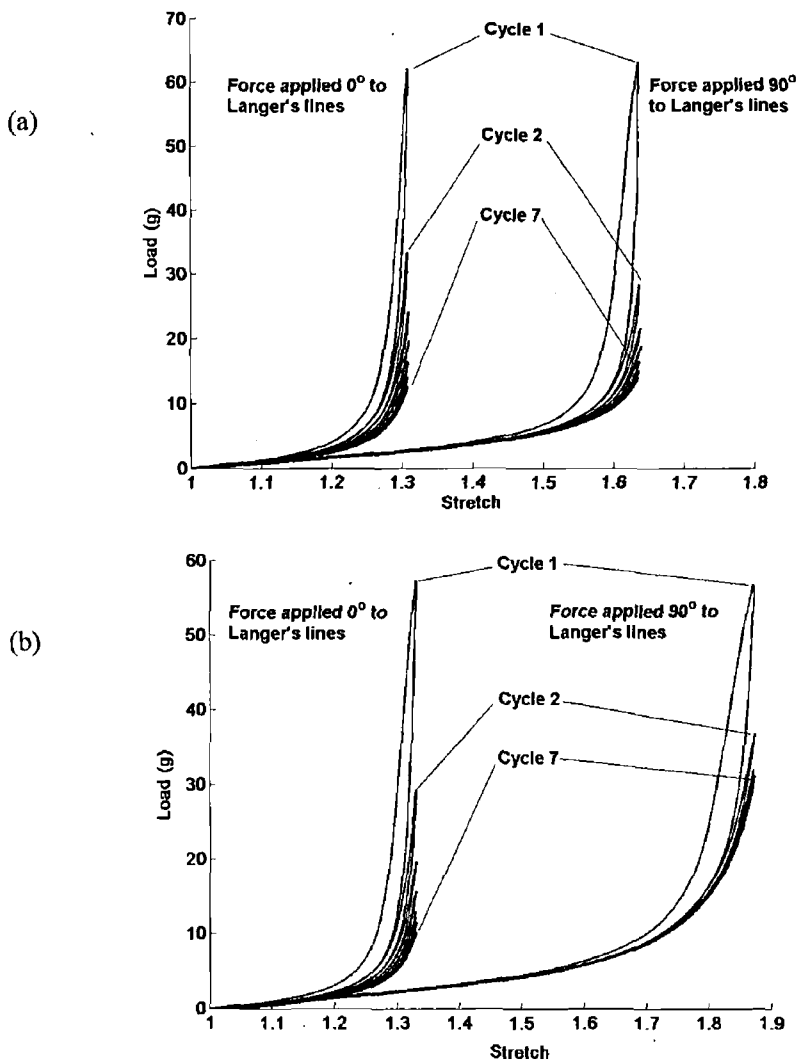
Figure 3.8: Demonstrating preconditioning in the skin model by subjecting the rabbit skin model to multiple cycles of (a) biaxial and (b) uniaxial loading. The material parameters of the model and the strains and strain-rates were the same as those used in Figure 3.7.

little significant effect on the load response outside of the locking region. It is noted that the response of the model is more sensitive to changes in C_1 than C_2. Also m has a significantly greater effect on the level of hysteresis in the load-stretch response than either C_1 or C_2.

It was mentioned earlier that the thickness of the rabbit skin was assumed to be 1.5 mm and the strain rate of the stretch tests was 2.0 mms^{-1}. To investigate the effect these assumptions had on the material parameters, the orthotropic-viscoelastic model was fitted to the experimental data in Figure 3.7 assuming different experimental conditions. These were (1) a strain-rate of 0.2 mms^{-1}; (2) a strain-rate of 0.02 mms^{-1};
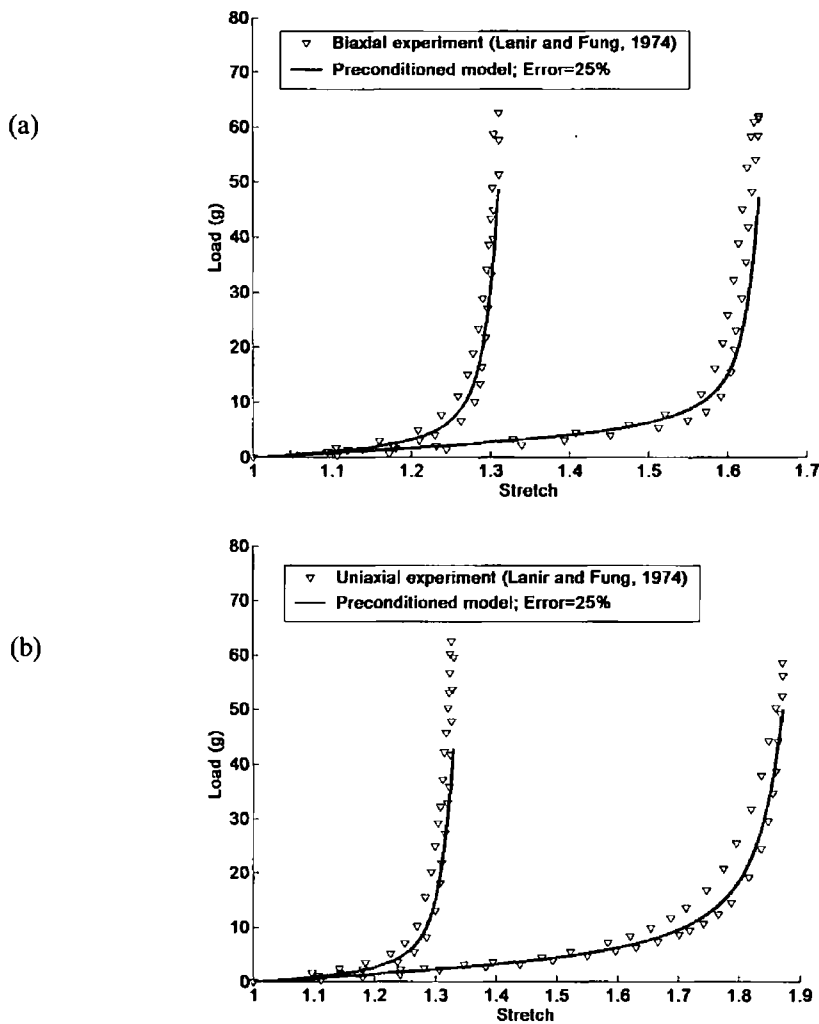
Figure 3.9: Fitting preconditioned model to stretch tests of rabbit skin; Orthotropic-viscoelastic model parameters: n_A= 3.507x10^{22} (7%); n_B=1.468x10^{22} (7%); (a_A,b_A,c_A)= (2.619,1.384,1.357) (4%, 0%, 4%); (a_B,b_B,c_B)= (1.074,1.404,1.216) (1%, -5%, 1%); B=50 kPa (0%); C_1=0.00008653 s^{-1}(kPa)$^{-m}$ (-95%); C_2=-0.015 (31%); m=1.301 (0%). The percentages refer to the change in the parameter value compared to the corresponding value in Figure 3.7.

(3) a skin thickness of 1.0 mm; (4) a skin thickness of 2.0 mm. The percentage changes to the material parameters in Figure 3.7 that were required to fit the model to the experimental data under these modified conditions are shown in Table 3.3. No changes were made to (a_A, b_A, c_A) and (a_B, b_B, c_B) as these parameters only change the location of the locking region. No change was made to the bulk modulus B. Reducing the strain-rate of the experiment required a decrease in the creep-rate of the fibres, γ_B, and so C_1 was reduced. A skin sample that is 1.0 mm thick and generates the load-stretch response in Figure 3.7 is stiffer than a thicker skin that generates the same load-stretch response. This is reflected in Table 3.3 with an increase in n_A and n_B.

46
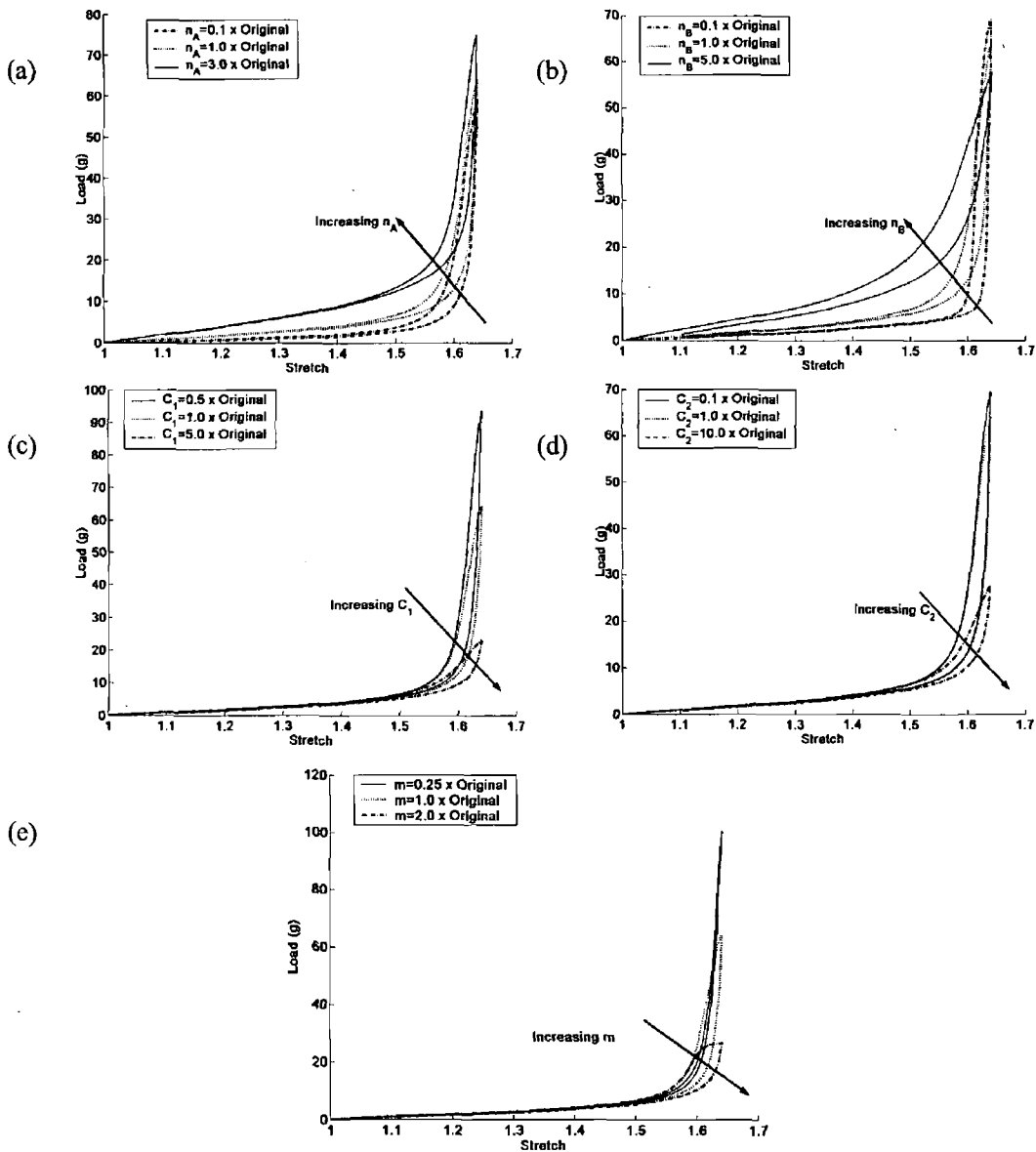
Figure 3.10: The effect of varying some of the material parameters of the orthotropic-viscoelastic model. The load-stretch curves are the simulated response of the biaxial stretch test of rabbit skin when the load is applied in the direction along the length of the body. Unless otherwise stated, the values of the material parameters are the same as in Figure 3.7. The thickness of the skin was assumed to be 1.5 mm and the strain rate 2.0 mms^{-1}.

After adjusting n_A and n_B, the model matched the experimental data closely outside the locking region but the load predicted by the model was too small inside the locking region. Therefore, C_1 and C_2 were decreased to get a better match inside the locking region. A final adjustment to m resulted in better agreement in the level of hysteresis between the model and experiment. For a thicker skin sample, the opposite adjustments were made to the material parameters.

Table 3.3: Effect on material parameter values when assumed conditions of uniaxial and biaxial stretch tests are varied. The error of fit for each assumed condition is within 1% of the error of fit of Figure 3.7.

	Modified experimental condition			
	Strain rate reduced by 90%	Strain rate reduced by 99%	Skin thickness reduced by 33%	Skin thickness increased by 33%
n_A	-	-	+38%	-21%
n_B	-	-	+51%	-11%
C_1	-90%	-99%	-73%	+96%
C_2	-	-	-36%	+5%
m	+1%	+1%	+22%	-10%

Biaxial stretching of human skin in vitro

To further test the applicability of the model to the behaviour of biological skin, the model was also fitted to the biaxial human skin experiments of Schneider (1982). The dimension of the sample was 35 x 35 x 2.5 mm. In the experiment, before any data was taken, the sample was preconditioned to allow the tissue's mechanical response to stabilise. The sample was then subjected to a constant strain in the x_2 direction and a cyclically varying strain along the x_1 direction. The results of fitting the orthotropic viscoelastic model to the experimental data are shown in Figure 3.11(a) and Figure 3.11(b) along with the results of the model developed by Shoemaker *et al.* (1986). Table 3.4 shows the error and the R^2 value of the models.

Uniaxial and biaxial stress relaxation of human skin

Wan Abas (1994) performed uniaxial and biaxial stress relaxation tests *in vivo* on human forearm skin. The test area on the forearm measured 30 x 30mm. A load of 150 N/m was applied with an extensometer in a direction along the length of the arm.

For the biaxial test the skin was restrained in the lateral direction by means of a constraining block. When the maximum load was applied, the skin was maintained at that deformation allowing the load to relax to an almost constant value. The applied strain was 0.15 for the uniaxial test and 0.11 for the biaxial test. For the purposes of modelling, it is assumed that the initial load was applied at a strain rate of 0.2 s^{-1}. The
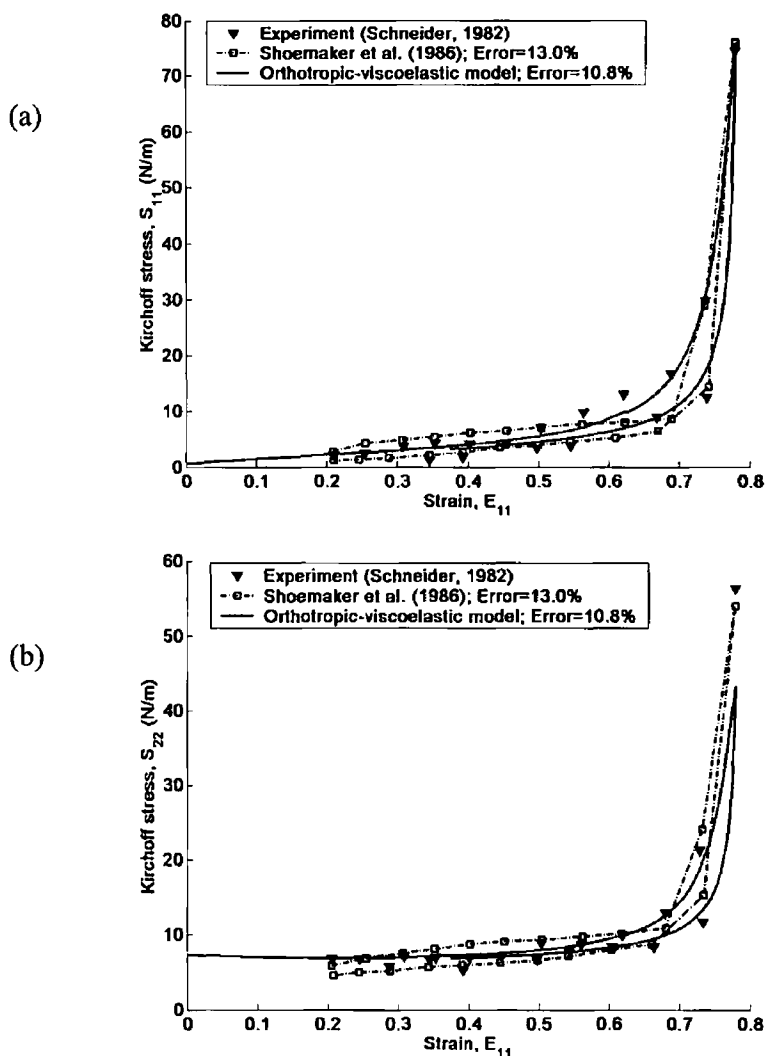
Figure 3.11: Biaxial stretching of human skin. (a) Stress response in direction of applied stretch; (b) Stress response in direction transverse to applied stretch; Orthotropic-viscoelastic model parameters: n_A= 1.727x10^{23}; n_B=4.210x10^{22}; (a_A,b_A,c_A)= (0.791,2.058,1.258); (a_B,b_B,c_B)= (1.954,1.887,0.509); B=53 kPa; C_1=0.00031428 s^{-1}(kPa)$^{-m}$; C_2=-0.385; m=0.855

Table 3.4: Error measure and R^2 values for models applied to human skin experiments of Schneider (1982).

Model	Error (%)	R^2
Orthotropic-viscoelastic	10.8	0.982
Shoemaker *et al.* (1986)	13.0	0.962

fitting of the orthotropic-viscoelastic model to the stress relaxation results are shown in Figure 3.12, along with the material parameters used.

49
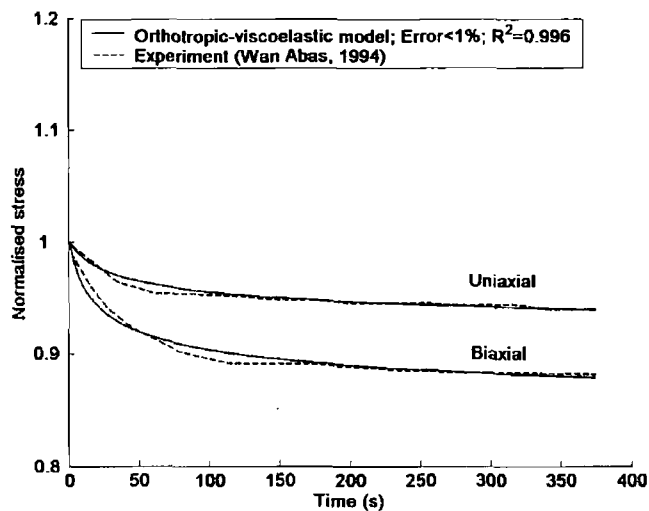
Figure 3.12: *In vivo* uniaxial and biaxial stress relaxation tests of human forearm skin. Orthotropic-viscoelastic model parameters: $n_A = 1.641 \times 10^{24}$; $n_B = 2.27 \times 10^{22}$; $(a_A, b_A, c_A) = (2.265, 1.378, 1.894)$; $(a_B, b_B, c_B) = (1.481, 1.419, 0.694)$; $B = 50$ kPa; $C_1 = 0.000034672 \ s^{-1}(kPa)^{-m}$; $C_2 = -0.921$; $m = 2.552$

Uniaxial tensile and compression tests of pig skin

Ankerson *et al.* (1999) conducted uniaxial tensile tests on skin samples taken from the abdomen of pigs. Loads were applied along directions both parallel and perpendicular to the spine to demonstrate the orthotropic characteristics of the pig skin. The strain rate for the experiments was $0.01 s^{-1}$. The experimental results are shown in Figure 3.13 along with the results of the orthotropic-viscoelastic model. Shergold *et al.* (2006) fitted the one-term Ogden strain energy model to the experimental data. Their results are also included in Figure 3.13.

Shergold *et al.* (2006) conducted compressive tests on *in vitro* pig skin samples at strain rates ranging from 0.004 to 4000 s^{-1}. The samples were 7 mm in diameter and 2.3 mm thick. Material parameters for the orthotropic-viscoelastic model were found to fit the compressive tests at strain rates of 0.04 and 40 s^{-1}. Both the model and the experimental results are shown in Figure 3.14. It is noted that Shergold *et al.* (2006) used the Ogden strain energy function to model the same compressive tests. As the Ogden function is not time-dependent, it was necessary to use different material parameters for each strain-rate.
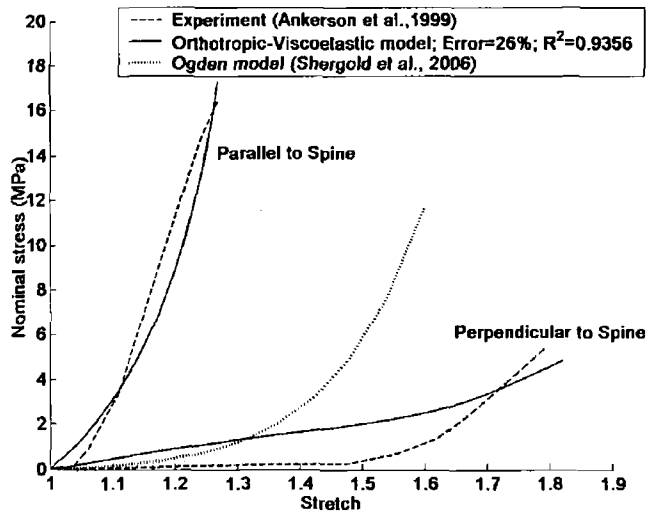
Figure 3.13: Uniaxial tensile tests of pig abdomen skin. Orthotropic-viscoelastic model parameters: $n_A=$ 5.27x10^{24}; $n_B=$1.98x10^{24}; $(a_A,b_A,c_A)=$ (1.425,0.777,1.176); $(a_B,b_B,c_B)=$ (1.425,0.777,1.176); $B=$71 kPa; $C_I=$0.0041297 s^{-1}(kPa)$^{-m}$; $C_2=$-1.0; $m=$1.461; Ogden model parameters: $\alpha=$12, $\mu=$0.4 MPa (Shergold et al., 2006)
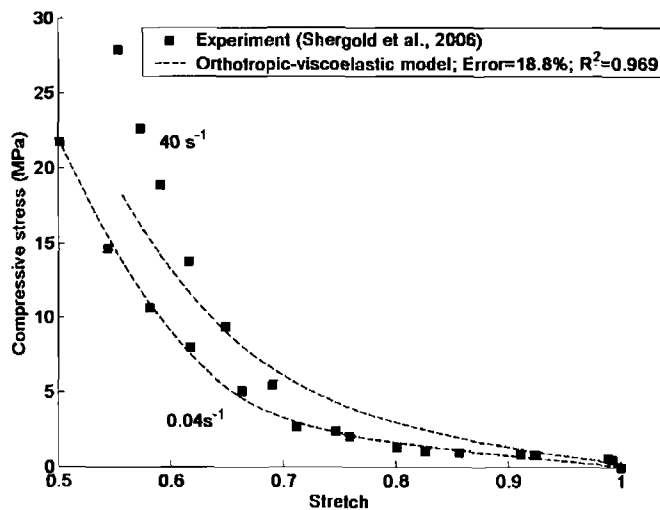
Figure 3.14: Compression of pig skin at different strain-rates; Orthotropic-viscoelastic model parameters: $n_A=$ 2.023x10^{25}; $n_B=$3.435x10^{25}; $(a_A,b_A,c_A)=$ (1.277, 0.883, 1.303); $(a_B,b_B,c_B)=$ (1.250, 0.878, 1.328); $B=$32 MPa; $C_I=$0.9779 s^{-1}(MPa)$^{-m}$; $C_2=$-1.0; $m=$1.619

Uniaxial compression tests of monkey liver at different strain rates

Bergstrom and Boyce (2001) fitted their model to experimental data from compression tests of monkey liver at different strain-rates (Miller, 2000). The orthotropic viscoelastic model was also fitted to this experimental data in order to further compare its performance with the Bergstrom and Boyce (2001) results. Figure 3.15 displays the fit of both models and Table 3.5 shows the errors and R^2 values.

51
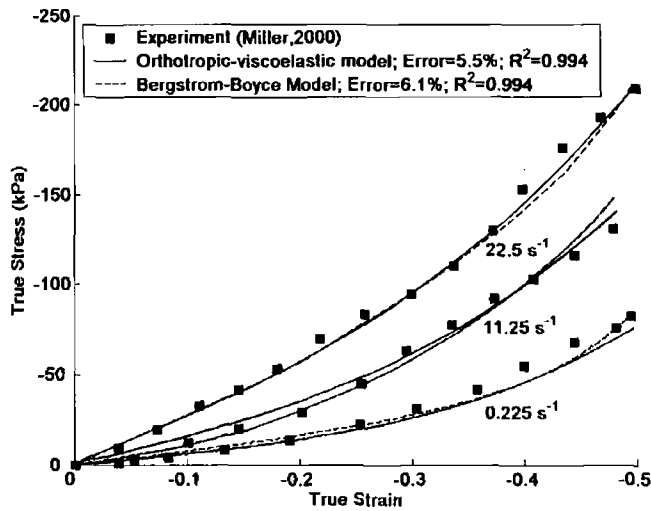
Figure 3.15: Compression of monkey liver at different strain-rates; Orthotropic-viscoelastic model parameters: $n_A=$ 1.194x10^{24}; $n_B=$4.202x10^{24}; $(a_A,b_A,c_A)=$ (1.287,1.287,1.172); $(a_B,b_B,c_B)=$ (0.958,0.960,1.585); $B=$640 kPa; $C_1=$8.036 s^{-1}(kPa)$^{-m}$; $C_2=$-0.04; $m=$0.001; Bergstrom-Boyce parameters: $\mu_A=$27.5 kPa, $\mu_B=$186 kPa, $\lambda_A^{lock} = \lambda_B^{lock} =$1.17, $C_1 = 0.39$ s^{-1}(kPa)$^{-m}$, $C_2 = $ -1, m = 0.12, $\varepsilon = 0.01$

Table 3.5: Error measure and R^2 values for models applied to monkey liver experiments of Miller (2000).

Model	Error (%)	R^2
Orthotropic-viscoelastic model	5.68	0.996
Bergstrom-Boyce	6.14	0.994

3.3.3 Implementation of constitutive model into finite element analyses

In order to study more complex boundary value problems it is necessary to incorporate the orthotropic-viscoelastic constitutive law into finite element analyses. ABAQUS Version 6.5 (ABAQUS, Inc., Providence, Rhode Island, USA) allows the implementation of user-defined materials through its user subroutine facilities (Hibbitt *et al.*, 2004). The orthotropic-viscoelastic model is implemented into ABAQUS/Explicit. Details on how the material model is implemented into the finite element package are contained in the Appendix B along with the FORTRAN code for the user subroutine in Appendix C.

52

3.4 Modelling the hypodermis

3.4.1 Hyperelastic model with linear viscoelasticity

As discussed in Section 2.3.3, the hypodermis has been shown to have a non-linear viscoelastic stress-strain response. Consider a specimen of hypodermis under a stretch, λ, which is a function of time.

The total stress in the specimen is assumed to be equal to an elastic stress, $T_e[\lambda(t)]$, due to the instantaneous tissue response decreased by a viscous component depending on the past history. From Fung (1993), the stress at any time t is given by

$$T(t) = T_e[\lambda(t)] + \int_0^t T_e[\lambda(t-\tau)] \frac{\partial g_R(\tau)}{\partial \tau} d\tau \qquad (3.50)$$

where $g_R(t)$ is the reduced relaxation function, which characterises the material's viscoelastic response.

A common approach to representing $g_R(t)$ is to define it by a Prony series expansion as follows:

$$g_R(t) = 1 - \sum_{i=1}^{N} \bar{g}_i^P \left(1 - e^{-t/\tau_i^G}\right) \qquad (3.51)$$

where $\bar{g}_i^P$ and τ_i^G are material parameters.

The elastic stress component, $T_e[\lambda(t)]$, is defined by the hyperelastic Yeoh model, whose strain energy potential is

$$W = C_{10}(I_1 - 3) + C_{20}(I_1 - 3)^2 + C_{30}(I_1 - 3)^3 +$$
$$\frac{1}{D_1}(J-1)^2 + \frac{1}{D_2}(J-1)^4 + \frac{1}{D_3}(J-1)^6 \qquad (3.52)$$

Using the relationship, $T_{ei}[\lambda] = \lambda_i \dfrac{\partial W}{\partial \lambda_i}$, the elastic stress component is given by

$$T_{ei}[\lambda] = \frac{2\lambda_i^2}{J} \left[C_{10} + 2C_{20}(I_1 - 3) + 3C_{30}(I_1 - 3)^2 \right] +$$
$$\frac{2}{D_1}(J-1) + \frac{4}{D_2}(J-1)^3 + \frac{6}{D_1}(J-1)^5 \qquad (3.53)$$

Specifying the parameters, C_{10}, C_{20}, C_{30}, D_1, D_2, D_3, $\bar{g}_i^P$ and τ_i^G, Equations 3.50, 3.51 and 3.53 can be solved to give the total stress in the hypodermis specimen.

3.4.2 Modelling the experiments

The hyperelastic, viscoelastic constitutive model for the hypodermis was fitted to experimental data obtained from unconfined compression tests of human calcaneal fat pads (Miller-Young et al., 2002).

The Yeoh model parameters, C_{10}, C_{20} and C_{30}, were found by fitting Equation 3.53 to a compression test of calcaneal fat carried out at a high strain rate of 35 s^{-1}. Figure 3.16 shows the comparison between the experimental data of Miller-Young et al. (2002) and the Yeoh model. A good fit is observed with an error of 6.22% and R^2 of 0.988.

The Prony series parameters were found by fitting Equation 3.51 to stress relaxation data of calcaneal fat. The stress-time data of Miller et al. (2002) was converted to normalised relaxation modulus-time data by dividing the stress by the strain at which the relaxation test was carried out – in this case, -0.4. The normalised relaxation modulus, $g_R(t)$, from the experiment and the fitted Prony series are shown in Figure 3.17. The error between the experimental and model data is 9.13% with an R^2 fitting of 0.9114.

Using the parameters obtained from the rapid compression and stress relaxation tests, the stress-strain response of the hypodermis model under quasi-static unconfined compression was calculated. The strain rate of the compression was 0.001s^{-1}. Figure 3.18 shows the model and experimental result. The model differs
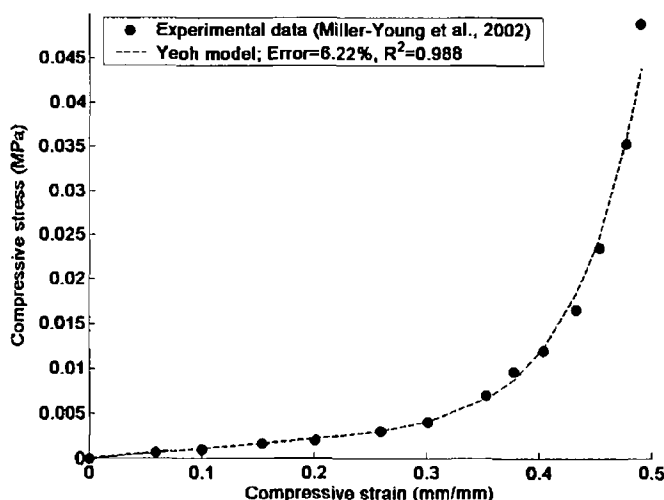
Figure 3.16: Rapid unconfined compression of human calcaneal fat-samples. Strain rate=35 s^{-1}. Yeoh model parameters: C_{10}=1.649 kPa; C_{20}=-1.136 kPa; C_{30}=-1.792 kPa
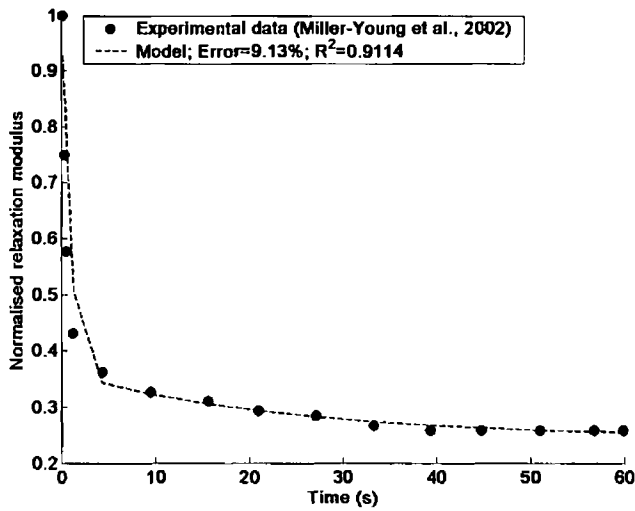
Figure 3.17: Normalised relaxation moduli from human calcaneal fat pad under 40% deformation. Prony series parameters: $\bar{g}_1^P$ =0.63928; τ_1^G =0.67772 s; $\bar{g}_2^P$ =0.11572; τ_2^G =24.024 s
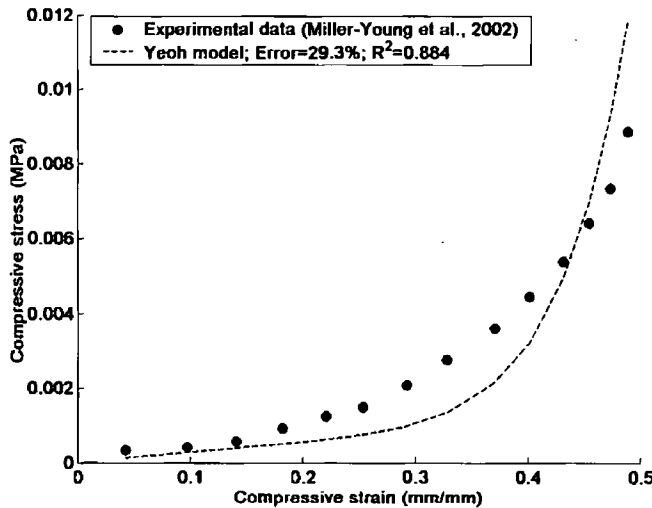
Figure 3.18: Quasi-static unconfined compression of human calcaneal fat-samples. Strain rate=0.01s^{-1}. Model parameters used are those from the rapid compression and stress relaxation tests in Figure 3.16 and Figure 3.17.

from the experiment by 29.3%. The R^2 value of the fit is 0.884.

3.4.3 Implementation of hypodermis model into finite element analyses

Most commercial finite element packages such as ABAQUS contain the Yeoh hyperelastic function and the Prony series as part of their in-built material modelling

features. Therefore, implementation of the proposed hypodermis model into finite element analyses is a trivial matter.

3.5 Multi-layer model

In Sections 3.2, 3.3 and 3.4, the constitutive models for the separate layers in the skin and hypodermis were developed. Using a commercial finite element package such as ABAQUS, each layer can be implemented into finite element analyses by either using the in-built material models or programming the material model using the user subroutine facilities.

In the finite element models, the connections between the layers needed to be specified. The stratum corneum was modelled as a shell structure and its bottom surface was connected to the top surface of the underlying layer using mesh tie constraints (Figure 3.19). This constrained all translational degrees of freedom of the nodes of the stratum corneum shell to be the same as the nodes on the top surface of the underlying layer to which they were closest. As discussed in Section 2.2.4, the epidermis is firmly attached to the dermis by the anchoring collagen fibrils. The thickness of the stratum corneum was assumed to be 20 μm. The nodes at the bottom surface of the dermis and the top surface of the hypodermis were shared. The thickness of the dermis was 1.2 mm and the thickness of the hypodermis 1.5 mm.

There were several simplifications made when developing the multi-layer model for skin. Firstly, the surface of the stratum corneum in the finite element models was assumed to be perfectly smooth in its undeformed state. As shown in Figure 2.3, this is not the case in real skin. Secondly, the interface between the epidermis and dermis
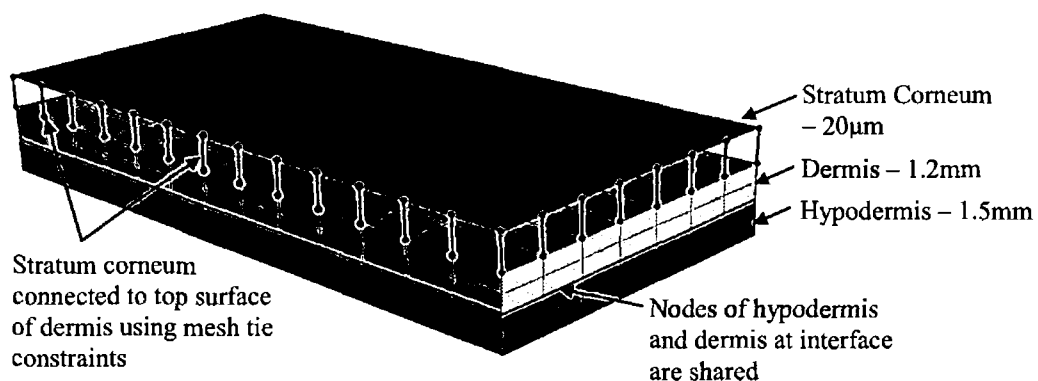
Figure 3.19: Multi-layer model of skin

was assumed to be flat. As shown in Figure 2.4, the interface undulates, which increases the surface contact area between the two layers and thus enhances the firmness of attachment. The interface between the dermis and hypodermis was also assumed to be flat. In reality, there is no clear boundary between the lower dermis and the hypodermis. Descending through the lower dermis, the density of collagen fibres starts to decrease and the amount of adipose tissue increases. One layer gradually changes into the other (Cohen and Wood, 2000). Despite these simplifications, the model does realistically represent the wrinkling behaviour of skin as will be seen in the next chapter.

3.6 Summary

Constitutive models have been developed for the stratum corneum, epidermis, dermis and hypodermis.

The stratum corneum was modelled using the neo-Hookean strain energy function. The dermis was represented by an orthotropic-viscoelastic model and was tested widely against experimental data reported in the literature. The model for the hypodermis consisted of the hyperelastic Yeoh strain energy function and a two-term Prony series to simulate the viscoelastic characteristics of the hypodermis.

The individual models representing each layer in the skin and hypodermis were then combined in a finite element model to form a multi-layer model of skin. More complex deformations of skin can now be analysed to see the effects of the different layers.

Chapter 4

Simulating the wrinkling of forearm skin

4.1 Introduction

This chapter details an experimental procedure that was developed to generate and measure wrinkles on the surface of volar forearms of volunteers. Finite element models were developed of the experiments and the results of both were compared. The influence of the pre-stress in the skin and the properties of each layer in the skin were also investigated.

4.2 Material and methods

4.2.1 Laboratory experiment

Measurement system

The system used to measure the wrinkle profile on the skin surface was a modification of a system originally developed to measure the blade profile of surgical osteotomes (Price, 2005). It consisted of a charged coupled device (CCD) laser displacement sensor (LK-2000 Series, Keyence, Osaka, Japan) mounted on a micro-translation stage (M-111DG, Physik Instrumente Gmbh, Karlsruhe, Germany) (Figure 4.1). The laser sensor was controlled by a laser controller unit (LK-2001, Keyence, Osaka, Japan). The laser control unit was connected to a laptop computer (Dell Latitude D800 Pentium 1.6 GHz) via a data acquisition card (NI PCI-6036E, National Instruments, Austin, USA). The micro-translation stage was controlled by a DC-motor controller (Mercury II C-862, Physik Instrumente Gmbh, Karlsruhe, Germany). The controller was connected to the laptop computer through the series port. A program developed in Labview Version 7.1 (National Instruments, Austin, USA) allowed the
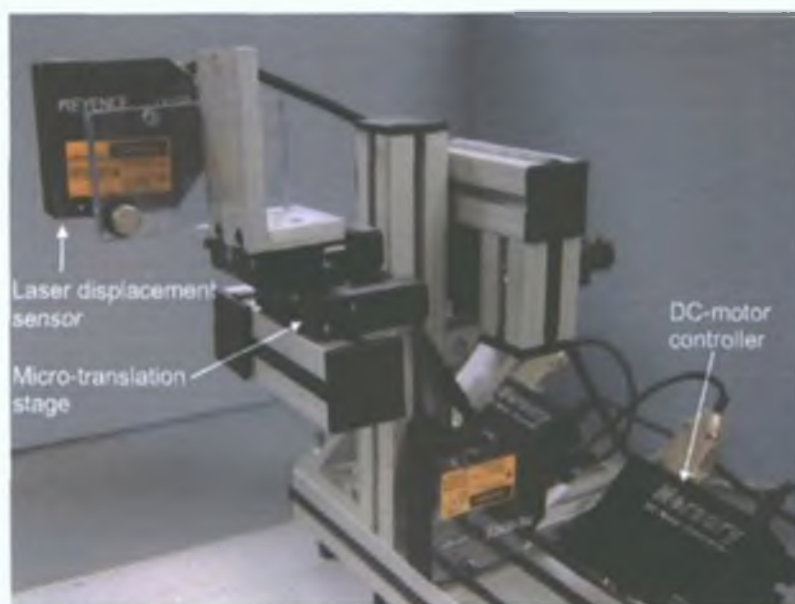
Figure 4.1: Laser profilometer machine with the laser displacement sensor mounted on the micro-translation stage, which is controlled by the DC-motor controller (Price, 2005). A laser sensor controller (not shown) controls the laser sensor. Commands to both controllers are sent from a Labview program on a laptop connected to the machine.

user to control the motion of the micro-translation stage and store the acquired data from it and the laser sensor in text files.

A series of slip gauges were used to evaluate the measurement error of the system. A parallel was placed underneath the laser sensor. The Labview program was initiated and the laser sensor scanned 10 mm along the length of the parallel (Figure 4.2). Data containing a three-dimensional coordinate of a point on the surface of the specimen was acquired every 100 µm.

Adjustments were made to the parallel ensuring it was horizontal and the laser sensor controller was adjusted so that the height reading for the surface of the parallel was zero. A 1.05 and a 1.0 mm slip gauge were placed side by side on the parallel and a 5 mm scan was performed, which included the step from one to the other. The data from the scan was analysed and the height of the step calculated. Minor adjustments to the laser sensor controller were made to bring the measured step height closer to the actual step height. Once the measurement error was satisfactorily low (about 10%), ten further scans of 5 mm length were made of the step. The step height and error was calculated for each scan. Ten scans were also made of a 0.1 and 1.0 mm step. The average, maximum and minimum errors of all three step-sizes are shown in Table 4.1.
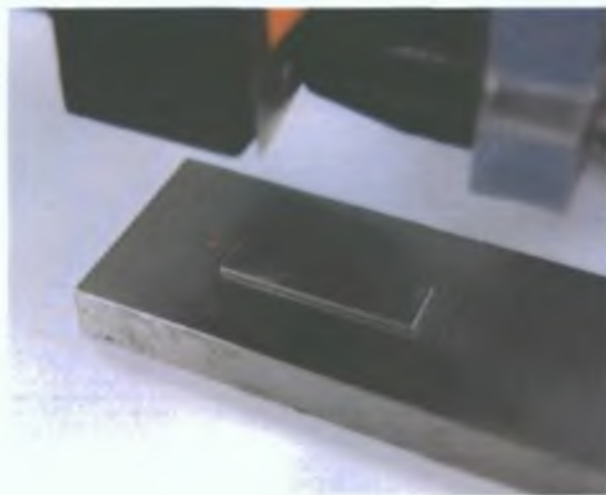
Figure 4.2. Evaluating measurement error of system using slip gauges.

It is noted that as the step size gets larger the measurement error gets smaller, being less than 0.5% on average for the 1.0 mm step.

Further evaluation of the measurement error of the system was carried out scanning a number of surfaces, all of which have a known surface roughness R_a and peak-to-valley amplitude R_v. R_a is defined as

$$R_a = 1/L \int_0^L |r(x)| dx \qquad (4.1)$$

where L is the scan length and $r(x)$ is the profile height at a point x.

The surfaces were part of a Rugotest roughness comparison specimen (Microtron Ltd., London, UK) used to test the quality of surfaces produced by different machining methods such as turning, grinding and planing. The Rugotest 101 specimen for testing planed surfaces was used in this test. The laser sensor scanned a line 10 mm in length in a direction perpendicular to the grooves (Figure 4.3). The roughness and peak-to-valley amplitudes of the surfaces measured along with the errors are shown in Table 4.2. As in the case of the slip gauges, the error decreases as the scale

Table 4.1: Error of laser profilometer system when measuring thickness of slip gauges. Each slip gauge was measured 10 times.

Step size (mm)	Average Error (%)	Max. Error (%)	Min. Error (%)
0.05	+7.85	+14.14	+4.37
0.1	+6.51	+8.95	+4.68
1	-0.48	-0.60	-0.33

Figure 4.3: Evaluating measurement error of system using Rugotest surface comparators

of the features being measured increase in size.

It will be shown later in the results that the maximum range of the wrinkles varied from about 0.2 mm at zero tab displacement to 1 mm at a tab displacement of 20 mm. Referring to Table 4.1 and Table 4.2 with these ranges, the measurement error of the maximum range varies from +10% for small tab displacements down to 0.5% for larger tab displacements. It will also be shown later that the average roughness at zero tab displacement was about 0.02 mm. From Table 4.2, the maximum measurement error for an average roughness of this order was -1.6%. It was assumed that for larger tab displacements, the measurement error for the average roughness would be less.

It was concluded that the measurement error of the laser profilometer was acceptable for measuring the wrinkles on the forearms of the volunteers.

Measuring wrinkles In vivo

The experimental configuration for measuring the wrinkles is shown in Figure 4.4 with a schematic of the configuration shown in Figure 4.5. Eight volunteers were used in the study. The arm of a volunteer was restrained in a support such that the volar

Table 4.2: Error of laser profilometer system as determined by scanning Rugotest 101 roughness comparison specimens

Surface Number	Specified R_a (µm)	Measured R_a (µm)	R_a error (%)	Specified R_v (µm)	Measured R_v (µm)	R_v error (%)
18	12.5	13.3	+6.4	50	59.9	+19.8
19	25	24.8	-1.6	100	109.9	+9.9
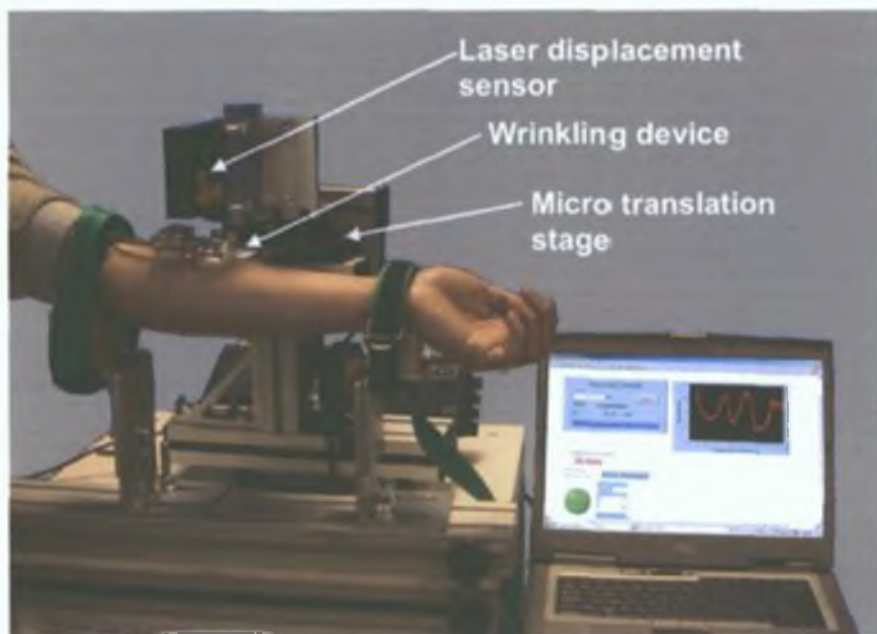
Figure 4.4: Experimental configuration
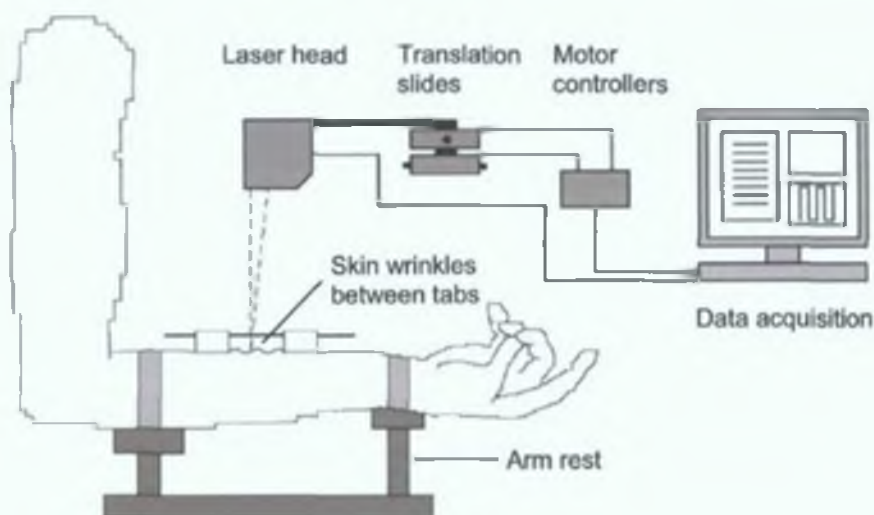
Figure 4.5: Schematic of experimental configuration

forearm faced upwards towards the laser head.

The surface of the skin was compressed in a controlled manner by means of a wrinkling device (Figure 4.6). It consisted of two tabs measuring 40 by 20 mm, which can be displaced towards each other in fixed measurements along two guide bars. The bottom surface of each tab was curved to improve the circumferential contact with the skin of forearm. The tabs were attached to the skin using double-sided tape and in some cases cyanoacrylate adhesive. The initial separation distance between the tabs
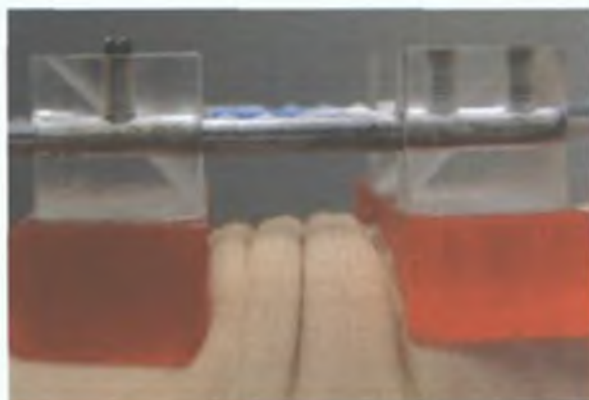
Figure 4.6: Tabs attached to skin of forearm and displaced towards each other, wrinkling the skin in between

was 45 mm. The distance was reduced to 20 mm in steps of 5 mm. At each step, the laser scanned a centre-line perpendicular to the wrinkles between 10 and 15 mm in length. The centre-line was chosen because the wrinkles were at their largest and most uniform here.

The experimental test was performed five times on one of the volunteers and once on all the other seven volunteers. The repeated tests on the volunteer were carried out to investigate the intra-person variation of the measured wrinkle profiles.

Wrinkle parameters

Two measurements were calculated from the wrinkle profile and are shown in Figure 4.7. The maximum range R_{max} of the wrinkles was defined as the height difference between the highest peak and deepest trough over the scanned length. The average roughness R_a of the wrinkles over the evaluation length was defined in Equation 4.1. In their study of skin wrinkles, Akazaki *et al.* (2002) used the maximum range to characterise wrinkle depth and average roughness to characterise wrinkle width.

Another parameter that was considered to characterise the wrinkles was the mean spacing S_m (ISO 4287 1997 cited in Leach and Harris (2002)). It was defined as the mean value of the profile element width within a sampling length

$$S_m = 1/N \sum_{i=1}^{N} S_i \tag{4.2}$$

where N was the number of wrinkles in the scanned length and S_i was the width of an individual profile or wrinkle. S_i was measured from the point at which the profile first crossed above the mean line to the point at which the profile crossed above the mean

63
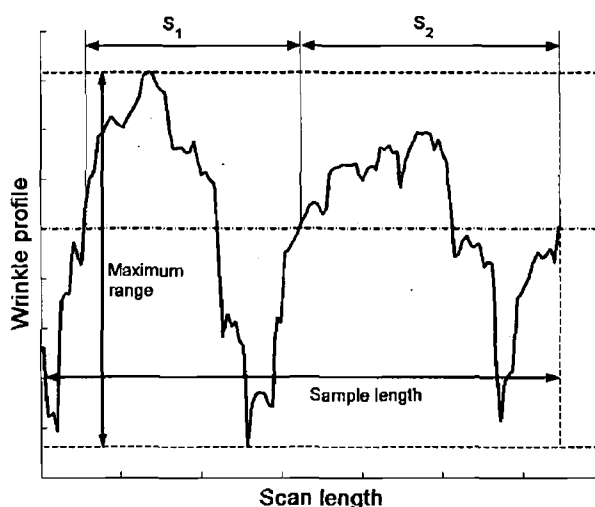
Figure 4.7: Typical wrinkle profile: the maximum range and average roughness of the wrinkles were measured. The average roughness was defined as the shaded area divided by the sample length. The spacing of the profile peaks is also shown.

line again as shown in Figure 4.7. A profile peak or valley was considered real only if its height or depth exceeded 10% of the maximum range and its width exceeded 1% of the sampling length. According to Leach and Harris (2002) an algorithm for calculating the value of a parameter such as the mean spacing should be stable. This means that small changes to the wrinkle profile data or threshold values should result in only small changes to the mean spacing. This stability was not observed in this study when calculating the mean spacing of the wrinkles in the experiments and models for larger tab displacements. The formula for mean spacing was developed for quantifying the topography of machined surfaces. In a sample length of a machined surface, there would be on the order of one hundred profile elements that would be used in the calculation of the mean spacing. In the present study, at large tab displacements, there were only about two or three full wrinkle profile elements in the sample length. Small changes in the data or threshold values introduced or eliminated profile elements and because of the small number of wrinkles N, this had a large effect on the mean spacing. While the mean spacing may be suitable for quantifying the topography of the undeformed surface of skin (Leveque, 1999), it was decided in this study that the mean spacing was not suitable for characterising the width of the wrinkles at large tab displacements.

Wrinkle replicas

For some volunteers, instead of measuring the wrinkle profile directly from the skin, replicas of the wrinkles at each tab displacement were produced using a low-viscosity dental impression silicone material (Thixoflex® M and Indurent Gel, Zhermack, Italy). The impression material and hardener were mixed and lightly spread over the skin between the displaced tabs (Figure 4.8). The mixture hardened within a couple of minutes and was then peeled away from the skin. For larger tab-displacements and, hence deeper wrinkles, it was found that applying the impression material to the skin before displacing the tabs resulted in better penetration of the material to the bottom of the wrinkles. It was investigated whether the replicas were a good representation of the actual wrinkles. For one volunteer, the wrinkles were measured directly from the skin at each tab displacement in the usual manner. With the tabs still in place on the forearm, replicas were also produced at each tab displacement and their profiles measured. The maximum range and average roughness of the replica wrinkles and the directly-measured wrinkles were then compared.

Producing replicas of the wrinkles had several advantages. Wrinkle profiles could be obtained from volunteers who were not in the vicinity of the laser profilometer. The replicas could be stored so that further measurements could be made in the future if needed. Also in future studies, replicas could be made of wrinkled areas that would be difficult to measure directly such as the facial area.

4.2.2 Finite Element Models

ABAQUS/Explicit Version 6.5 was used to develop a finite element model of the experiment, which is shown in Figure 4.9. The problem was assumed to be symmetrical and so one-quarter of a forearm skin area measuring 67.5 mm by 10 mm
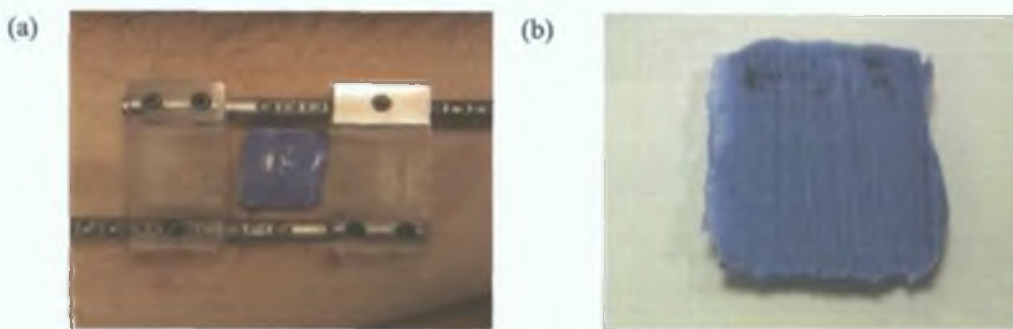
Figure 4.8: Producing a replica of the wrinkles: (a) Silicone dental impression material applied between displaced tabs; (b) replica of wrinkles
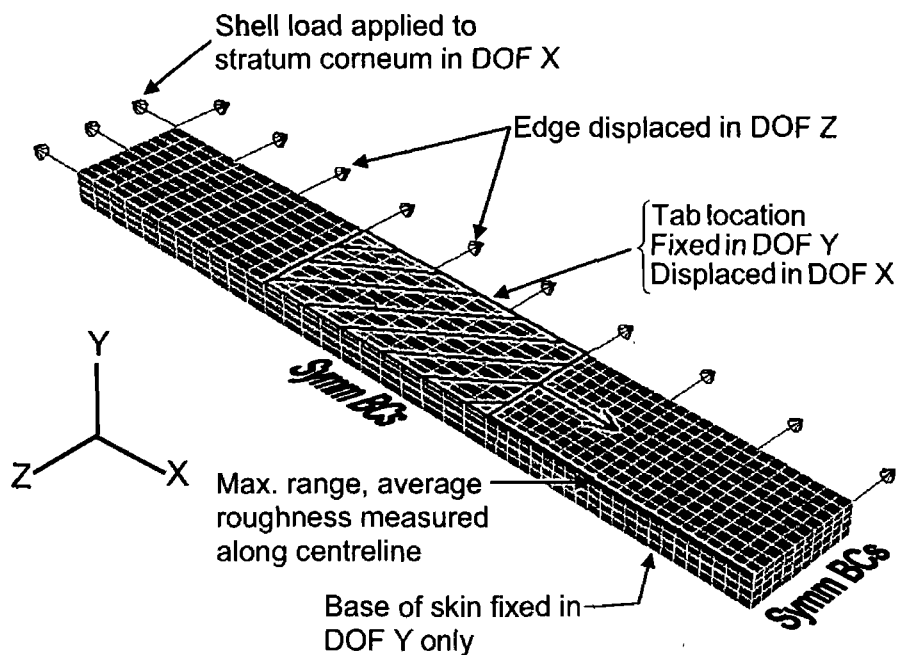
Figure 4.9: Finite element model. Note that the actual mesh density used in the analyses was much higher than displayed here. For the three-layer model, there were 58592 nodes and 47460 elements

was modelled. For one of the analyses, a model measuring 67.5 mm by 20 mm was run to quantify the effect of the boundary conditions along the long edge of the model on the results. The base of the model was fixed in the global Y-direction. The forearm was assumed to be perfectly flat. Four different models of the skin were developed to investigate the effects of the layers on the wrinkling of the skin.

Single-layer skin model

The single-layer model assumed the skin to consist of one homogeneous layer and the hypodermis was ignored. The skin was represented by the orthotropic-viscoelastic model developed in Section 3.3. The thickness of the skin was assumed to be 1.2mm, which is within the range of forearm skin thickness reported in the literature (Reihsner *et al.*, 1995; Lee and Hwang, 2002). The material parameters used were the same as those used to simulate the uniaxial and biaxial stretch tests of rabbit skin (Lanir and Fung, 1974) and are shown in Figure 3.7.

Two-layer model consisting of the stratum corneum and dermis

This two-layer model consisted of the outermost stratum corneum and an underlying layer representing the dermis. The living epidermis and hypodermis were

ignored. The thickness of the stratum corneum was assumed to be 20 μm (Batisse *et al.*, 2002; Wu *et al.*, 2006). This layer was modelled using the neo-Hookean hyperelastic equation described in Section 3.2.1. The stratum corneum was assumed to have a relative humidity of 96%. The material parameters used were estimated from Table 3.1 using linear interpolation – C_l was 4 MPa and D_l was 0.01013 MPa. The dermis was represented by the same model and material parameters as the single-layer model. It was also assumed to be 1.2 mm thick.

Two-layer model consisting of the dermis and hypodermis

The dermis was represented by the same model and material parameters as the single-layer model. It was also assumed to be 1.2 mm thick. The bottom layer in the model consisted of the hypodermis. This was modelled using the Yeoh hyperelastic function along with a Prony series to capture quasi-linear viscoelasticity as described in Section 3.4.1. The thickness of the hypodermis was assumed to be 1.5 mm. The material parameters used were the same as those in Figure 3.14 and Figure 3.15.

Three-layer model consisting of the stratum corneum, dermis and hypodermis

In the three-layer model, the top two layers, consisting of the stratum corneum the dermis, were represented using the same material models and parameters as for the two-layer model. The thicknesses of the layers were also assumed to be 20 μm for the stratum corneum and 1.2 mm for the dermis.

The bottom layer in the model consisted of the hypodermis and was represented by the same material model as the two-layer model. It was assumed to be 1.5 mm thick.

To investigate the effect of the thickness of the layers on the wrinkle formation, another three-layer model was built where the hypodermis had the same material properties as the dermis. Therefore, it was equivalent to the two-layer model described above except the dermis is now 2.7 mm thick instead of 1.2 mm thick. This analysis will show the effect of the layer thickness and the hypodermis mechanical properties on the size of the wrinkles.

Finite element mesh

The stratum corneum layer was meshed using four-noded reduced integration shell elements (S4R) with enhanced hourglass control. The layer was connected to the

underlying layer using mesh tie constraints. The dermis and hypodermis were meshed using eight-noded reduced integration linear brick elements (C3D8R) with enhanced hourglass control and distortion control was also enabled.

For all the layers, there were 200 elements along the length between the tab and the end with the symmetrical boundary condition. There were 15 elements across the width of the model. For the dermis, there were 8 elements across its thickness, while there were 5 across the thickness of the hypodermis. The mesh density was reduced in areas of the model where wrinkling would not occur. In total, there were 3632 nodes and 3390 elements in the stratum corneum; 32976 nodes and 27120 elements in the dermis; and, in the three-layer model, 21984 nodes and 16950 elements in the hypodermis.

A mesh sensitivity analysis was carried out to ensure that the mesh density was adequate for the simulations. The chosen mesh was such that an increase in the density of 50% resulted in a change to the predicted maximum range and average roughness of less than 4%. The results were converging. Ideally, the chosen mesh would be such that doubling the mesh density would change the results by less than 1%. However, using the available computational resources, it was estimated that one analysis with such a mesh would take several weeks to run. The maximum range and average roughness of the wrinkles decreased slightly as the mesh density increased. It will be seen later that the maximum range and average roughness of the predicted wrinkles by the finite element analysis was larger than that measured in the experiments. Using a higher mesh density, therefore, would reduce the error between the model and experiment. The mesh density is of less importance when comparing the results of different finite element analyses of the same mesh density.

Mass scaling

In ABAQUS/Explicit, the state of the model at time t is stepped forward an increment Δt. The central difference operator used to step the analysis forward in time is only conditionally stable. The maximum increment the model can be advanced without becoming numerically unstable is known as the stability limit and is dependent on the characteristic element length, the stiffness and density of the material. As a result of the very fine mesh, the high stiffness of the stratum corneum and the high non-linearity of the dermis and hypodermis, the maximum time step Abaqus/Explicit could advance the solution in the current study was on the order of

1×10^{-8} s resulting in very long analyses. A technique to reduce solution times, known as mass scaling, was employed. The analyses were assumed to be quasi-static in nature. Mass-scaling involved increasing the stability limit by artificially increasing the material density. For the analyses run in this study the density of the stratum corneum was increased by a factor of 100000 and the density of the dermis and hypodermis was increased by a factor of 1000 in order to achieve favourable stability limits. To ensure the mass scaling was not having a dynamic inertial effect on the results it was checked that the kinetic energy of the system did not exceed 5% of the total energy over most of each analysis. This was recommended in the ABAQUS manual (Hibbitt *et al.*, 2004).

Analysis procedure

The first step in the analysis applied a stress to the skin smoothly. A shell load was applied to the edge of the stratum corneum in the X-direction as shown in Figure 4.9. The nodes of the dermis and hypodermis at the same edge were constrained to move in the X-direction with the adjacent stratum corneum nodes as shown in Figure 4.10. This was achieved using the *EQUATION keyword. Due to modelling difficulties, it was not possible to place a load boundary condition in the Z-direction along the length of the model. This problem is discussed further in Appendix E. Instead, a displacement boundary condition was specified that moved the side smoothly in the

Each row of nodes is constrained in X-direction with the row of stratum corneum nodes on the edge
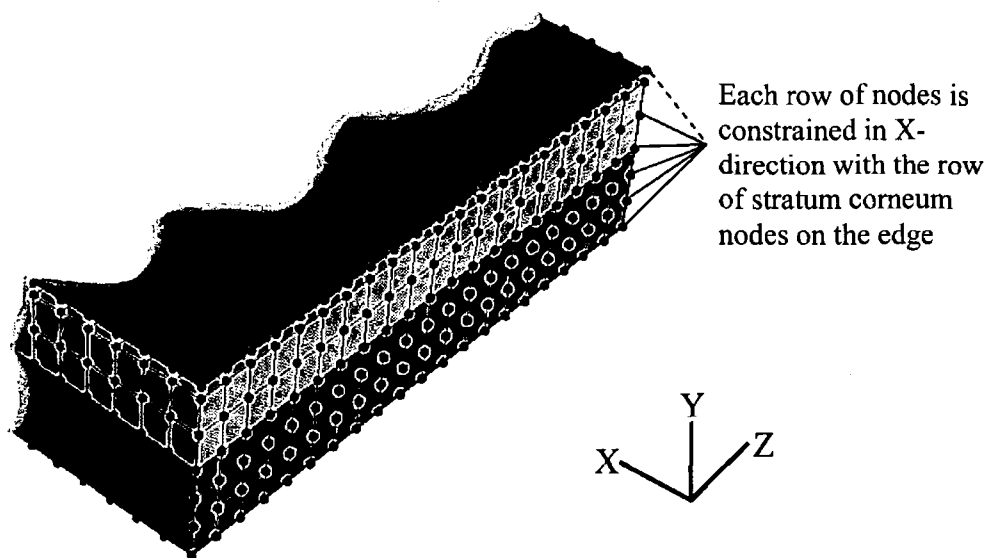
Figure 4.10: The end nodes of the dermis and hypodermis are constrained with the nodes of the stratum corneum using *EQUATION keyword in ABAQUS.

Z-direction as shown in Figure 4.9. The load and displacement applied to the edge of the stratum corneum were such that there was a 2 kPa stress in the X and Z-directions in the dermis at the end of the first step. Actual values of pre-stress of skin in the forearm region were not available in the literature. For this reason, further analyses were run with pre-stresses of 1 kPa and 5 kPa in the dermis. It should be noted that for all the analyses, the models were developed so that the length of skin between the tab and the symmetrical boundary condition was 22.5 mm at the end of the first step. This corresponds to the experiment where the two tabs were initially separated by 45 mm.

The second analysis step simulated the in-plane compression of the skin by the displacement of the attached tabs. The nodes of the top layer in the hatched area in Figure 4.9 were fixed in the global Y-direction. This area represented the location where a tab was attached to the skin surface. The nodes were then displaced in the X-direction 12.5 mm over 15 seconds, simulating the displacement of the tab. The maximum range and average roughness of the wrinkles that formed were measured along the centre-line of the model as indicated in Figure 4.9.

The full analysis took about two days to run on a 1.6 GHz Centrino PC.

Parameter study

To investigate the influence of the properties of each layer of the skin model, a parameter study was carried out. Firstly, the level of hydration of the stratum corneum layer was decreased. The adjusted material parameters of the neo-Hookean model are shown in Table 4.3. The relative humidities for these sets of parameter were estimated from Table 3.1 using linear interpolation. The properties of the other layers in the skin model were unchanged. The pre-stress in the skin was 2 kPa in the X and Z-directions.

The density of the collagen fibres in the dermis layer was also altered to see the influence it had on the wrinkle formation. Two analyses were run – one where the values n_A and n_B representing the fibre density were increased by 25% and the other where n_A and n_B were reduced by 25%. The other layers in the skin model remained unchanged and the pre-stress was 2 kPa in the X and Z directions.

Table 4.3: Material parameters used for strata cornea of different relative humidities (RH)

RH (%)	C_{10} (MPa)	D_1 (MPa)
92	12	0.00338
85	24	0.00169

A number of analyses were run to investigate the influence of the orthotropic characteristics of skin on the behaviour of the wrinkles. In one analysis, the material parameters (a_A, b_A, c_A) and (a_B, b_B, c_B) were rearranged so that the Langer's lines in the model were rotated 90° to lie in the X-direction. The pre-stress in the model was 2 kPa in the X and Z-directions. The maximum range and average roughness of the wrinkles predicted by this analysis were compared with the 2 kPa pre-stress case with the Langer's lines lying in the Z-direction.

Further analyses were run where there was an unequal pre-stress in the X and Z-directions. The pre-stress was 4 kPa in the direction of the Langer's lines and 2 kPa perpendicular to the Langer's lines. Two analyses were run – one where the Langer's lines lay in the Z-direction and the other where the lines lay in the X-direction.

4.3 Results

4.3.1 Wrinkle replica and direct measurements

The wrinkle profiles measured directly off the skin (direct measurements) and the wrinkle profiles measured from the replicas (indirect measurements) agreed closely. The maximum range of the direct and indirect profiles of the one volunteer differed by 14.7% over the full range of tab displacements (Figure 4.11(a)). The largest difference in maximum range occurred when the tabs were displaced 25 mm. This would suggest that the silicone replica material did not penetrate down to the base of the deepest wrinkles. For smaller tab displacements, the direct and indirect maximum ranges from the one volunteer were almost identical with an average difference of 7.2% up to tab displacements of 20 mm. The average roughness measured directly and indirectly differed by 4.8% (Figure 4.11(b)). Both profiles followed a similar trend with an initial slight increase in the roughness of the wrinkles and then a more rapid increase as the tabs were displaced further towards each other.

As a result of the close agreement between the laser measurements directly from the skin and the measurements indirectly from the replicas, it was decided that using the replica material to obtain wrinkle profiles from volunteers was a useful and suitable method. Wrinkle replicas were produced in cases where the volunteer was not in the vicinity of the laser profilometer measurement system. However, it was decided to disregard experimental measurements at tab displacements of 25 mm because of the apparent poor penetration of the silicone material at this point.
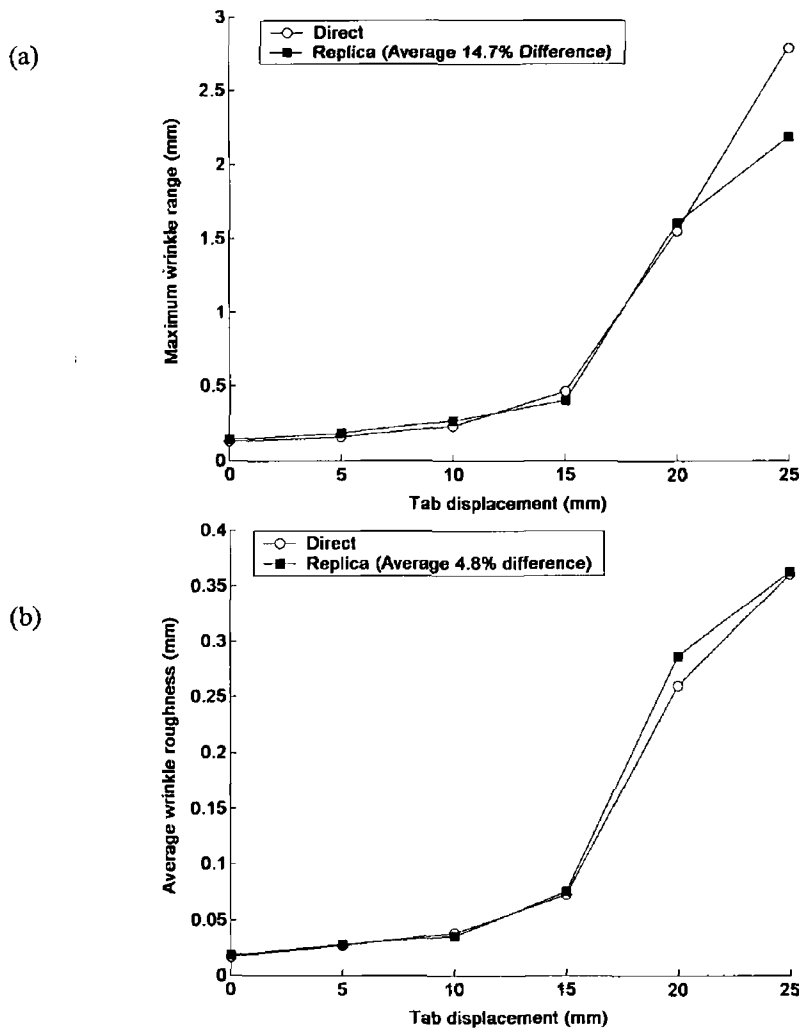
Figure 4.11: Comparison of (a) the maximum range and (b) average roughness of the wrinkles measured by laser directly from the skin of one forearm and from the silicone replica of the same forearm.

4.3.2 Experimental results

The maximum range and average roughness of the wrinkles of eight volunteers were averaged and are shown in Figure 4.12(a) and Figure 4.12(b). The maximum range increased gradually from about 0.15 mm when the tabs were not displaced to 0.35 mm when the tabs were displaced 15 mm towards each other. Thereafter, there was a greater rate of increase in the wrinkle size with an average maximum range of about 1.3 mm when the tabs were displaced 25 mm. The average roughness increased slightly from 0.025 mm at zero tab displacement to 0.035 mm at 10 mm tab displacement. For greater displacements, there was a greater rate of increase in the roughness with a value of almost 0.1 mm at 20 mm tab displacement.

72
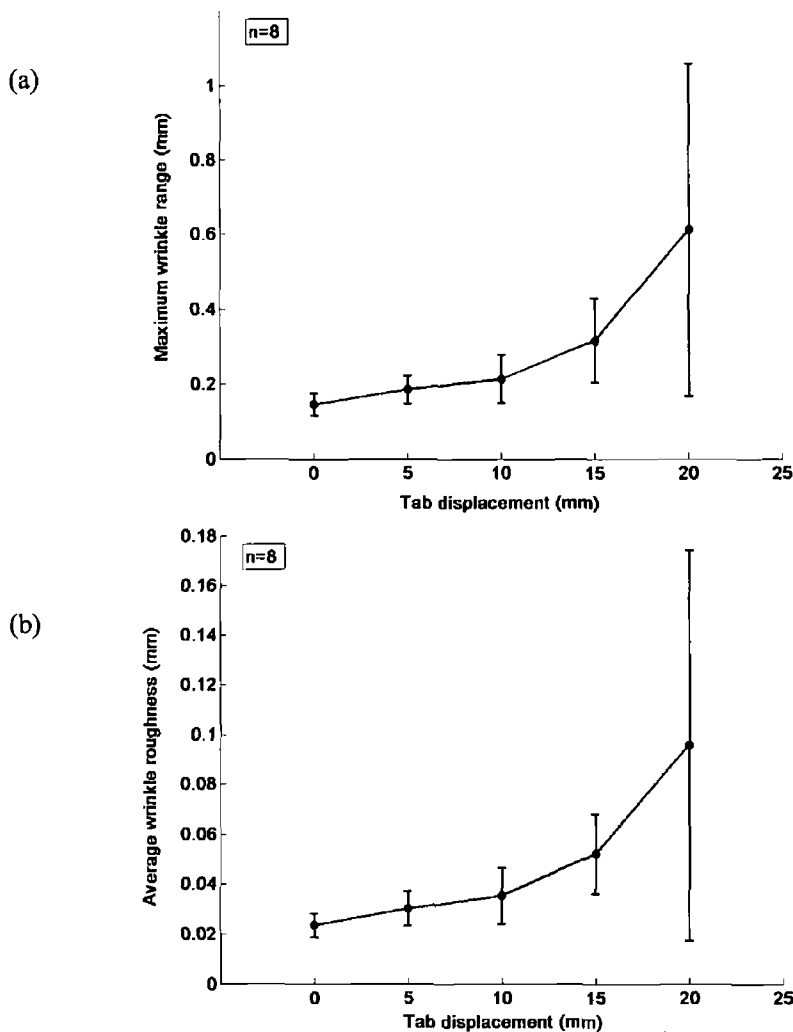
Figure 4.12: Averaged wrinkle profile results with standard deviations from eight volunteers: (a) Maximum range; (b) Average roughness

As mentioned already, the rate of change of both wrinkle parameters increased with larger tab displacements. At small tab displacements, the maximum range and average roughness were due to the wrinkling of the thin epidermis and stratum corneum layers. As the tabs displaced further, it is probable to assume that the thicker dermis and hypodermis layers started to wrinkle resulting in a greater rate of increase of the maximum range and average roughness.

Figure 4.13 shows the averaged results along with the standard deviations from the five repeat tests on the one volunteer. The intra-person variation was significantly less than the inter-person variation.

Table 4.4 compares the maximum range and average roughness at zero tab displacement with results from studies of human skin surfaces in the literature. The

(a)

(b)
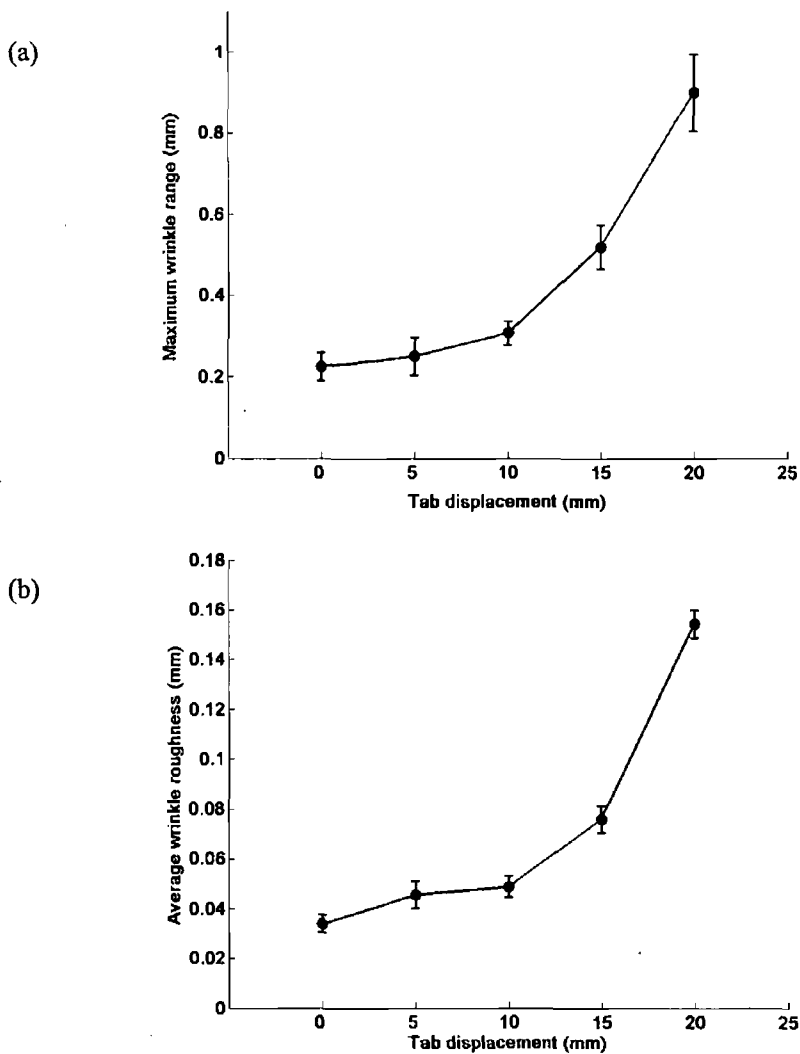
Figure 4.13: The mean and standard deviation of (a) the maximum range and (b) average roughness of the wrinkles from five repeated tests on one volunteer.

Table 4.4: Comparing the maximum range and average roughness of the volar forearm skin surface at zero tab displacement with other studies of human skin surfaces in the literature.

	Anatomical region	Maximum range (mm)	Average roughness (mm)
Present study	Volar forearm	0.15	0.025
Akazaki et al. (2002)	Eye corners	0.5 – 1.75	0.075 – 0.3
Jacobi et al. (2004)	Flexor forearm	0.2 – 0.3	0.03
Pierard et al. (2003)	Facial region	0.025 – 0.06	0.008 – 0.017
Ferguson and Barbenel (1981)	Volar forearm	0.07	0.014

74

maximum range and average roughness measured in the present study lay between the maximum ranges and average roughnesses of forearm skin measured by Ferguson and Barbenel (1981) and Jacobi *et al.* (2004).

4.3.3   Finite element results

Figure 4.14 shows the wrinkles formed on the volar forearm of one volunteer and
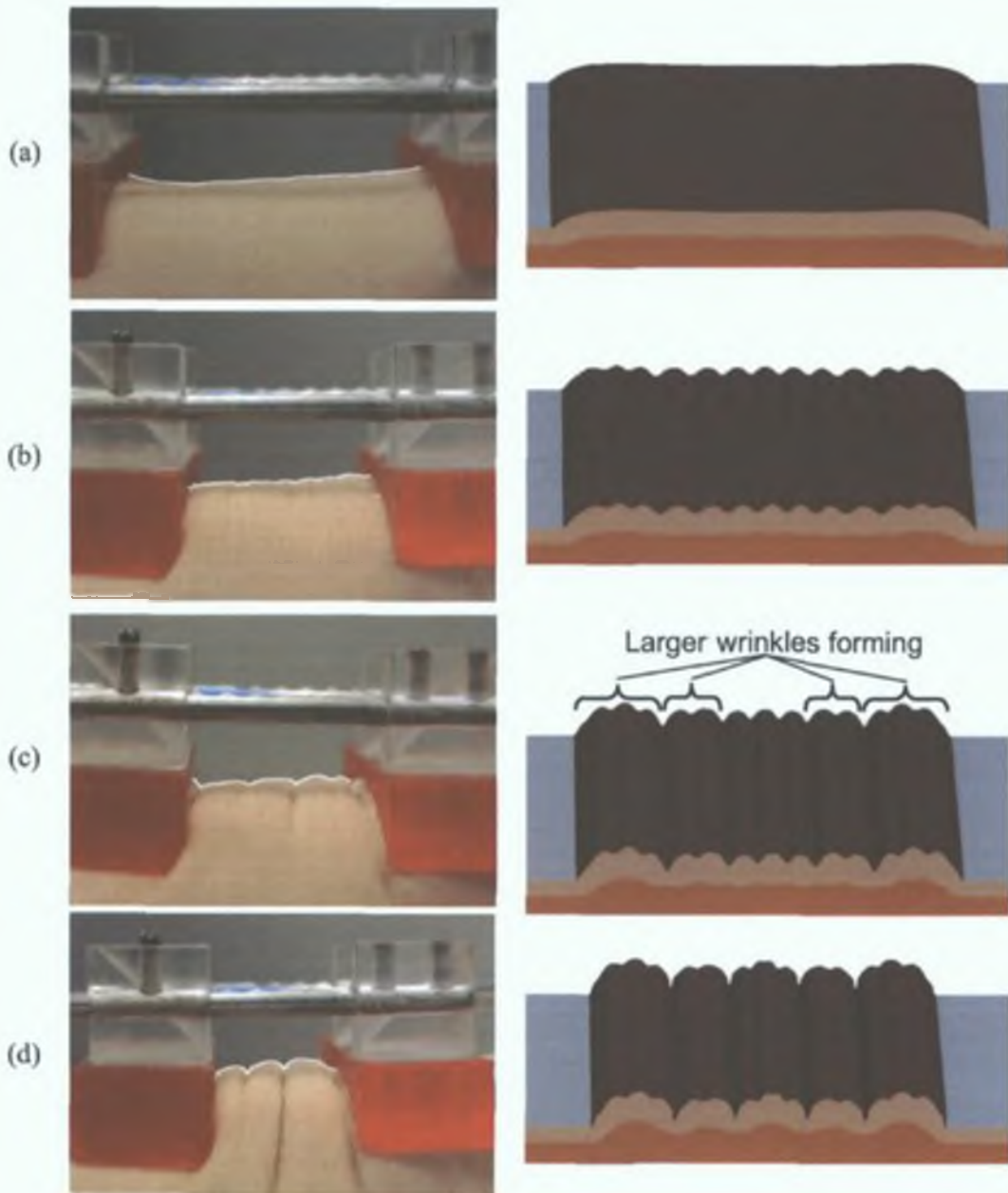
Figure 4.14: Visual comparison between the *in vivo* experiment and finite element model at different tab displacements; (a) Flat skin; (b) Small wrinkles appear; (c) Larger wrinkles begin to appear; (d) Large wrinkles dominate. The finite element results are mirrored about the axes of symmetry. Therefore, the wrinkles on the right hand sides of the finite element images are a mirror image of those on the left hand sides.

the finite element model at various tab displacements. Initially, there were no wrinkles in both the experiment and model (Figure 4.14(a)). As the tabs were displaced further, small wrinkles were visible in the experiment, while small wrinkles also formed in the model (Figure 4.14(b)). In Figure 4.14(c), larger wrinkles began to form in both the experiment and the model. At greater tab displacements, the large wrinkles were fully formed. In the model, the large macro-wrinkles dominated over the initial smaller micro-wrinkles.

Figure 4.15 shows the maximum range and average roughness of the wrinkles predicted by models with different pre-stresses. As the pre-stress in the skin model

Figure 4.15: Comparing maximum range and average roughness of wrinkles predicted by the three-layer model with different pre-stresses.

increased, the tab displacement required to create the first wrinkling increased. Increasing the pre-stress decreased both the maximum range and average roughness of the wrinkles for any tab displacement.

The maximum ranges of the wrinkles formed in the three-layer model under a pre-stress of 2 kPa are shown with the experimental results in Figure 4.16(a). The wrinkles did not appear until the tabs were displaced by over 15 mm. Similar to the experiment, the slope of the curve increased with increasing tab displacements. The maximum range predicted by the model fell within the range of the measurements from the experiments. Linearly interpolating the experimental results between the tab

Figure 4.16: Comparing maximum range and average roughness of wrinkles predicted by the two and three layer models with the experimental results. The pre-stress in both skin models was 2 kPa. The experimental data is the same as the data shown in Figure 4.12.

displacements of 15 and 20 mm, the wrinkle ranges predicted by the model differed from the average ranges measured in experiment by 31%.

The average roughness of the wrinkles formed by the same model is shown with the experimental results in Figure 4.16(b). After the wrinkles first formed at a tab displacement of about 15 mm, the average roughness of the wrinkles increased steadily up to almost 0.16 mm at a tab displacement 19.5 mm. The average roughness predicted by the model fell mostly within the range of the roughness measured in the experiments differing by 43% from the experimental average.

Both the maximum range and average roughness measured in the experiment had non-zero values before the tabs were displaced, whereas in the finite element model both were zero up to tab displacements of 15 mm. The reason for the difference was that the surface of the skin in the model was assumed to be initially perfectly smooth as discussed in Section 3.5, and the smooth skin required greater displacement to initiate wrinkle formation.

As mentioned in 4.2.2, a finite element model measuring 67.5 mm by 20 mm was constructed to quantify the effect of the boundary conditions along the long edge on the results. Only the three-layer model under a pre-stress of 2 kPa was run using both the 10 mm wide and 20 mm wide models. The maximum ranges predicted by both models differed on average by 5.0%. The average roughness predicted by both models differed on average by 4.3%. Both the maximum range and average roughness at higher tab displacements predicted by the 20 mm wide model were smaller than the maximum range and average roughness predicted by the 10 mm wide model.

Three-layer model versus one and two-layer models

No wrinkles formed in the single-layer skin model or the two-layer model consisting of the dermis and hypodermis under any displacement condition. When the tabs were displaced in the two-layer model consisting of the stratum corneum and dermis and the three-layer model, wrinkles formed.

The results predicted by the two-layer model consisting of the stratum corneum and the dermis is compared with the experimental results in Figure 4.16(a) and Figure 4.16(b). The maximum range predicted by the two-layer model differed from the mean experimental maximum range by 10%, while there was a difference of 24% between the predicted average roughness and experimental average roughness. While these percentage differences were less than the corresponding differences between the

78

three-layer model and experiment, the trends predicted by the two-layer model did not follow the experimental trends. In Figure 4.16(a), for a tab displacement of slightly greater than 17 mm, the maximum ranges predicted by the two and three-layer models closely agreed. For greater tab displacements, the slope of the curve predicted by the two-layer model decreased, whereas the slope predicted by the three-layer model increased, in agreement with the experimental measurements. The average roughness predicted by the two-layer model was very different than the average roughness predicted by the three-layer model (Figure 4.16(b)). For the two-layer model, the slope of the average roughness curve decreased with increasing tab displacements. Between tab displacements of 18.75 and 19.75 mm, there was a decrease in the average roughness. This was unlike the three-layer model, where the average roughness increased monotonically as the tab displacement increased.

A three-layer analysis was also run where the material model of the dermis was also used for the hypodermis. The thicknesses of each layer were the same as the previous three-layer model. While the maximum range and average roughness of the wrinkles in this modified three-layer model increased monotonically as before, they differed by a greater margin from the experiment (46 and 71% difference for the maximum range and average roughness, respectively). This result suggests that while including the thickness of the hypodermis in a skin model is significant when simulating the wrinkling of skin between two tabs, it is also important to accurately represent the mechanical behaviour of the hypodermis. A more accurate constitutive equation of the hypodermis may further improve the agreement between the three-layer finite element model and experimental results.

4.3.4 Parameter study

Hydration level of stratum corneum

The maximum range and average roughness of the wrinkles predicted by models with strata cornea of differing levels of hydration are shown in Figure 4.17. As the hydration level in the stratum corneum decreased, both the maximum range and average roughness of the wrinkles increased. Therefore, as the hydration level of the stratum corneum decreased, the wrinkles in the model became larger.
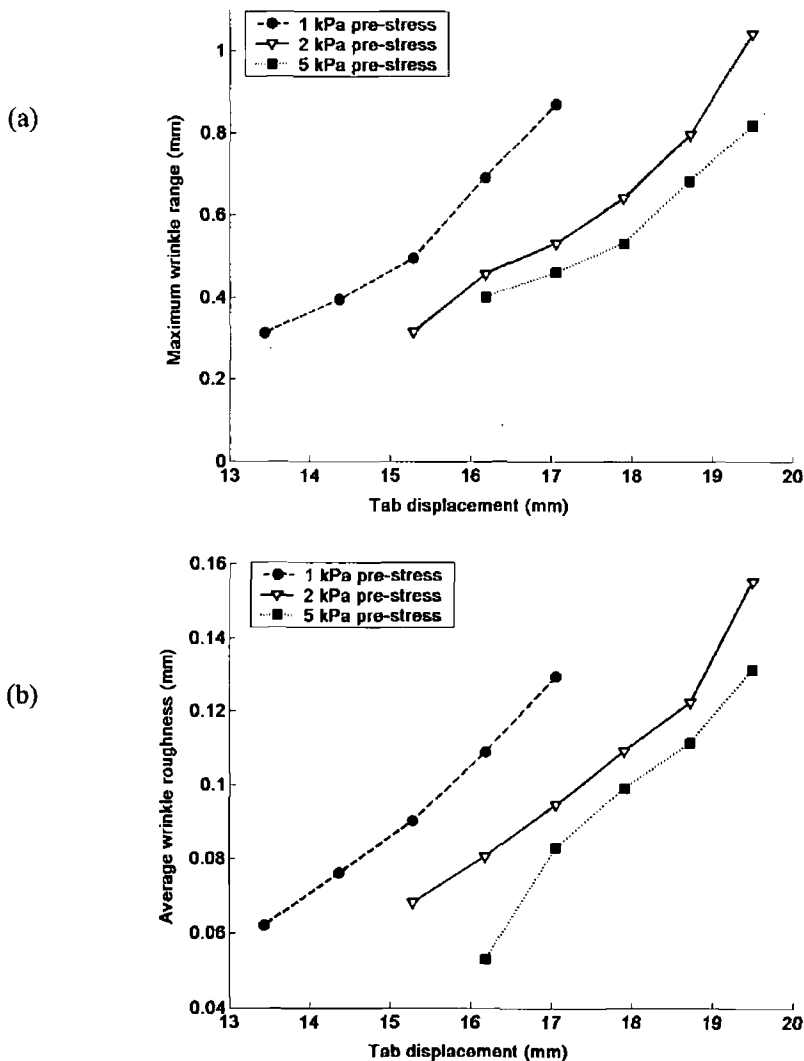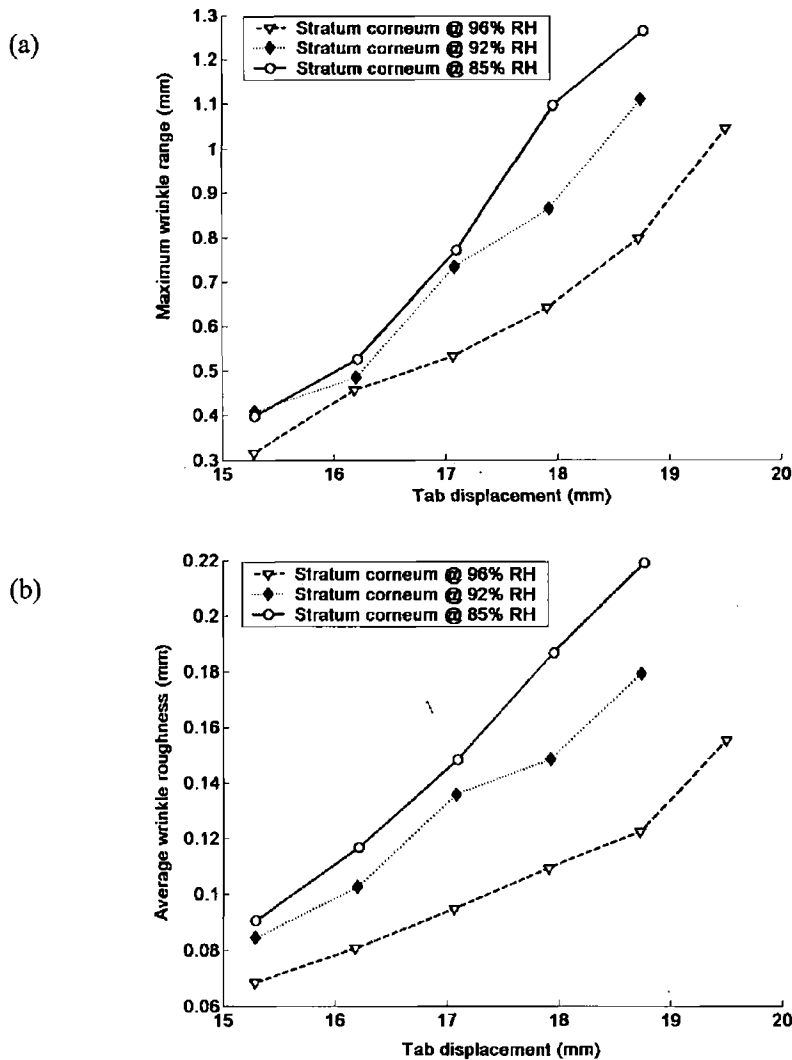
Figure 4.17: Comparing maximum range and average roughness of wrinkles predicted by the three-layer model with different strata cornea. The material parameters used for each relative humidity are in Table 4.3

Dermal collagen fibre density

The effect of varying the collagen fibre density on the formation of the wrinkles is shown in Figure 4.18. As the density of the fibres increased both the maximum range and average roughness of the wrinkles increased.

Orthotropy of skin

Figure 4.19(a) and Figure 4.19(b) compare the maximum range and average roughness of the wrinkles formed parallel to and perpendicular to the Langer's lines in the skin model under equibiaxial and unequibiaxial pre-stresses. For the equibiaxial

(a)

(b)
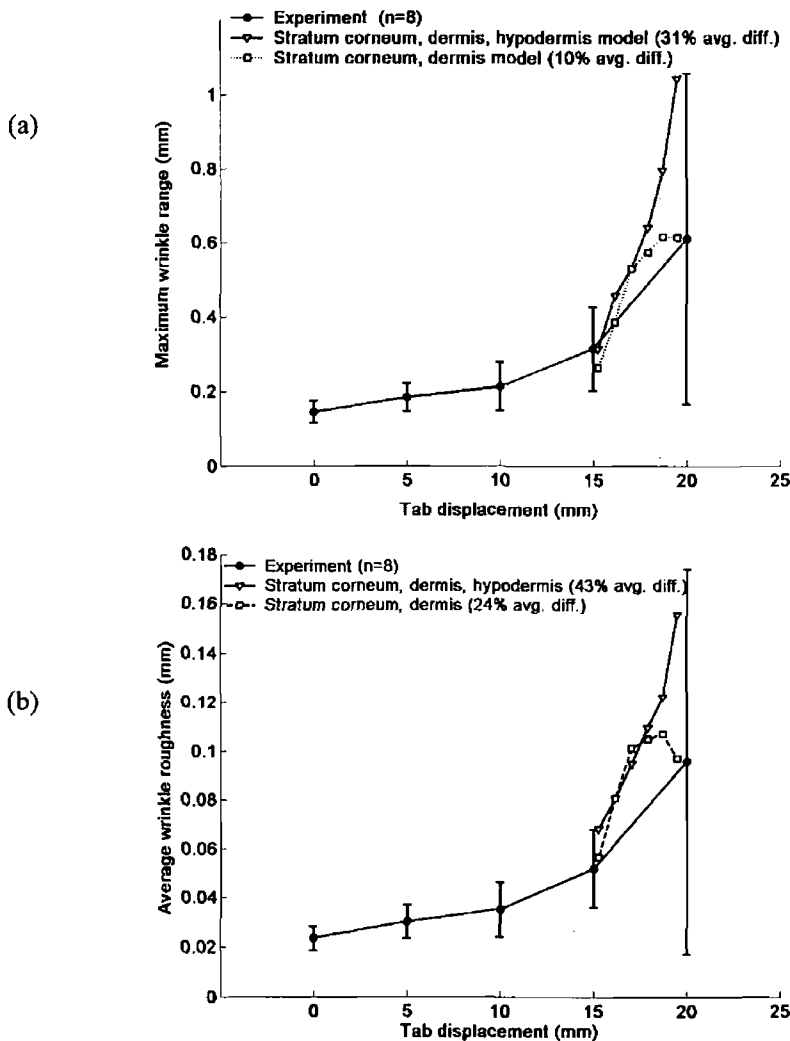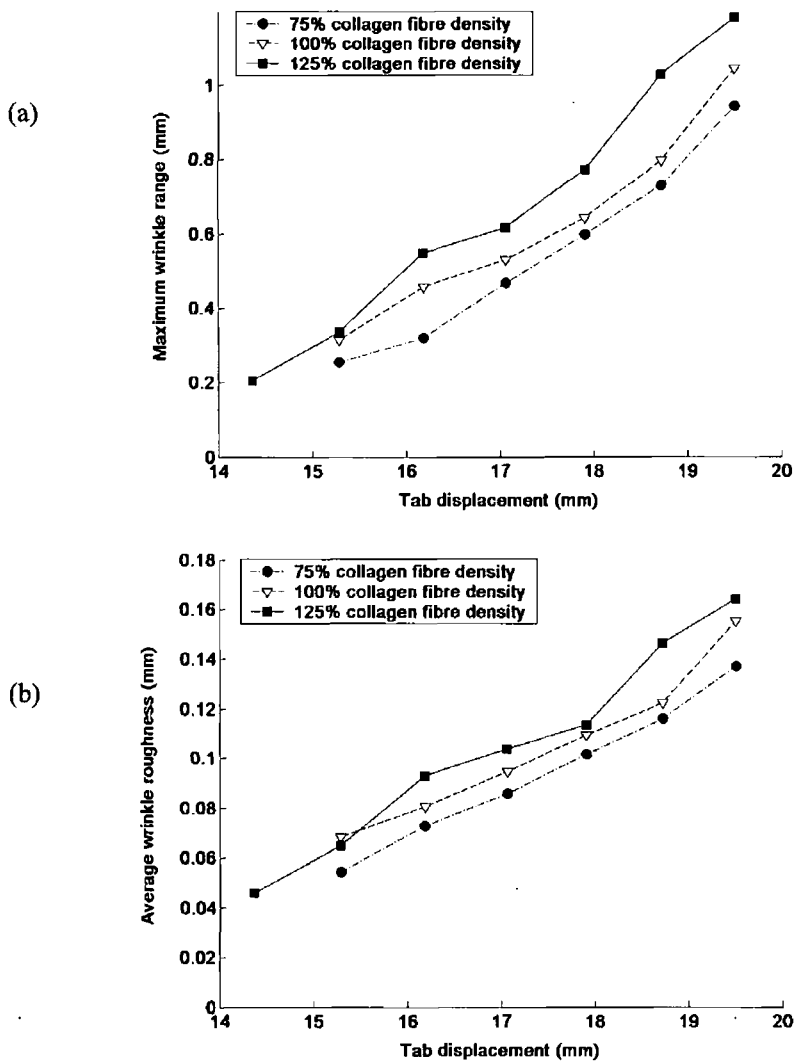
Figure 4.18: Comparing maximum range and average roughness of wrinkles predicted by the three-layer model with different collagen fibre densities in the dermis. The 100% collagen fibre density corresponds to the n_A and n_B value given in Table 3.7. The pre-stress in the skin was 2 kPa.

case, where the pre-stress parallel and perpendicular to the Langer's lines was 2 kPa, the maximum range and average roughness of the wrinkles were larger when they formed perpendicular to the Langer's lines. When the pre-stress was 4 kPa in the direction of the Langer's lines and 2 kPa perpendicular to them, the range and roughness were greater when the wrinkles were parallel to the Langer's lines.

4.3.5 Non-dimensionalising the wrinkle parameters

Numerous plots were generated showing how the maximum range and average roughness changed with respect to the tab displacement for skin models with different

81

(a)
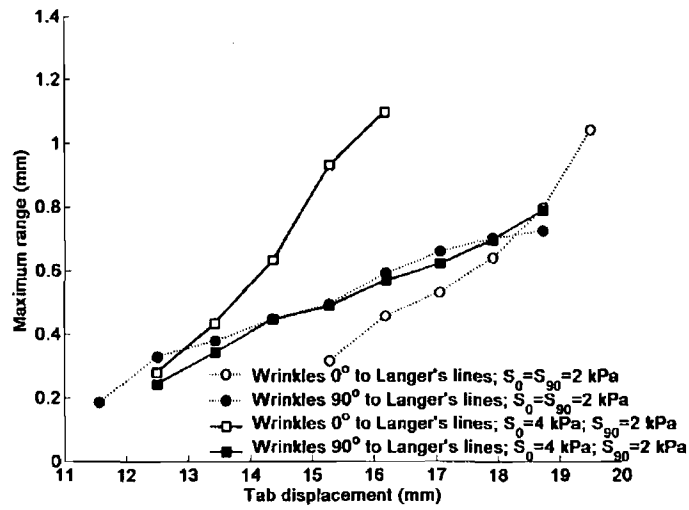
(b)
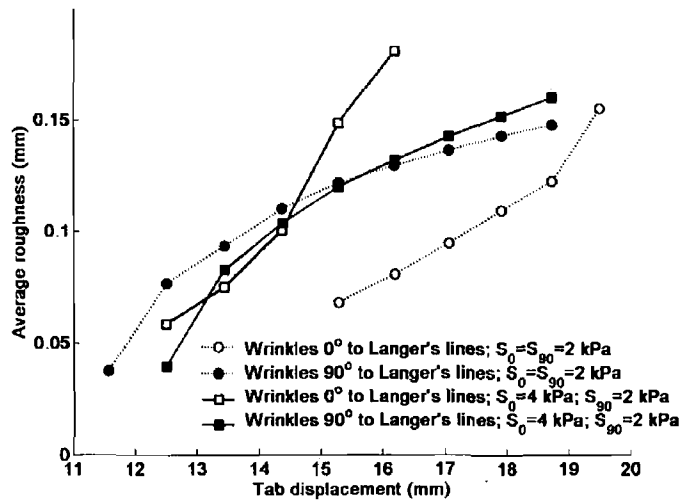
Figure 4.19: Comparing maximum range and average roughness of wrinkles predicted by the three-layer model when the wrinkles are parallel and perpendicular to the Langer's lines in the skin. S_0 and S_{90} refer to the pre-stresses in the dermis parallel to and perpendicular to the Langer's lines, respectively.

strata cornea, dermal layers and pre-stresses. It would be of benefit if a function could be found relating the maximum range and average roughness to the tab displacement. Cerda and Mahadevan (2003) derived a set of scaling laws for the amplitude and wavelength of the wrinkles in a thin sheet under tension

$$\lambda \sim \left(\frac{B}{K}\right)^{1/4} \tag{4.3}$$

$$A \sim \lambda \left(\frac{\Delta}{W}\right)^{1/2} \tag{4.4}$$

where B is the bending stiffness of the sheet; K is the effective stiffness per unit thickness of the foundation; W is the width of the sheet and Δ is the lateral deflection of the sheet (illustrated in Figure 4.20).

The configuration of the wrinkled sheet is shown schematically in Figure 4.20. If the thin sheet is assumed to be the stratum corneum and the foundation is the hypodermis, the scaling laws could be adopted for the case of wrinkling skin between two displacing tabs. Combining the amplitude and wavelength scaling laws, rearranging and replacing the amplitude A with the maximum range R_{max} gives

$$\frac{R_{max}}{\left(B_{sc}/K_H\right)^{1/4}} \sim \left(\frac{\Delta}{W}\right)^{1/2} \qquad (4.5)$$

where B_{sc} is the bending stiffness of the stratum corneum; K_H is the stiffness per unit thickness of the hypodermis in the direction of the tab displacement when the pre-stress is applied; Δ is the displacement of the tabs and W is the original distance between the two tabs. B_{sc} can be calculated from

$$B_{sc} = \frac{E_{sc}h^3}{12\left(1-v^2\right)} \qquad (4.6)$$

Figure 4.21(a) shows the maximum range and tab displacement non-dimensionalised according to Equation 4.5. The predicted results from the various finite element analyses collapse to a reasonable degree on to the linear line with an R^2 value of 0.84. Figure 4.21(b) shows that the average roughness predictions also collapse reasonably well when non-dimensionalised by the same quantities as the
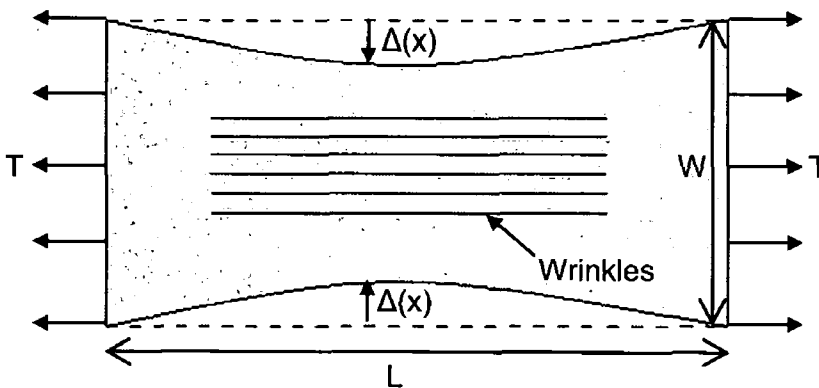
Figure 4.20: Schematic of wrinkles forming in a sheet of length L and width W under a tension T. As the sheet is stretched, the sides displace inwards a distance $\Delta(x)$. This configuration is similar to the case of the skin wrinkling between two tabs, where W is the initial distance between the tabs and $\Delta(x)$ is their displacement.

(a)

(b)
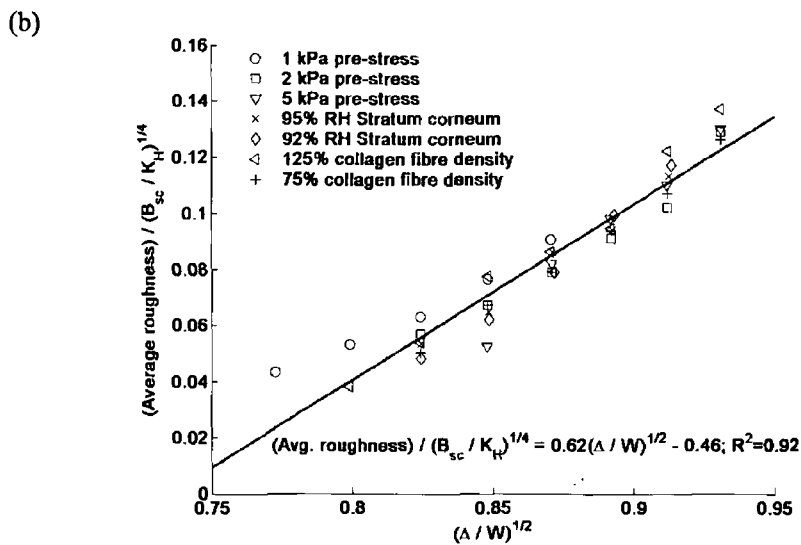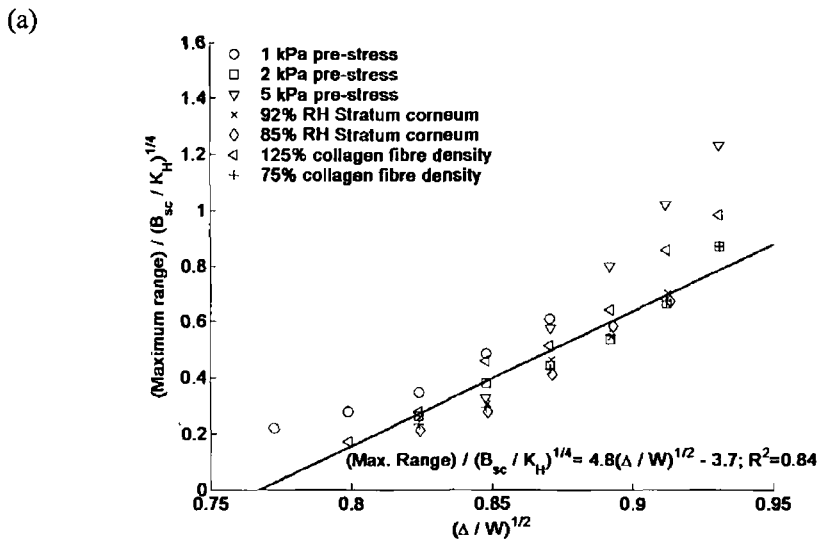
Figure 4.21: Non-dimensional (a) maximum range and (b) average roughness as a function of the non-dimensional tab displacement $(\Delta/W)^{1/2}$. B_{sc} is the bending stiffness of the stratum corneum; K_H is the stiffness of the hypodermis in the direction of the tab displacement when the pre-stress is applied. The best-fit linear line for all the data points is given in each plot.

maximum range. The data was fitted to the linear line with an R^2 value of 0.92. This would suggest that the average roughness of the wrinkles can be related to the tab displacement by

$$\frac{Avg.\ Roughness}{\left(B_{sc}/K_H\right)^{1/4}} \sim \left(\frac{\Delta}{W}\right)^{1/2} \tag{4.7}$$

While Equations 4.5 and 4.7 describe, for many of the finite element analyses, the behaviour of the maximum range and average roughness of wrinkles, they do not account for the orthotropic nature of skin. Consequently, the results contained in

84

Figure 4.19(a) and Figure 4.19(b) do not fit with the linear functions in Figure 4.21(a) and Figure 4.21(b). Equations 4.5 and 4.7 would need to be developed further to contain either the stresses or the stiffnesses of the dermis in the direction perpendicular to and parallel to the tab skin displacement. Further development would also be needed to take into account other variables such as the thickness of each of the layers.

Equations 4.5 and 4.7 clearly show how each of the variables influence the wrinkling behaviour. The next step in the development would be to apply these relationships to *in vivo* real skin. Batisse *et al.* (2002) developed a qualitative wrinkling scale and correlated it with certain mechanical properties. This correlation could be used to evaluate skin quality. The analytical relationships, Equations 4.5 and 4.7, also have the potential to be used to assess the quality of a person's skin. From a measurement of the wrinkles of a patient, an estimate of the stiffness of each skin layer could be made using a form of the equations displayed in Figure 4.21(a) or Figure 4.21(b). This quantitative approach may be an improvement over the qualitative approach of Batisse *et al.* (2002).

4.4 Summary

In this chapter, a novel experimental method has been devised to wrinkle volar forearm skin in a controlled manner and measure the surface profile using a tested laser profilometer system. The wrinkles were quantified in terms of their maximum range and average roughness. A series of single and multi-layer finite element models were developed to simulate the experiment. The single-layer model and a two-layer model representing the dermis and hypodermis were unable to simulate the wrinkling of skin. The two-layer model representing the stratum corneum and dermis predicted the maximum range and average roughness up to intermediate tab displacements with reasonable accuracy. For larger tab displacements, however, the maximum range and average roughness did not increase monotonically as measured in the experiment. In the three-layer model, the predicted maximum range differed by 31% from the mean of the maximum ranges measured in the experiment, while the average roughness differed by 43% from the mean measured value. While these differences may seem large, the three-layer model representing the stratum corneum, dermis and hypodermis was the best model to simulate the wrinkling of skin over a larger range of tab

displacements. It can simulate the wrinkling of skin better than any existing single or two-layer model.

The size of the wrinkles in the model increased in size when the hydration level of the stratum corneum was reduced, the pre-stress in the skin was reduced or the density of the collagen fibres was increased. Larger wrinkles formed parallel to the Langer's lines in the model only when the pre-stress parallel to the Langer's lines was greater than the pre-stress perpendicular to them.

Finally, when the maximum range and average roughness were non-dimensionalised by several of the model parameters, the results predicted by the different finite element analyses collapsed to a reasonable degree on to the same linear line.

Chapter 5

A simplified model of scar contraction

5.1 Introduction

In this chapter, the simple model of a contracting scar originally proposed by Cerda (2005) is further developed. Firstly, the latex experiments of Geminard *et al.* (2004) were simulated using both finite element and analytical techniques. This was done to validate the finite element and analytical models developed. Following this, finite element models were developed to simulate the behaviour of skin around a contracting 'scar'. Laboratory experiments were also conducted analysing the behaviour of real skin around a contracting 'scar' model. These experiments were compared with the finite element analyses. The comparisons show the importance of including the orthotropic characteristics of skin in the model.

5.2 Modelling isotropic membranes around contracting 'scars'

In this study, a finite element model was developed that simulated the experiments carried out by Geminard *et al.* (2004). Comparing the results of the simulations against their experimental data offers a means of validating the finite element model. Modelling their simplified experiment of a contracting scar in a linear elastic material was the first step in the development of a finite element model of the wrinkling process in skin.

In addition to the finite element model, a simplified analytical model was derived to predict the pattern of wrinkling around circular 'scars'. The development follows the approach Wong and Pellegrino (2006) took when analysing the wrinkling of square solar sails. The analytical model offers a means of validating the results of the

finite element model. Indeed, an analytical model is beneficial in its own right as it can produce results more quickly than a finite element model.

5.2.1 Material and methods

Finite element study

The experimental configuration of Geminard *et al.* (2004) consisted of a circular membrane of latex suspended horizontally in a frame. A tension was applied to the membrane by applying an outward radial displacement β to the circumference of the membrane. A vertical tube of radius R_i was located underneath the centre of the membrane. The pressure in the tube was reduced by means of a pump and the membrane was sucked down into the tube. When there was a critical radial displacement of the membrane at the edge of the tube, wrinkles spread out radially towards the edge. The number, length and amplitude of the wrinkles were measured via an optical measurement system. The effect of varying the tube radius R_i outer radial displacement β and inner radial displacement δ were investigated.

A finite element model of the experiment was developed using ABAQUS/Explicit Version 6.5.1. A schematic of the model is shown in Figure 5.1. As the problem was assumed to be symmetrical, only one-quarter of the membrane and vertical tube was modelled. Symmetrical boundary conditions were applied along each straight edge. The outer edge of the membrane was fixed in the vertical direction. As in the experiment by Geminard *at al.* (2004), the latex membrane had a radius of 18.5 cm and a thickness of 0.2 mm. Comparing the thickness of the latex modelled with human skin, the epidermis varies in thickness from 0.06 mm to 0.8 mm, while the dermis varies from 0.5 mm to 2.0 mm (Lee and Hwang, 2002). The density of latex was specified as 995 kg/m^3.

The latex material was modelled using the Yeoh hyperelastic strain energy function whose form is given by

$$W = C_{10}\left(\overline{I}_1 - 3\right) + C_{20}\left(\overline{I}_1 - 3\right)^2 + C_{30}\left(\overline{I}_1 - 3\right)^3 + 1/D_1\left(J - 1\right)^2 \tag{5.1}$$

where W is the strain energy per unit of reference volume; C_{i0} and D_i are material parameters; $\overline{I}_1 = \overline{\lambda}_1^2 + \overline{\lambda}_2^2 + \overline{\lambda}_3^2$ is the first deviatoric strain invariant, where the deviatoric stretches $\overline{\lambda}_i = J^{-1/3}\lambda_i$; J is the total volume ratio; and λ_i are the principal stretches (Hibbitt *et al.*, 2004).

88
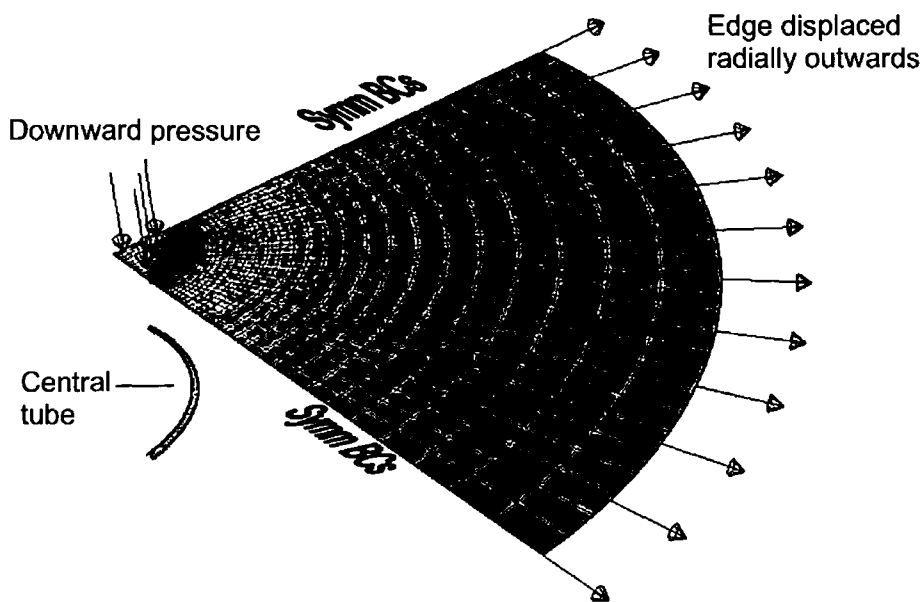
Figure 5.1: Finite element model - one quarter of membrane is modelled; Latex membrane meshed using approximately one layer of 11700 S4R shell elements; Edge displaced radially outwards during first step; Downward pressure applied smoothly over the inside area of the tube during second step.

The material parameters were found by fitting the hyperelastic function to experimental biaxial stretch data of natural rubber (Bergstrom, 2006) with an error of 4.04% and an R^2 value of 0.992. The curve-fit is shown in Figure 5.2.

The latex membrane was meshed using S4R shell elements. The top edge of the vertical tube was generated as a discrete rigid body. It was only necessary to model the top edge as the latex membrane did not make contact with the sides below this. We assumed the fillet radius of the top edge of the tube to be 0.5 mm. Contact between the latex membrane and the vertical tube was modelled using the kinematic contact method and was considered frictionless. The tube was designated the master surface and the latex membrane the slave surface. A very high mesh density was generated in the membrane where the latex made contact with the tube. Approximately 11900 nodes and 11700 elements were used in each analysis. Due to the very high mesh density and the high stiffness of the latex material modelled, mass scaling techniques were used to increase the stability limit and hence reduce analyses run-times. Mass scaling was described in detail in Section 4.2.2. For the analyses run in this study the density was increased by a factor of 1000 in order to achieve favourable stability limits. To ensure the mass scaling was not having a dynamic
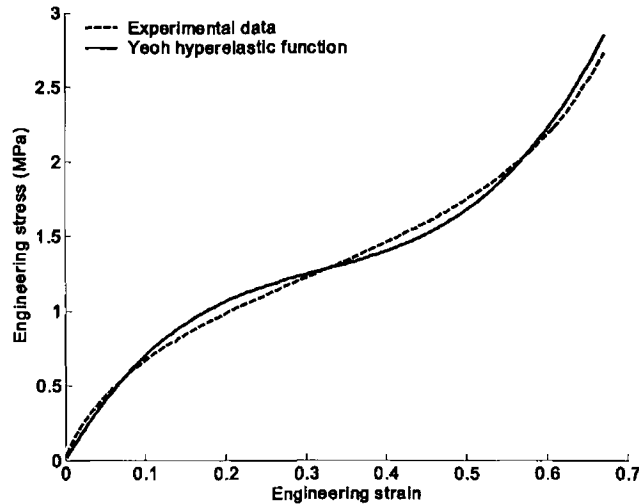
Figure 5.2: Fitting of hyperelastic Yeoh function to experimental biaxial stretch data of natural rubber; Yeoh function parameters are $D_1=5.298 \times 10^{-2}$ MPa^{-1}, $C_{10}=0.7652$ MPa, $C_{20}=-0.1594$ MPa, $C_{30}=4.4798 \times 10^{-2}$ MPa; Error=4.04%, $R^2=0.99208$; Experimental data from (Bergstrom, 2006)

effect on the results, it was checked that kinetic energy of the system did not exceed 5% of the total energy over most of each analysis, as recommended in the ABAQUS User Manuals (Hibbitt et al., 2004).

Analyses were ran with the five different hole radii that Geminard et al. (2004) used for the central tube – 8, 14, 19, 26 and 31 mm. Each analysis consisted of two steps. In the first step, the edge of the latex membrane displaced radially outwards by a fixed distance. The displacement was applied smoothly over 5 seconds. In the second step, a downward pressure was applied on the membrane over an area slightly smaller than the cross-sectional area of the tube. The pressure was applied smoothly over a period of 15 seconds. The time period was chosen so that the kinetic energy did not exceed 5% of the total energy. Two outer-edge displacements were considered – 2.4 and 5.6 mm. The two displacements would show the effect that different membrane tensions have on the wrinkle development. This was relevant in the context of skin as the tension of skin depends on several factors including the location on the body and age (Wilkes et al., 1973). The number, amplitude and length of the wrinkles that developed in each case were analysed.

Analytical model

To develop a simplified analytical model an annular membrane of outer radius R_o, inner radius R_i and thickness h was considered. A radial displacement β is imposed along its outer edge, while a displacement $-\delta$ is imposed along the edge of the inside hole of the membrane as shown in Figure 5.3. As the inside edge is drawn inwards, wrinkles radiate out towards the edge of the membrane occupying a zone of radius R_w. Outside this radius there are no wrinkles because the membrane is in tension in all directions. The radial and hoop stresses in this region are positive and are given by (Wang, 1953)

$$\sigma_r^{outer} = \frac{E}{1-v^2}\left[(1+v)\frac{\delta R_i + \beta R_o}{R_o^2 - R_i^2} + (1-v)\frac{\delta R_o + \beta R_i}{R_o^2 - R_i^2}\frac{R_o R_i}{r^2}\right] \tag{5.2}$$

$$\sigma_\theta^{outer} = \frac{E}{1-v^2}\left[(1+v)\frac{\delta R_i + \beta R_o}{R_o^2 - R_i^2} - (1-v)\frac{\delta R_o + \beta R_i}{R_o^2 - R_i^2}\frac{R_o R_i}{r^2}\right] \tag{5.3}$$

while the displacement field is given by

$$u_r^{outer}(r) = \frac{\delta R_i + \beta R_o}{R_o^2 - R_i^2}r - \frac{\delta R_o + \beta R_i}{R_o^2 - R_i^2}\frac{R_o R_i}{r} \tag{5.4}$$

Strictly speaking, Equations 5.2, 5.3 and 5.4 apply to situations where the membrane is under stress and there is no wrinkling in any part of it. In this wrinkling theory, these equations are assumed to be correct where the membrane is in tension. In
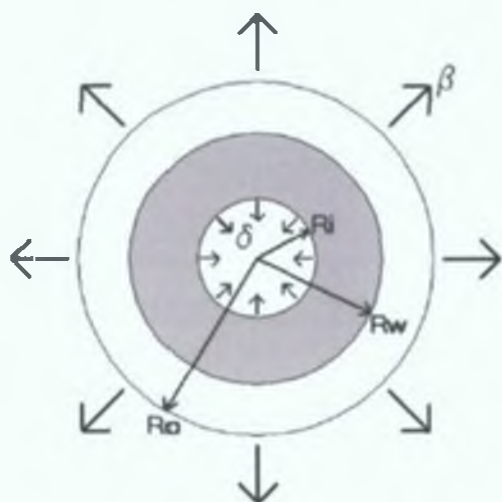
Figure 5.3: Analytical model sketch: An annular membrane of outside radius R_o and inside radius R_i is subjected to an outer radial displacement β and inner radial displacement δ. The shaded area is the wrinkled zone, which has a radius R_w. The membrane was assumed to be thin compared to other dimensions.

regions where there is wrinkling, the stress and displacement equations are corrected for these areas only; the stress and displacement fields outside the wrinkled regions remain unchanged. This assumption is also used in other wrinkling theories such as the relaxed strain energy approach demonstrated by Haughton and McKay (1995).

The wrinkle radius R_w is assumed to be the point at which the hoop stress equals zero and so from Equation 5.3

$$R_w = \sqrt{\frac{1-v}{1+v}\frac{\delta R_o + \beta R_i}{\delta R_i + \beta R_o} R_o R_i}$$

(5.5)

Inside R_w, the hoop stress is assumed to be negligible compared to the radial stress and so a uniaxial stress field exists. A uniaxial stress field of the form $\sigma_r^{inner} = C_1/r$ satisfies the equilibrium condition $\partial\sigma_r^{inner}/\partial r + \sigma_r^{inner}/r = 0$. The radial displacement field inside the wrinkling zone is given by

$$u_r^{inner} = \frac{1}{E}\int\sigma_r^{inner}dr$$

(5.6)

Substituting in for σ_r^{inner} and using the boundary conditions $u_r^{inner}(R_i) = -\delta$, $u_r^{inner}(R_w) = -\alpha$, the constant C_1 can be found. The radial stress inside the wrinkle zone works out to be

$$\sigma_r^{inner} = \frac{E(\alpha + \delta)}{\ln(R_w/R_i)}\frac{1}{r}$$

(5.7)

where α is the radial displacement of the membrane at the wrinkle radius and is given by

$$\alpha = u_r^{outer}(R_w) = \frac{\delta R_i + \beta R_o}{R_o^2 - R_i^2}R_w - \frac{\delta R_o + \beta R_i}{R_o^2 - R_i^2}\frac{R_o R_i}{R_w}$$

(5.8)

Similar to Wong and Pellegrino (2006), it is assumed that the profile of the membrane inside R_w is given by

$$w(r,\theta) = A_m \sin\frac{\pi(r - R_i)}{R_w - R_i}\sin n\theta$$

(5.9)

where A_m is the maximum amplitude of the wrinkles and n is the number of wrinkles. A schematic of a single wrinkle is shown in Figure 5.4(a). To derive an expression for n, consider the equilibrium of a small element of a crest of a wrinkle in Figure 5.4(b) as per Wong and Pellegrino (2006). The equilibrium equation for the out-of-plane forces is

$$\kappa_r\sigma_r^{inner} + \kappa_\theta\sigma_\theta^{inner} = 0$$

(5.10)

92
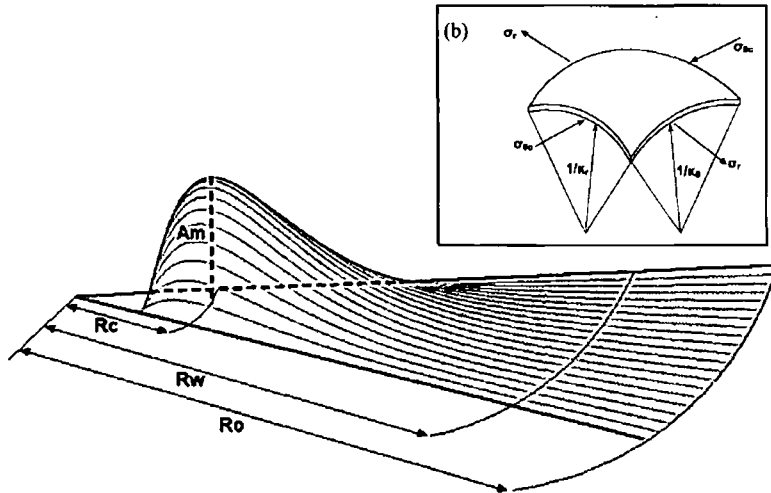
Figure 5.4: Schematic of single wrinkle showing radius to centre of wrinkle R_c, wrinkle zone radius R_w, radius of membrane R_0 and maximum wrinkle amplitude A_m. Inset (b): Out-of-plane equilibrium of wrinkled membrane at a point of maximum wrinkle amplitude: The critical stress, $\sigma_{\theta c}$, is equal to the buckling stress of a thin membrane of wavelength λ.

where $\kappa_r = -\dfrac{\partial^2 w}{\partial r^2}$ is the radial curvature and $\kappa_\theta = -\dfrac{1}{r^2}\dfrac{\partial^2 w}{\partial \theta^2}$ is the hoop curvature.

The centre of a wrinkle is where the curvatures are a maximum and is found from setting $\partial \kappa_r / \partial r = 0$ and $\partial \kappa_\theta / \partial r = 0$. This gives the centre of the wrinkle at radius R_c

$$R_c = \frac{R_w + R_i}{2} \tag{5.11}$$

The curvatures at R_c are therefore

$$\kappa_{rc} = \frac{A\pi^2}{\left(R_w - R_i\right)^2} \tag{5.12}$$

$$\kappa_{\theta c} = \frac{4An^2}{\left(R_w + R_i\right)^2} \tag{5.13}$$

The radial stress at R_c is

$$\sigma_{rc} = \frac{E(\alpha + \delta)}{\ln(R_w/R_i)}\frac{2}{R_w + R_i} \tag{5.14}$$

Wong and Pellegrino (2006) assumed the hoop stress to be equal to the critical buckling stress of a membrane of thickness h and width $\lambda = 2\pi R_c/n$

$$\sigma_{\theta c} = -\frac{\pi^2 E h^2}{12(1 - v^2)\lambda^2} \tag{5.15}$$

Substituting Equations 5.12, 5.13, 5.14 and 5.15 into Equation 5.10 and rearranging gives

$$n = \sqrt[4]{\frac{6\pi^2\left(1-v^2\right)\left(\alpha+\delta\right)\left(R_w+R_i\right)^3}{h^2\left(R_w-R_i\right)^2 \ln\left(R_w/R_i\right)}}$$ (5.16)

To find the amplitude A of the wrinkle, we look at the strain field inside the wrinkle zone. When there are wrinkles, the hoop strain ε_θ is greater than the material hoop strain, $\varepsilon_{\theta M}$. The balance is provided by the geometric hoop strain due to the out-of-plane deflection of the wrinkling formation

$$\varepsilon_\theta = \varepsilon_{\theta M} + \varepsilon_{\theta G}$$ (5.17)

The hoop strain is given by

$$\varepsilon_\theta = \frac{u^{inner}\left(R_c\right)}{R_c}$$ (5.18)

where the displacement field $u^{inner}(r)$ is purely radial and given by

$$u^{inner}(r) = \int \varepsilon_r dr$$

$$= \frac{1}{E}\int \sigma_r dr$$ (5.19)

$$= \frac{\alpha+\delta}{\ln\left(R_w/R_i\right)}\ln r + C_1$$

Since $u_r^{inner}\left(R_i\right) = \delta$, the constant C_1 can be found giving

$$u_r^{inner}(r) = \frac{\alpha+\delta}{\ln\left(R_w/R_i\right)}\ln\left(\frac{r}{R_i}\right) - \delta$$ (5.20)

The hoop strain at R_c is then given by

$$\varepsilon_\theta = \frac{2}{R_i+R_w}\left(\frac{\alpha+\delta}{\ln\left(R_w/R_i\right)}\ln\left(\frac{R_i+R_w}{2R_i}\right) - \delta\right)$$ (5.21)

The material hoop strain can be written

$$\varepsilon_{\theta M} = -v\frac{\sigma_{rc}}{E}$$

$$= -\frac{v\left(\alpha+\delta\right)}{\ln\left(R_w/R_i\right)}\frac{2}{R_w+R_i}$$ (5.22)

Wong and Pellegrino (2006) derived an expression for the out-of-plane hoop strain

$$\varepsilon_{\theta G} = -\frac{\pi^2 A^2}{4\lambda^2}$$

$$= -\frac{A^2 n^2}{4\left(R_w+R_i\right)^2}$$ (5.23)

Substituting Equations 5.21, 5.22 and 5.23 into 5.17 and solving for the amplitude A gives

$$A = \frac{1}{n} \sqrt{8(R_w + R_i)\left(\delta - \frac{\alpha + \delta}{\ln(R_w/R_i)}\left(\ln\frac{R_w + R_i}{2R_i} + v \right) \right)} \qquad (5.24)$$

It should be noted that many of the governing equations used in the development are only valid for small linear deformations. Therefore, the analytical model is only applicable in cases where the strains are small. A summary of the analytical model is shown in Figure 5.5.

Length scale for circular scars

From the analytical model the number of wrinkles is given by Equation 5.16. The wavelength of the wrinkles is

$$\lambda = \pi\frac{(R_w + R_i)}{n} \qquad (5.25)$$

Substituting Equation 5.16 into 5.25 gives

$$\lambda = \left(\frac{\pi^2 h^2 (R_w - R_i)^2 (R_w + R_i)\ln(R_w/R_i)}{6(1 - v^2)(\alpha + \delta)} \right)^{\frac{1}{4}} \qquad (5.26)$$

The radial stress applied along the edge of the centre hole is given by Equation 5.7

$$\sigma_r^{inner}(R_i) = \frac{E(\alpha + \delta)}{\ln(R_w/R_i)}\frac{1}{R_i} \qquad (5.27)$$

The force per unit length T_{fi} applied along the edge of the hole is found by multiplying

Known variables: R_o, R_i, δ, β, v, h

Calculate the radius of the wrinkle zone R_w using Equation 5.5

Calculate α, the radial displacement at R_w, using Equation 5.8

Calculate the number of wrinkles n from Equation 5.16

Calculate the amplitude of the wrinkles A from Equation 5.24
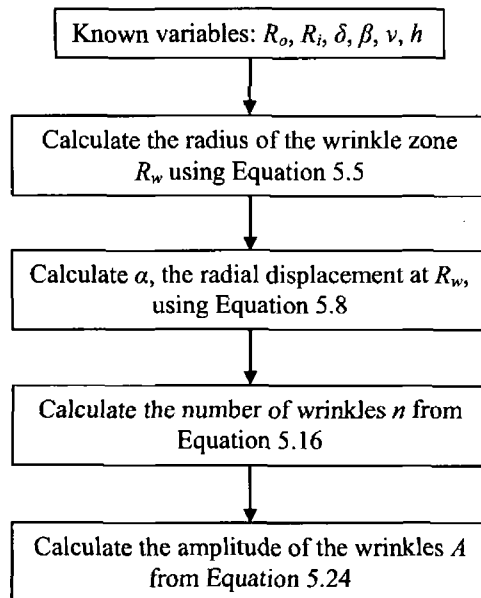
Figure 5.5: Summary of procedure to calculate the radius of the wrinkle zone, the number of wrinkles and the amplitude of the wrinkles.

Equation 5.27 by h. Substituting T_{fi} into Equation 5.26 gives

$$\lambda = \left(\frac{\pi^2 E h^3 (R_w - R_i)^2 (R_w + R_i)}{6(1 - v^2) R_i T_{fi}} \right)^{\frac{1}{4}}$$

(5.28)

The bending stiffness of a membrane of thickness h is

$$B = \frac{E h^3}{12(1 - v^2)}$$

(5.29)

Therefore the wavelength of the wrinkles in the circular membrane are given by

$$\lambda = 2\sqrt{\pi} \left(\frac{B}{T_{fi}} \right)^{1/4} \left(\frac{(R_w - R_i)^2 (R_w + R_i)}{8 R_i} \right)^{1/4}$$

(5.30)

Rearranging Equation 5.23 gives

$$A = \frac{\sqrt{2}\lambda}{\pi} \sqrt{-2\varepsilon_{\theta G}}$$

(5.31)

These two expressions compare with Cerda and Mahadevan (2003) who derived the wavelength and amplitude of wrinkles in a stretched rectangular sheet of length L and width W

$$\lambda = 2\sqrt{\pi} \left(\frac{B}{T_{fi}} \right)^{1/4} (L)^{1/2}$$

(5.32)

$$A = \frac{\sqrt{2}\lambda}{\pi} \left(\frac{\Delta}{W} \right)^{1/2}$$

(5.33)

5.2.2 Results of finite element and analytical models

Figure 5.6 shows the finite element result obtained when a pressure is applied to a central circular area of a latex membrane under tension. A uniform array of wrinkles has radiated out from the circular 'scar'.

Number of wrinkles

As can be seen from Figure 5.7, the number of wrinkles increased linearly with increasing 'scar' radius. There were more wrinkles when the tension in the membrane increased. Both these trends agree with the experimental results of Geminard et al. (2004). The slopes of the linear relationships were similar between the experiments and the models. However, the number of wrinkles predicted by the finite element model was about 72% higher than the number observed in experiment for the case of
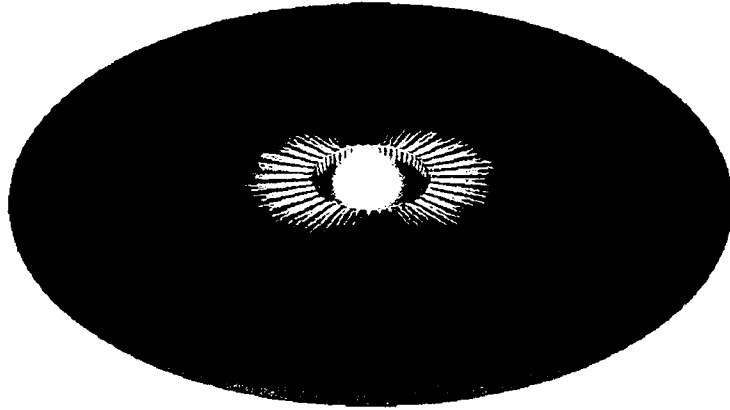
Figure 5.6: Wrinkles radiating out from a circular 'scar' in a latex membrane: R_i=19 mm, β=2.4 mm, δ≈4.9 mm for the model of Figure 5.1
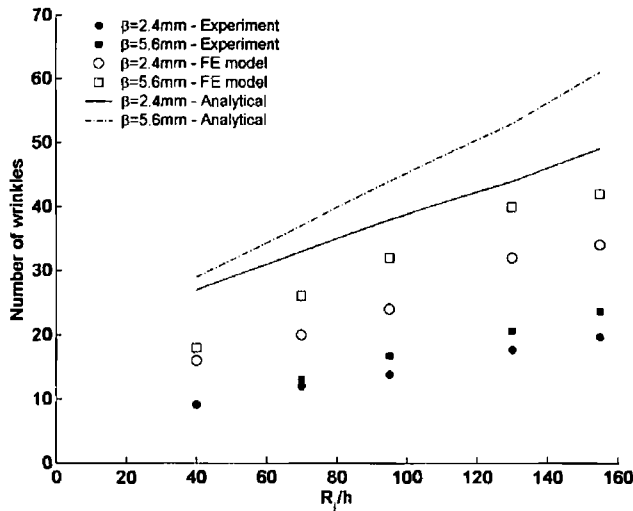
Figure 5.7: Comparison between experiment and models for the number of wrinkles, n vs. R_i/h

β=2.4 mm and 90% higher for the case of β=5.6 mm. The numbers of wrinkles predicted by the analytical model is even greater with a predicted number 167% higher than the number observed in experiment when β=2.4 mm and 144% higher when β=5.6 mm.

Amplitude of the wrinkles

Figure 5.8 shows the increase of the maximum amplitude of the wrinkles A_m as the inward displacement δ at the edge of the 'scar' increases. As the initial tension in the membrane β increases A_m decreases. There was a 20% difference in the maximum amplitudes between the finite element model and the experiment for the case of R_i=19

97
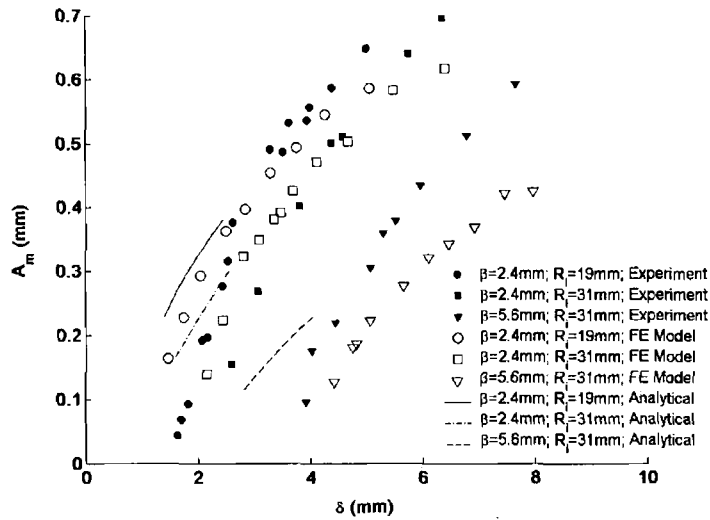
Figure 5.8: Comparison between experiment, finite element and analytical models for the amplitude of wrinkles vs. δ.

mm and β=2.4 mm and there was a 12% difference when R_i=31 mm and β=2.4 mm. These are within the error of the experiment as determined by Geminard et al. (2004). The difference in amplitudes measured in the experiment and amplitudes predicted by the simulation increases to about 42% when R_i=31 mm and β=5.6 mm.

For the analytical model, there was a much larger difference in its predicted maximum amplitudes than those measured in the experiments for the cases of R_i=19 mm, β=2.4 mm and R_i=31 mm, β=2.4 mm – 72% and 31% respectively. For the case of R_i=31 mm, β=5.6 mm, the analytical model predicts an amplitude with a similar error to the finite element model with a difference of only 44%. It should be remembered that the analytical model errors are calculated over a smaller range of δ due to the assumption of small deformations.

Length of the wrinkles

The criterion used to determine the length of a wrinkle in the finite element models was different than the criterion used in the experiments. Geminard et al. (2004) smoothed the experimental data and defined the end-point of a wrinkle to be where the slope of the profile becomes constant, i.e. $\partial^2 A_m / \partial r^2 = 0$. The wrinkle profile from the finite element results was a little noisy beyond a certain length and the slope of the profile does not stay constant. An example of this is seen in Figure 5.9. Therefore, it was difficult to unambiguously determine the length of a wrinkle using the criterion of

98
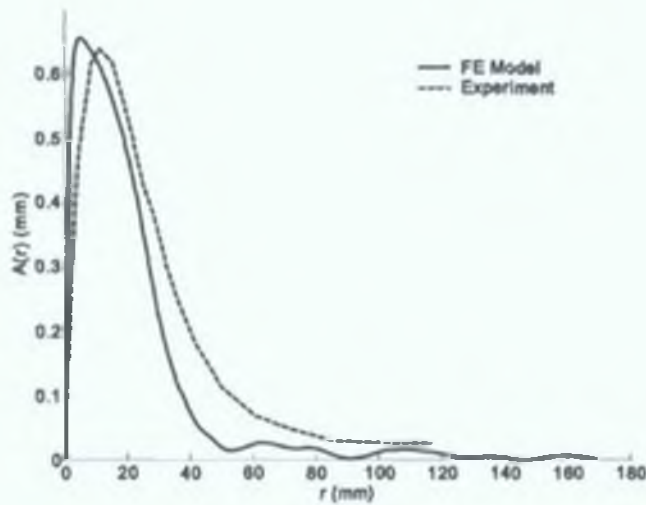
Figure 5.9: Comparison between experiment and model for the wrinkle profile vs. radius r: R_i=19 mm, β=2.4 mm, $\delta\approx$4.9 mm

Geminard *et al.* (2004). For this reason, the criterion used to determine the length of a wrinkle in the finite element models was similar to the criterion used in the analytical model, i.e. the point where the hoop stress becomes zero.

As a result of the different criteria used in the experiments and models, the wrinkle lengths predicted by the models were less than the lengths measured in the experiments (Figure 5.10). Similar trends were observed between the experiments and models. The wrinkle lengths increased in a linear fashion as δ increased and decreased as the initial tension in the membrane was increased. The wrinkle lengths predicted by the analytical and finite element models are very close to each other, differing by, at most, 5% in the regions where the analytical model was valid.

The errors of the analytical and finite element models compared to the experiment are summarised in Table 5.1.

5.2.3 Discussion

The proposed finite element model in this study showed good agreement with the wrinkling behaviour observed in the latex membrane experiments of Geminard *et al.* (2004). In addition, despite its relative simplicity, the analytical model provided a good replication of the pattern of wrinkling around a contracting circular 'scar'.

The results show the role of membrane tension in limiting the length of the wrinkles. This is important in the context of skin in which there is a resting tension whose magnitude varies according to the location on the body (Wilkes *et al.*, 1973).
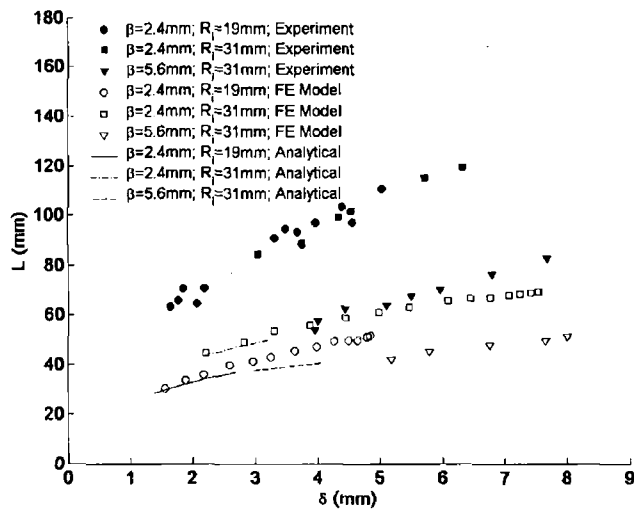
Figure 5.10: Comparison between experiment, finite element and analytical models for the length of wrinkles vs. δ

Table 5.1: Percentage errors between the predicted values of the models and the corresponding values measured in the experiments

	Case	Finite element model	Analytical model
Number of wrinkles	β=2.4mm	72%	167%
	β=5.6mm	90%	144%
Maximum amplitude	R_i=19mm; β=2.4mm	20%	72%
	R_i=31mm; β=2.4mm	12%	31%
	R_i=31mm; β=5.6mm	42%	44%
Length[1]	R_i=19mm; β=2.4mm	-	5%
	R_i=31mm; β=2.4mm	-	4%

1: The lengths predicted by the analytical and finite element models are compared with each other and not with the experiment as a different criterion was used to determine the wrinkle length. No comparison was made for the R_i=31mm β=5.6mm case because the analytical model extended up to δ=4mm and the FE model result only began at δ=5mm

100

As in the numerical model proposed by Geminard *et al.* (2004), the finite element model predicted a larger number of wrinkles than observed in experiment. These differences may be attributed to the assumption of frictionless contact between the latex membrane and the tube. Although Geminard *et al.* (2004) took steps to minimise the effect of friction, it probably was not eliminated entirely. The wavelength of wrinkles is a compromise between the bending energy and the strain energy in the membrane (Cerda and Mahadevan, 2003). The inclusion of friction in the finite element model may have a significant effect on this balance and influence the number of wrinkles.

Other differences between the experimental, finite element and analytical results could be attributed to the constitutive models used for the latex. The analytical model assumed the latex membrane to be linear elastic. Although many elastomers are presumed to be linear elastic at low strains, this is increasingly invalid as strains increase (Bergstrom and Boyce, 1998). In the finite element model, the Yeoh hyperelastic function was used to model the latex material. The function was fitted to biaxial tension data of natural rubber (Bergstrom, 2006) with good accuracy (4% error) but this data may not be representative of the latex material used in the experiments of Geminard *et al.* (2004). Latex comes in a wide variety of forms (Roff, 1971).

Although relatively simple, the analytical model is a useful tool in estimating the characteristics of the wrinkles around a circular 'scar'. The analytical model has an advantage over the finite element model in that results can be generated very quickly. Finite element analyses in this study typically took seven to ten hours to run on a 1.6 GHz Centrino PC. If mass-scaling techniques were not employed, analyses would have taken days to run. However, the finite element model more closely replicates the experimental results than does the analytical model in terms of the number, amplitude and length of wrinkles. A major limitation of the analytical model is the small strain assumption. The finite element models also have the potential to analyse wrinkling in scenarios involving anisotropic materials under more complex tension distributions. Indeed, the finite element models could provide a means of simulating scenarios that are difficult to perform experimentally.

5.3 Modelling the behaviour of skin around a contracting 'scar'

The study of Section 5.2 has shown it is possible to model the wrinkling of isotropic elastomer materials, such as latex with reasonable accuracy using the finite element method. Reasonable results can also be obtained with a relatively simplistic analytical model. However, it is likely that the results of similar test on a complex material such as biological skin would be very different to latex. The next development of the study was to carry out experimental tests similar to Geminard *et al.* (2004) but to use biological skin in place of the latex elastomer. The experimental results could then be used to validate finite element analyses of similar scenarios.

5.3.1 Material and Methods

Laboratory experiment

The experimental set-up consisted of a square plate measuring 300 x 300 mm and raised 200 mm by supports at each corner shown in Figure 5.11 and Figure 5.12. A 10 mm radius hole was located in the centre of the plate. The edge of the hole and the four edges of the plate were raised 10 mm above the rest of the plate. This was done in order to minimise the friction between the skin and the plate.

Goat skin was used for the experiment, due to its availability and its look and feel,
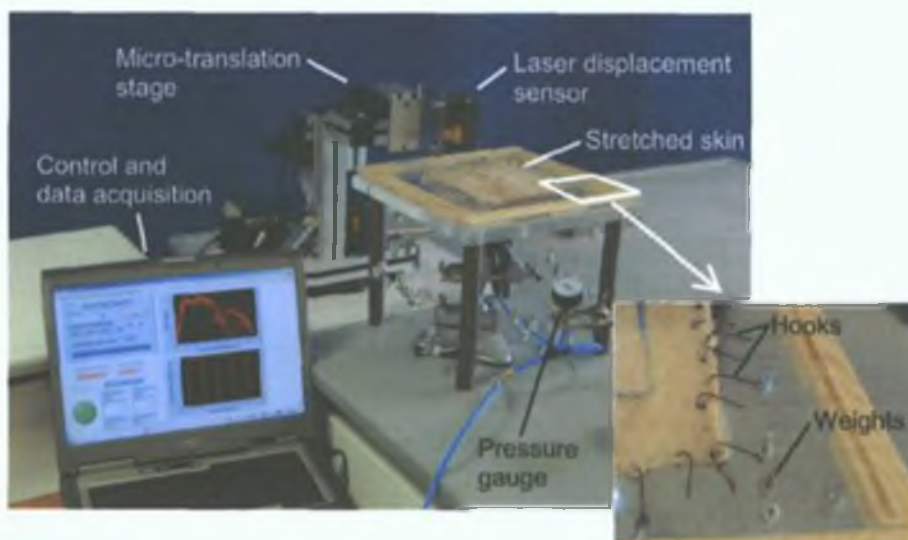
Figure 5.11: Experimental rig with skin biaxially stretched on the supporting frame
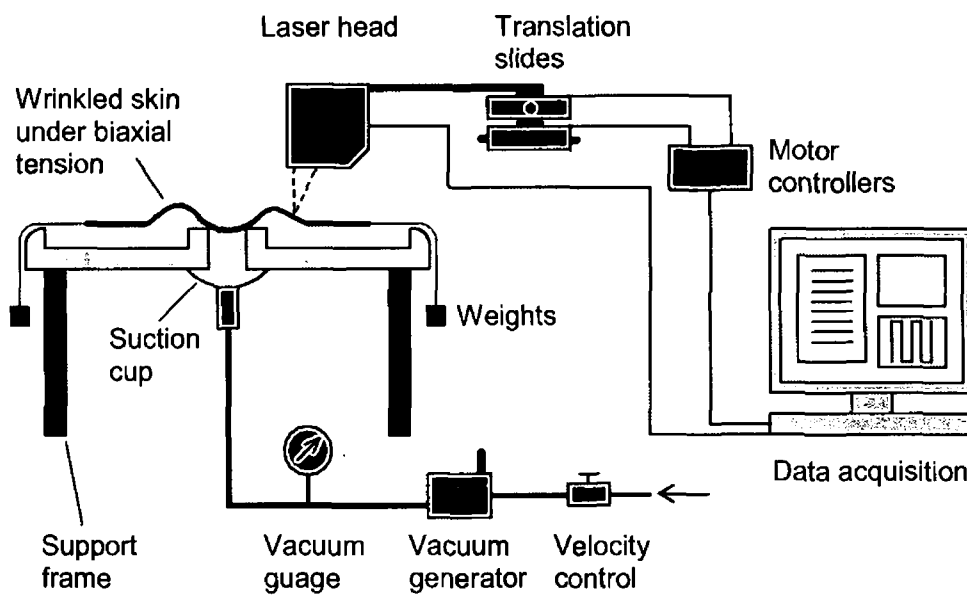
Figure 5.12: Schematic of experimental rig

which was similar to human skin. The excised skin was shaved and cut into approximately square samples of side 150 mm. The orientation of each skin sample with respect to the body was recorded. The samples were frozen until required for testing. Frozen storage has been reported as having a negligible effect on the mechanical properties of soft tissue (Foutz *et al.*, cited in Wu *et al.* (2006a)).

Holes were punched uniformly along the sides of the sample and a fishing line was attached to each hole by means of a hook. Each line ran over the rounded edge of the plate to a suspended weight, thus applying a biaxial tension to the skin sample. The tension applied by each weight was varied between 0.06 N to 0.3 N. While it was assumed that there was a constant tension applied along each side of the sample, in reality there may have been some variation. This variation may arise due to friction between the fishing line and the edge of the support plate, differences in the connection between the hooks and the skin or local differences in the skin thickness.

A suction cup (Festo Type VAS-30-1/8-PUR) was located underneath the hole on the underside of the plate. The cup was connected to a vacuum generator (Festo Type VAD-M5). The level of the vacuum was controlled by a flow-control valve and the pressure in the vacuum was measured using a vacuum gauge. As the pressure was reduced, the skin was drawn into the hole and wrinkles spread radially outwards. The pressure in the hole underneath the skin was varied from -0.1 to -0.5 Bar depending on the skin sample and the applied tension.

The profiles of the wrinkles were measured using the laser profilometer system described earlier in Chapter 4. For this experiment, there were two micro-translation slides, arranged one on top of the other. With this arrangement, the laser head could be moved in two orthogonal directions and a 15 x 15 mm square could be measured. It was necessary to devise a system to measure a larger area. The profilometer was placed upon 5 mm grid paper. For each pressure and tension setting, the laser head was located above the centre of the hole and a 15 x 15 mm square was measured and recorded. Upon completion, the profilometer was moved 15 mm on the grid paper and another 15 x 15 mm square was measured. The data from each 15 x 15 mm grid could then be joined together to give the skin profile over a larger area. The time taken to profile an area of dimension 30 x 30 mm was approximately 20 to 25 minutes.

Two different experimental procedures were carried out. The first involved stretching the skin at a constant tension of 5.7 N/m and reducing the pressure in the hole underneath the skin from -0.1 to -0.5 Bar. The second procedure involved keeping the pressure in the hole constant at -0.5 Bar and reducing the applied tension to the skin. The applied tensions in the second procedure were 18.4, 12.1, 9.2, 5.7 and 2.9 N/m. There were few values of *in vivo* pre-tension in human skin reported in the literature. Alexander and Cook (1977) measured pre-tensions varying from 5 N/m to 24 N/m in the upper back of a male volunteer.

The skin profile data was processed. The maximum range and length of each wrinkle was calculated. The maximum range of a wrinkle was defined as the greatest vertical distance between a point on the crest of the wrinkle and a point at the same radius on the bottom of an adjacent valley. At each applied pressure and tension, the mean and standard deviation of the maximum range and length of the measured wrinkles were calculated. The orientation of the wrinkles was also observed at each applied pressure and tension.

Finite element analysis

The finite element model developed was similar to that developed in Section 5.2.1 to model the wrinkling of the latex membrane and is shown in Figure 5.13. As before, only one-quarter of the domain was modelled, assuming the problem to be symmetrical. The skin sample in the one-quarter model measured 75 x 75 x 1.4 mm. Symmetrical boundary conditions were placed along the appropriate sides.
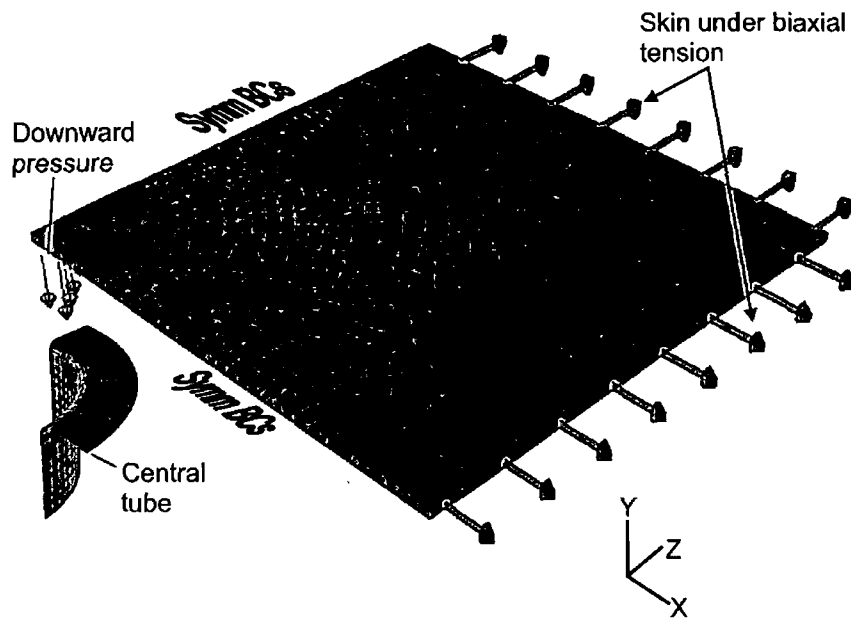
Figure 5.13: Finite element model of skin: One quarter of skin is modelled; Skin is meshed using approximately 30000 eight-noded brick elements (C3D8R); Biaxial stress applied to edge during first step; Downward pressure applied smoothly over the inside area of the tube during second step.

Approximately 30000 eight-noded brick elements were used in the skin mesh with the density highest in the region of the edge of the hole. There were four elements across the thickness of the skin. The central tube was generated as a discrete rigid body and was meshed with 350 four-noded rigid elements.

The hypodermis was ignored in the model because it was not present in the skin samples used in the experiment. There were some difficulties applying pre-stress to the skin model with the stiff stratum corneum layer in place. It was found that an excessively high vacuum pressure was required to pull the skin into the hole. While acknowledging the importance of the stratum corneum from the previous chapter, it was decided to ignore the contribution of this layer in this initial development of the 'scar' model. It is still a significant development over other scar contraction models developed by Geminard *et al.* (2004) and Cerda (2005) in that the orthotropy of the skin is taken into account. The model used the orthotropic-viscoelastic constitutive equation developed in Section 3.3.1. The material parameters chosen were those generated for the stress relaxation tests of human skin and are shown in Figure 3.11.

105

It was assumed that goat skin was similar to most mammalian skin and was almost incompressible. Human skin has density of about 1100 kg/m^3 (Leider and Buncke, 1954) and it was assumed goat skin has a similar density.

The analysis procedure was similar to the procedure for the latex membrane analyses. For the first step, a biaxial tension was applied smoothly to the skin over a period of 5 seconds. The biaxial tensions applied in the model were 1.4, 2.1, 2.8, 5.6 and 9.1 N/m. In the second step, a downward pressure was applied over an area slightly smaller than the cross-sectional area of the tube. The time-period of the second step was 15 seconds. Mass-scaling was used in order to reduce the computational time of the analyses. The density was increased by a factor of 100.

The time period of the second step in the finite element analysis was 15 seconds and was a small fraction of the time period of the experiments, which were between one and two hours. The CPU time required to solve an analysis with a time period of two hours would be on the order of weeks, even if mass-scaling techniques were used.

The orientation, the mean of the maximum range and mean length of the wrinkles in the finite element analyses were recorded and compared with the experimental data.

The biaxial tension in the model was applied continuously along each edge of the skin, whereas in the experiments, the tension was applied at discrete points along the edges. Applying the tension at discrete points results in a heterogeneous stress field in the region of the attachment points. The extent of this heterogeneous stress field was investigated by simulating the biaxially stretching of the skin using discrete attachment points as per the experimental protocol. Point loads of 0.02625 N were applied at six points along each edge. This is equivalent to a biaxial tension 2.1 N/m. The loads were applied smoothly over 5 seconds. Figure 5.14(a) and Figure 5.14(b) shows the E_{11} and E_{22} strain fields, respectively, after the point loads were applied. Away from the attachment points, the strain fields are almost homogeneous. The area of maximum homogeneity (the bottom left section of the model) corresponds to the area of interest where the wrinkles form around the contracting scar. The stress field in this region was also found to be very homogeneous. In this region, the stress in the X direction was 1.4 kPa and in the Z direction was 1.3 kPa. These stresses are slightly lower than the 1.5 kPa stress field obtained when the loads are applied continuously along each edge of the skin.

It can be concluded that although there are stress and strain inhomogeneities in the region of the discrete attachment points, the dimensions of the skin sample being

(a)
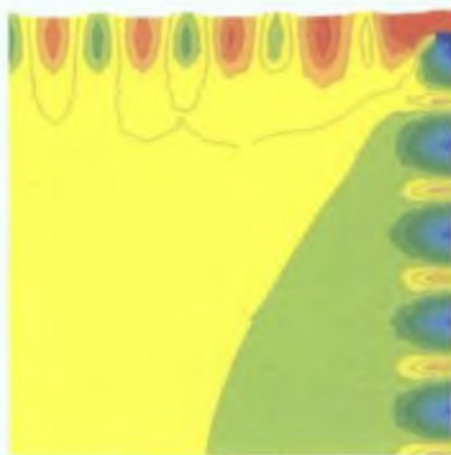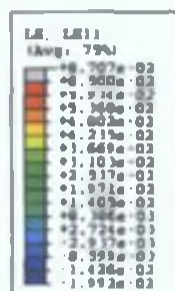
(b)
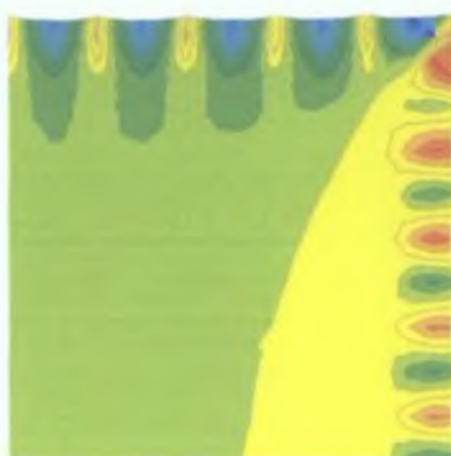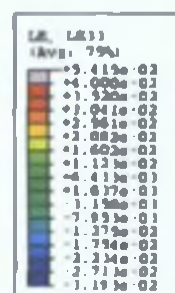
Figure 5.14: (a) E_{11} and (b) E_{33} strain fields after skin model is biaxially stretched by applying loads at discrete points along edges. The strain field is mostly homogeneous except for the areas around each load point.

modelled are large enough such that the area of interest lies in a sufficiently homogeneous stress and strain region. Therefore, simulating the laboratory experiment with continuously applied loads along the edges is a valid approach.

5.3.2 Results

Wrinkle orientation

A typical wrinkle formation around a contracting 'scar' in real skin is shown in Figure 5.15(a). When each side of the skin sample was under equal tension, it was observed that the wrinkles had a preferential orientation that corresponded to a direction perpendicular to the Langer's Lines in the skin sample. This characteristic was also observed in the finite element models. Figure 5.15(b) shows contours of wrinkle heights around a contracting 'scar' for an orthotropic skin model under an

(a) Real skin
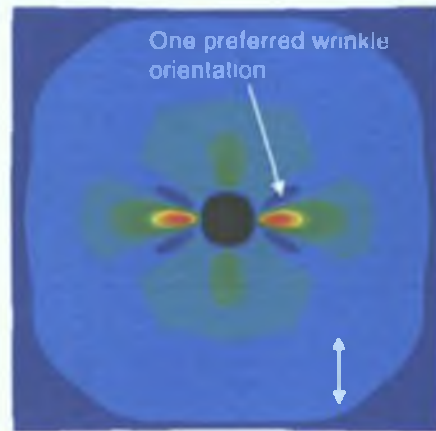
(b) Orthotropic skin model

Figure 5.15: The effect of material orthotropy on the wrinkling behaviour of skin around 'scars': (a) Wrinkles formed around a contracting 'scar' in real skin under an equibiaxial tension of 3.1 N/m; (b) and (c) Height contours for wrinkles around contracting 'scars' for orthotropic and isotropic skin models, respectively, under an equibiaxial tension of 2.8 N/m; For (a) and (b) the wrinkles have one preferred orientation, which is perpendicular to the Langer's lines (indicated by the arrows); for an isotropic material (c) there is more than one dominant wrinkle orientation
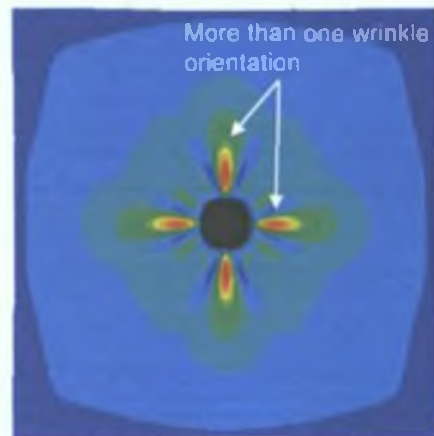
(c) Isotropic skin model

equibiaxial tension of 2.8 N/m. The wrinkles formed in the model also had a preferred orientation corresponding to a direction perpendicular to the Langer's Lines. Figure 5.15(c) shows the pattern formed for an isotropic material. For this material, the model parameters were such that its stress-strain response was similar to the orthotropic skin model in the stiffer direction. In this isotropic case, there was no single preferred wrinkle orientation.

In the experiments, the preferred wrinkle orientation was more noticeable when the skin was under higher tensions. Figure 5.16(a) shows the wrinkle pattern around a contracting 'scar' when the skin was under a biaxial tension of 2.9 N/m. The wrinkles were more uniformly distributed around the 'scar'. As the biaxial tension increased to 12.1 N/m, one large wrinkle dominated (Figure 5.16(b)). This wrinkle was orientated in a direction perpendicular to the Langer's Lines. A similar trend was observed in the skin models. Figure 5.16(c) and Figure 5.16(d) shows the wrinkle pattern formed

(a) Experiment: Biaxial tension 2.9 N/m (b) Experiment: Biaxial tension 12.1 N/m

(c) Model: Biaxial tension 0.0 N/m (d) Model: Biaxial tension 5.7 N/m
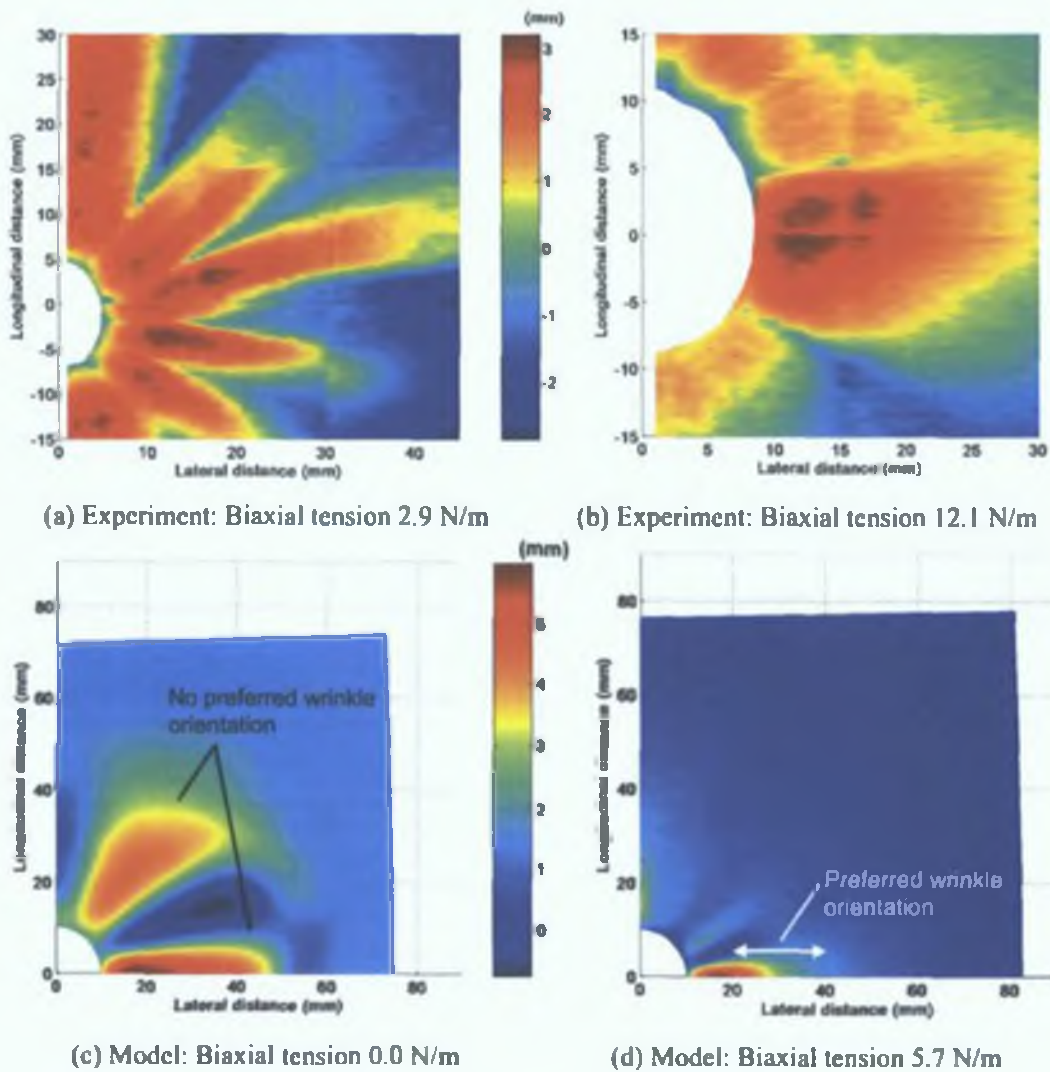
Figure 5.16: Contour plots showing the heights of the wrinkles around the circular 'scar' from a typical experiment and models. For the experimental result, the pressure in the hole underneath the skin is -0.5 Bar, while for the model, the pressure in the hole underneath the skin is -0.075 Bar. For all contour plots, the Langer's Lines lie approximately in the longitudinal direction.

when there was a pre-stress of 0.0 N/m and 5.7 N/m, respectively. Although, there was a slight preferred wrinkle orientation for the case of zero pre-stress, it was a more uniform pattern than the distribution obtained for the 5.7 N/m case.

This behaviour may be attributable to the orthotropic characteristics of the material. In Figure 5.16(d), the stiffness of the skin in the longitudinal-direction is greater than the stiffness in the lateral-direction. Therefore, as the 'scar' contracts, skin in the longitudinal-direction cannot stretch to the same extent as skin in the lateral-direction. Instead, the top edge of the skin model in Figure 5.16(d) displaces inwards to a greater extent than the right edge, causing the wrinkles to form

predominantly in the lateral-direction. When an isotropic material model was used to simulate the experiment, the resulting wrinkles were evenly distributed around the 'scar' (Figure 5.15(c)). There was no preferential orientation as observed in the experiment.

Varying pressure

Figure 5.17(a) shows the mean of the maximum ranges of the wrinkles measured in the experiments as the vacuum pressure was decreased. The skin samples were under

(a)

(b)
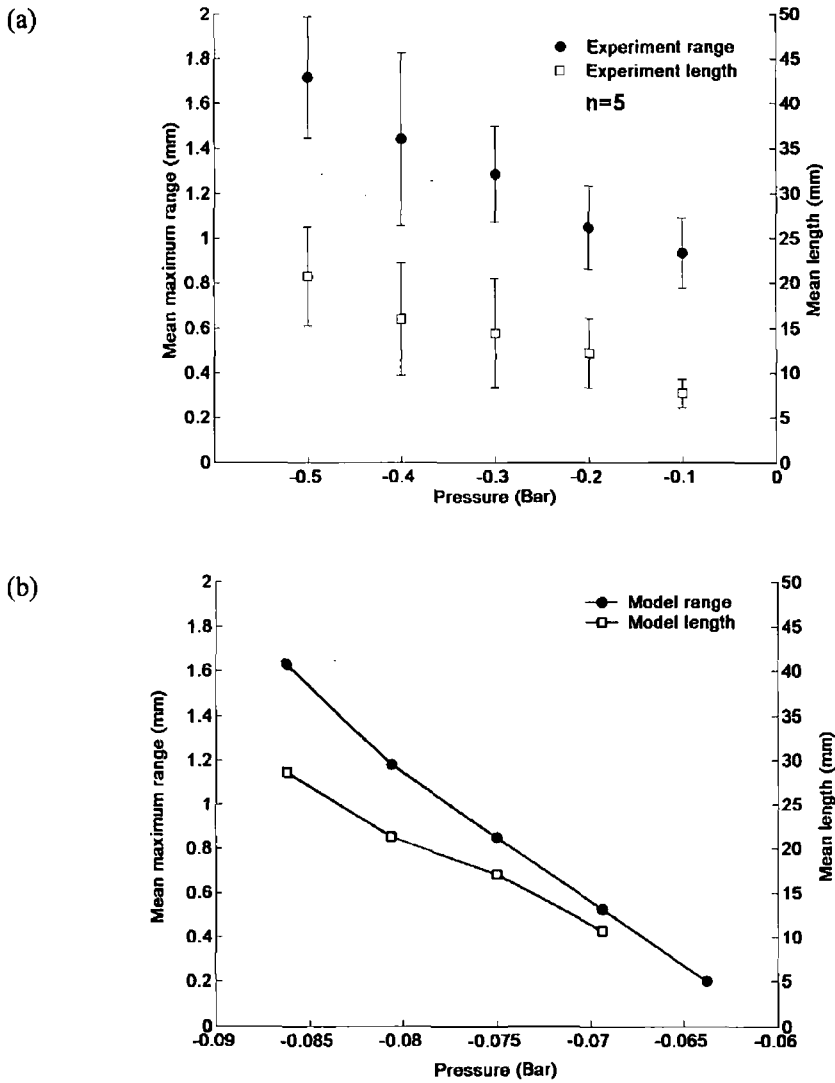
Figure 5.17: (a) Experimental mean value and standard deviation of the maximum range and length of each wrinkle as a function of the pressure in the hole underneath the skin; (b) Mean maximum range and mean length predicted by the finite element model. For the experiment and model, the applied tension along each side of the skin was 5.7 N/m.

a biaxial tension of 5.7 N/m. As the vacuum pressure decreased from -0.1 to -0.5 Bar, the maximum ranges of the wrinkles increased in an almost linear fashion from an average of 1 to 1.75 mm. The length of the wrinkles increased almost linearly from an average of 10 to 21 mm, as also shown in Figure 5.17(a).

The maximum range and mean length predicted by the finite element models are shown in Figure 5.17(b). The change of both the range and the length with pressure was almost linear as measured in the experiments. Both the magnitudes of the wrinkle range and lengths were comparable with the experiment. However, the vacuum pressures in the model were much smaller than the pressures applied in the experiments. They ranged from -0.06 to -0.09 Bar in the model compared to -0.1 to -0.5 Bar in the experiments.

Varying tension

When the vacuum pressure in the experiments was held constant at -0.5 Bar and the biaxial tension was increased, both the wrinkle range and length decreased non-linearly. The maximum range decreased from 2.86 to 0.85 mm when the tension increased from 2.9 to 18.4 N/m (Figure 5.18(a)). The length decreased from an average of 36 to 8 mm when the tension was increased from 2.9 to 18.4 N/m (Figure 5.18(b)).

For the models, the wrinkle range decreased non-linearly from 5.9 to 0.2 mm when the biaxial-tension in the skin was increased from 1.4 to 9.1 N/m as shown in Figure 5.18(a). There was a corresponding non-linear decrease in the predicted wrinkle length from 60 to 5 mm as shown in Figure 5.18(b). The vacuum pressure in the hole underneath the skin models was much lower than the vacuum pressure in the experiment at -0.075 Bar.

5.4 Summary

An analytical model and finite element model were developed to simulate a simplified experimental model of a contracting scar in the literature. While the numbers of wrinkles predicted by the models were significantly larger than the numbers observed in the experiments, they correctly predicted an increasing number when the tension in the membrane increased and the initial 'scar' radius increased. The predicted amplitudes of the wrinkles in the finite element models differed by 12
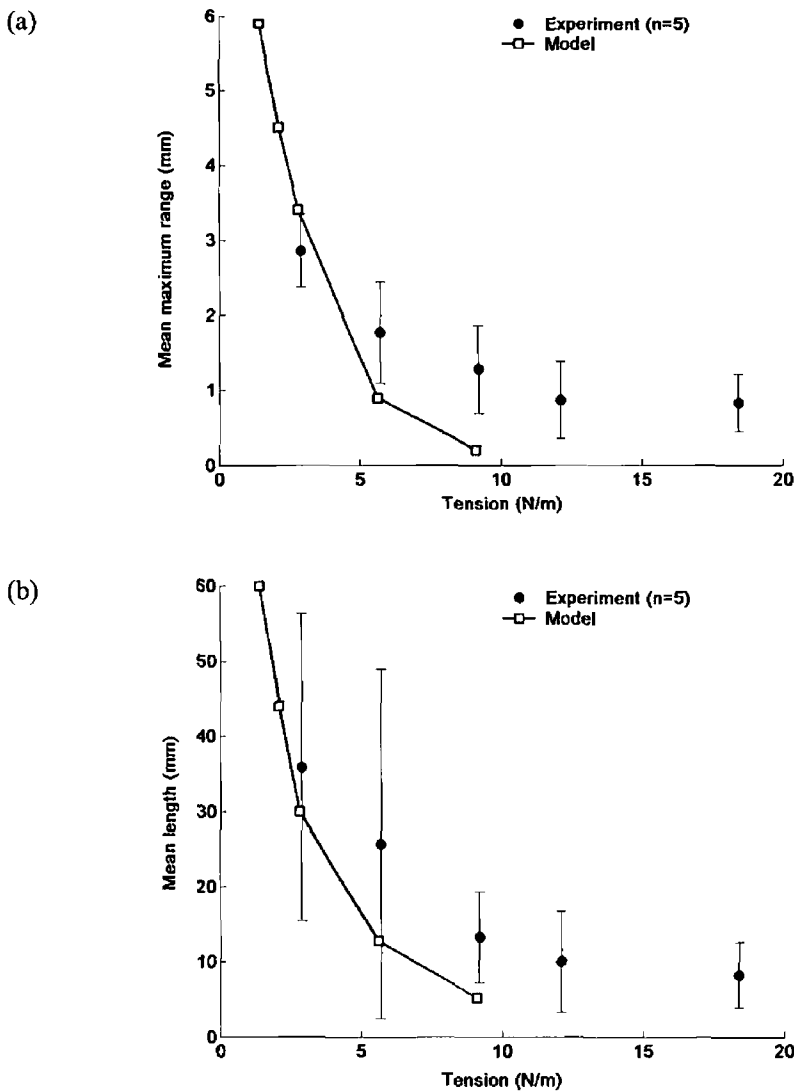
Figure 5.18: The mean value and standard deviation of the (a) maximum range and (b) length of each measured wrinkle as a function of the applied tension along each side of the skin sample. The experimental pressure in the hole underneath the goat skin is -0.5 Bar. In the models, the pressure in the hole underneath the skin is -0.075 Bar.

to 42% from the amplitudes measured in experiment. The predicted analytical model amplitudes differed by 15 to 24% from the experimental amplitudes.

The finite element model was developed further with a single-layer orthotropic-viscoelastic model of skin substituted in place of the latex membrane model. The 'scar' contraction model in skin was compared with experiments measuring the wrinkles that formed around a contracting 'scar' in goat skin. Both the experiments and models showed that, when the skin is under an equibiaxial tension, the direction of the resulting wrinkles will be strongly influenced by the relative orientation of the

112

Langer's Lines. This characteristic cannot be simulated with an isotropic material model. Both the experiment and model showed a linear increase in wrinkle range and length with increasing vacuum pressure. They both also showed a non-linear decrease in the wrinkle range and length when the skin tension was increased.

Chapter 6

Discussion

Skin forms the outermost layer of the human body and, because of its high visibility and importance, it has been studied in many areas of science and technology such as biomechanics, medicine, forensics, cosmetology and computer animation. Much of this effort has been in the development of mathematical and computer models of human skin. The complexity and quality of these models have evolved significantly over the last few decades. There are several skin models that can simulate accurately the non-linear, orthotropic and viscoelastic characteristics of skin measured in various *in vivo* and *in vitro* experiments. Most of these models, however, assume skin to be a homogenous material and thus ignore the individual contribution of each layer. While it may be justified to use single-layer skin models to simulate homogeneous uniaxial and biaxial stretch tests, it is argued that a multi-layer model of skin more accurately simulates complex deformations such as skin wrinkling.

The aim of this thesis was to develop a more realistic model of the mechanical behaviour of skin when subjected to loads and deformations that cause it to wrinkle. A model such as this, where the properties of each layer are specified, would be of benefit in numerous areas including the study of skin aging; the development of cosmetic treatments; the design of more realistic artificial skin; more realistic computer animation; and the development of surgical techniques.

It was hypothesised that in order to accurately simulate the wrinkling of skin, it is necessary to have a multi-layer model representing the epidermis, dermis and hypodermis. To support this hypothesis, several objectives were accomplished, the first of which was the development of a multi-layer model with constitutive equations specified for each of the three layers.

The stratum corneum was represented by the neo-Hookean hyperelastic function. The non-linear portion of the stress-strain curve in Figure 3.1 was ignored because it occurred over a very small strain-range (less than ~1%). Viscoelastic effects were also ignored. Yuan *et al.* (2006) demonstrated that stratum corneum has viscoelastic properties but the applied loads and indentations used in the tests were in the nanoscale region. The loads and strains of that experiment were several orders of magnitude smaller than the loads and strains of interest in the current study.

The orthotropic-viscoelastic model for the dermis was tested by evaluating its ability to model a broad range of experiments in the literature. The model matched, accurately (to within 7.6%), the response of rabbit skin undergoing uniaxial and biaxial deformation using the one set of material parameters. The location of the locking region followed that of the experimental results whether the force was applied along the length or width of the body. The model therefore successfully captured the orthotropic nature of the rabbit skin. The level of hysteresis also closely simulated the experimental results for all tests. A better fit with the experimental data may be obtained if the extension rate used in the experiment and the thickness of the skin samples were known more precisely. The percentage error of the orthotropic-viscoelastic model when simulating the rabbit tests was significantly lower than the Bergstrom and Boyce model (2001) (13.8% error) and the orthotropic model of Bischoff *et al.* (2002) (19.5% error). It should also be noted that the Bergstrom and Boyce model (2001) is isotropic and so can only predict the response of the rabbit skin for one orientation only. The orthotropic model of Bischoff *et al.* (2002) is purely hyperelastic and so obviously cannot capture any of the viscoelastic properties. As a result it would not be able to simulate stress relaxation tests such as those of Wan Abas (1994). The orthotropic-viscoelastic model presented in this thesis simulated the stress relaxation of human skin to within 1% as seen in Figure 3.12.

Lanir and Fung (1974) did not explicitly state that the rabbit skin experimental data in Figure 3.7 was preconditioned. For the model with the material parameters in Figure 3.7, it was assumed not to be preconditioned. When this model was subjected to multiple loading and unloading cycles, the load-stretch curves changed and became more compliant until they converged after about seven cycles. When it was assumed that the experimental data in Figure 3.7 was preconditioned, the material parameters had to be changed significantly in order to simulate the test. In conclusion, when

simulating experimental tests in the literature, it is important to take into account whether the specimens were preconditioned prior to testing or not.

The orthotropic-viscoelastic model reproduced the human skin experiments of Schneider (1982) to a higher accuracy (10.8% error) than did the Shoemaker *et al.* (1986) model (13.0% error) as seen in Figure 3.11(a) and Figure 3.11(b). The response of the new model at the 'elbow' region was less abrupt than the Shoemaker *et al.* (1986) model and matched the experiment well.

When simulating the tensile tests of pig-skin (Ankersen *et al.*, 1999), the quality of the fit was not as good as when simulating the rabbit skin or human skin experiments (Figure 3.13). The nominal stress predicted by the model when the pig-skin was loaded perpendicular to the spine was much higher than the experiment at low stretches. It was noted that the locking region occurred at a very low stretch of about 1.05 when the skin was loaded parallel to the spine, while there was no significant stress in the specimen until stretches of 1.5 when loaded transversely. This behaviour probably contributed to the difficulty in fitting the model closely to the experimental data. It is speculated here that perhaps there were wrinkles in the pigskin in the longitudinal direction. When the skin was stretched transversely, these wrinkles first flattened before any stress developed in the skin. Despite the difficulties, the orthotropic-viscoelastic model was significantly better than the Ogden model that Shergold *et al.* (2006) used to simulate the experiment.

The compression tests of pig-skin were simulated accurately by the orthotropic viscoelastic model (18.4% error) as shown in Figure 3.14. The one set of material parameters could simulate two tests carried out at strain-rates differing by a factor of 100. Shergold *et al.* (2006) used the Ogden model to simulate the experiments. Of course, they had to use a different set of material parameters for each strain-rate.

The orthotropic-viscoelastic model matched the compression test data of monkey liver (Miller, 2000) as well as the Bergstrom-Boyce model (2001) (Figure 3.13 and Table 3.5). This demonstrates that the model is capable of replicating experiments carried out at a wide range of strain-rates and on other soft tissues.

A source of inaccuracy in the orthotropic-viscoelastic model is the probability that there are further mechanisms for viscoelasticity in addition to the reptation of the fibres within the ground substance, such as molecular motion within each collagen fibril (Fyhrie and Barone, 2003). Another source of inaccuracy is not modelling

116

explicitly the fluid in the ground substance as a second phase as was done in the cartilage model of Mow *et al.* (1980).

Another limitation of the orthotropic-viscoelastic model is that it contains more parameters than the other models (12 as compared with 5 for the Bischoff *et al.* (2002) model, and 9 for the Bergstrom and Boyce (2001) and Shoemaker *et al.* (1986) models). The goal of any constitutive model would be to accurately capture the various properties with as few parameters as possible. Bischoff *et al.* (2004) effectively reduced the number of parameters of the orthotropic-viscoelastic model to eight by, among other things, restricting the dimensions of the unit cells of each network – (a_A, b_A, c_A) and (a_B, b_B, c_B) – to be equal to each other. They fitted the model to a biaxial stretch test of rabbit skin (Lanir and Fung, 1974) with an error of about 30% and R^2 of 0.79. This compares to an error of 7.6% and R^2 of 0.975 (Table 3.2) when the model was fitted simultaneously to uniaxial and biaxial stretch tests of rabbit skin and the material parameters were not restricted. Therefore, the parameter reduction comes at the expense of accuracy of fit.

Recently, Bischoff (2006) proposed a seven-parameter model for soft tissues that is capable of simulating anisotropic and viscoelastic effects. The model contains the orthotropic unit cell of previous models (Bischoff *et al.*, 2002; 2004) but viscoelasticity is incorporated at the fibre level using the theory of quasi-linear viscoelasticity (QLV) (Fung, 1993). The model simulated various stress relaxation tests of porcine skin to a high accuracy (1.3 % error of fit). The model does not account for the viscoelasticity due to relative motion between the collagen fibres and ground substance. Representing viscoelasticity in soft tissues such as skin as quasi-linear is only an abstraction. Modelling the strain-rate dependency of soft tissues using the QLV theory is problematic (Fung, 1993). Despite these shortcomings, this approach does offer good potential for an orthotropic-viscoelastic model with minimal number of material parameters.

The material parameters of the dermis model should be physically meaningful and, ideally, it should be possible to obtain their numeric values from experimental tests. Bischoff *et al.* (2001) demonstrated a method to calculate the dimensions of the unit cell (*a, b, c*) for their orthotropic model (Bischoff *et al.*, 2002) by examining SEM images of heart tissue. This method would be significantly more difficult when calculating the unit cell dimensions of both networks in the present orthotropic-viscoelastic model – (a_A, b_A, c_A) and (a_B, b_B, c_B). With regard to n_A and n_B, which both

represent the collagen fibre density of the dermis, there were few reported values of the fibre density in the literature. Sanders and Goldstein (2001) counted the number of collagen fibrils per cross-sectional area in the dermis to be on the order of 1×10^{14} m^{-2}. While there are difficulties getting collagen fibre densities from experimental examinations of skin, the parameters n_A and n_B are physically meaningful in the sense that increasing either of them leads to a predictable increase in the stiffness of the skin as was shown in Figure 3.10. The viscoelastic parameters C_1, C_2 and m are less physically meaningful in the sense that there is no clear means of measuring their values experimentally. Trial and error would be the best method to find their values for a particular skin sample.

The hypodermis model simulated accurately a number of compressive and stress relaxation tests from the literature at different strain-rates. The error between the model predictions and the experimental results ranged from 6 to 29% (Figure 3.16, Figure 3.17 and Figure 3.18). The model for this layer consisted of the hyperelastic Yeoh strain energy function and a two-term Prony series to simulate the viscoelastic characteristics of the hypodermis. This model represents an improvement over other models, which assumed the hypodermis or subcutaneous tissue to be purely linear elastic (Dandekar *et al.*, 2003; Gerling and Thomas, 2003).

The first objective of developing a multi-layer model of skin was achieved and the second objective of evaluating the model was partially completed with the testing of the individual layers against experimental results in the literature. The next stage was to complete the second objective by evaluating the multi-layer model against *in vivo* wrinkling experiments conducted in this study.

For the first time, a multi-layer finite element model of skin has been developed to simulate the wrinkling of skin under compression and the results of the model have been validated against *in vivo* experiments. The quantitative comparison of the finite element model results with the experimental results is a significant improvement over the work of Magnenat-Thalmann *et al.* (2002), where only some qualitative comparisons were made between their simpler two-dimensional model and real wrinkling skin.

The study has shown the importance of accounting for the individual layers of the skin when simulating wrinkling under compression. In single-layer models, no wrinkles form under skin compression. In order to simulate the wrinkling in this study, a model consisting of at least a layer representing the stratum corneum and a layer

representing the dermis is necessary. While the single-layer models of Lanir (1983), Shoemaker *et al.* (1986) and Bischoff *et al.* (2004) simulate accurately the behaviour of skin in biaxial stretch and stress relaxation tests, they are unable to simulate more complex deformations such as skin wrinkling. Therefore, the proposed multi-layer model represents a considerable advancement over existing single-layer models.

In addition to the necessity of accounting for the stratum corneum and dermis in a skin model, the study has demonstrated the importance of accounting for the hypodermis beneath the skin. In the two-layer model consisting only of the stratum corneum and dermis, the trends of the predicted maximum range and average roughness of the wrinkles did not follow the trends observed in the experiments at larger skin compressions. This result would suggest that an additional layer is required beneath the dermis. The proposed three-layer model was an improvement over the two-layer model because it was able to simulate the wrinkling of skin over a larger range of compressions. The proposed model is also, therefore, superior to other skin wrinkling models in the literature. While the model proposed by Magnenat-Thalmann *et al.* (2002) contained layers representing the stratum corneum and dermis, it ignored the hypodermis. The proposed three-layer model would make more realistic predictions of the wrinkles at greater skin compressions than their model.

The overall improvement of the three-layer model results over the other models support the primary hypothesis that a multi-layer model representing the stratum corneum, dermis and hypodermis is necessary to accurately simulate the wrinkling of skin. The usefulness of the model can now be demonstrated by showing how it can predict the changes in the wrinkles when various properties of the skin are adjusted.

The finite element analyses showed that an increasing pre-stress in the skin delays the initiation of wrinkles. It also decreased both the maximum range and average roughness of the wrinkles for a given skin compression. While this result is not unexpected, its demonstration in the context of a skin wrinkling model is novel and provides support to the hypothesis that inclusion of pre-stress or natural tension in a skin model is important. Wrinkles in skin increase with age and one cause for this is the loss of the natural tension in skin (Pierard *et al.*, 2003). By explicitly accounting for the pre-stress, the proposed three-layer model for skin is better able to simulate the aging of skin due to the loss of natural tension than other multi-layer models of skin such as those developed by Hendriks (2005) or Magnenat-Thalmann *et al.* (2002).

The strength of the proposed model in simulating aging skin is further demonstrated by the results from the parameter study. It was shown that the size of the wrinkles in the model was dependent on the hydration level of the stratum corneum – the greater the hydration level, the smaller the wrinkles (Figure 4.17). This phenomenon is also observed in real skin. When real skin ages, the stratum corneum becomes drier and stiffer resulting in larger wrinkles (Batisse *et al.*, 2002). This result also demonstrates the motivation for the use of moisturisers in skin care. The moisturisers hydrate or prevent water-loss from the stratum corneum, thus lowering its stiffness and reducing the appearance of wrinkles (Magnenat-Thalmann *et al.*, 2002; Sivamani *et al.*, 2003).

It has been observed that the collagen fibre density increases with age (Lavker *et al.* cited in Silver *et al.* (2001)). Batisse *et al.* (2002) measured the mechanical properties of human skin *in vivo* and found the whole dermis to be stiffer in aged skin. Increasing the collagen fibre density parameters, n_A and n_B, in the orthotropic-viscoelastic model of the dermis resulted in a stiffer layer, which in turn led to larger wrinkles forming when the tab displaced (Figure 4.18). Therefore, changing the mechanical properties of the dermis in the model in accordance to what is observed in real aging skin results in the prediction of larger wrinkles.

The finite element analyses showed that the size of the wrinkles were dependent on their orientation relative to the Langer's lines. When there was an equibiaxial pre-stress, the wrinkles were largest when perpendicular to the Langer's lines. When the pre-stress parallel to the Langer's lines was larger than the pre-stress perpendicular to them, the wrinkles were largest when parallel to the Langer's lines. This is what is observed when one pinches themselves – wrinkles are larger when they form parallel to the Langer's lines (Borges, 1989). This result further supports the hypothesis that a realistic pre-stress is necessary in a model when simulating wrinkling.

The ability of the proposed multi-layer model to predict realistic changes in the wrinkles when different properties of the skin are used clearly demonstrates its advantages over other existing models. Single-layer models cannot predict changes in wrinkles when the stratum corneum stiffens. Models that do not consider the natural tension or pre-stress in skin cannot make meaningful predictions of the wrinkling behaviour when that pre-stress changes. Isotropic models cannot take into account the effect of the directionality of skin on the wrinkling behaviour. The proposed multi-layer model has demonstrated its capacity to take all these factors into account.

A source of uncertainty in the experiments is the large standard deviation at greater tab displacements. This shows a degree of variability between the volunteers as the wrinkles develop. There could be many reasons for this variability between the volunteers, such as age, gender, moisture content of the stratum corneum, the thickness of the hypodermis or the physical size of the forearm. Increasing the number of volunteers in the study may reduce the standard deviation at the higher tab displacements.

Unlike real skin, there is no wrinkling in the finite element model until there is a critical compression in the skin. This is due to the assumption of a perfectly smooth surface for the stratum corneum. The addition of an initial surface roughness to the stratum corneum layer (representing the actual unloaded surface texture of skin) would result in non-zero maximum ranges and average roughnesses at zero compression as observed in real skin. Better agreement may then be observed between the experimental and finite element results.

Another source of error in the finite element models is the selection of the material parameters for each skin layer. The parameters were chosen so that each individual layer matched experimental results in the literature carried out on an individual layer. A development of the experiment and model would be to carry out *in vivo* stretch or compression tests on each volunteer in addition to the wrinkling tests. Volunteer-specific material parameters could then be generated to fit the constitutive model of each layer to the stress-strain response of each volunteer. Simulating the wrinkling of skin using multi-layer models specified for each volunteer may account for the variability of the wrinkles observed in the *in vivo* experiments.

The third and final objective was to apply the model to the case-study of a healing scar. The purpose of this work was to explore wrinkle formation around a contracting scar. Experiments of a simplified model of a contracting scar were developed. The amplitude, length and orientation of the wrinkles that formed around the 'scar' were compared to finite element models of the same experiments. As discussed in Chapter 5, there were difficulties in using the multi-layer model of skin for the simulations so a single-layer version was used as a first step in the development. Despite the simplification, the comparison of the finite element model to experiments on real skin is a significant development over the work of Geminard *et al.* (2004) and Cerda (2005). They used latex and polyethylene membranes, respectively, in place of real skin in their experimental models of contracting scars. Therefore, those models are

unable to account for the influence of the orthotropy of the skin on the behaviour of the wrinkles. The orthotropic property of the proposed skin model in this study correctly predicts the orientation of the wrinkles around the contracting scar observed in the experiment. These results provide support to the hypothesis that it is necessary to account for the material orthotropy in a realistic skin model.

The results from the 'scar' contraction model also provide additional support to the hypothesis of the requirement of a realistic pre-stress in a skin model. Both the experiments and models showed that the natural tension or pre-stress in the skin has the effect of restricting the zone of wrinkling around the scar. The combination of this feature and orthotropy results in a model that can make more meaningful predictions of the behaviour of skin around contracting scars than the Geminard *et al.* (2004) or Cerda (2005) models. The 'scar' contraction model could also be used to analyse the suturing and closure of wounds. The proposed model would be an improvement over previous wound closure models (Lott-Crumpler and Chaudhry, 2001; Retel *et al.*, 2001; Yoshida *et al.*, 2001; Kirby *et al.*, 1998), which do not explicitly take into account the pre-stress in the skin.

In both the experiments and the models, there was an almost linear increase in the maximum range and mean lengths of the wrinkles as the vacuum pressure increased (Figure 5.17). When the tension in the skin was increased, the range and the length of the wrinkles decreased non-linearly in the experiments and models (Figure 5.18). However, the maximum vacuum pressures applied in the finite element analyses were about one-fifth of the vacuum pressures applied in the experiment. One reason for the discrepancy is probably due to the material parameters used for the orthotropic skin model. A series of tensile and compression tests should be carried out on the skin used in the experiments and fit the orthotropic-viscoelastic model to these test results. A biaxial stretch test of the skin would be required at the very minimum. In the finite element analyses, there were also regions where the skin went into compression, particularly near the edge of the hole. With this in mind, compression tests, in a direction perpendicular to the surface of the skin, would need to be carried out. Material parameters could then be generated that would allow the orthotropic-viscoelastic model to simulate this mode of deformation more accurately. Simulating the behaviour of the goat skin under relatively simple homogenous biaxial and compression tests may improve the accuracy of the simulation of more complex deformations such as the wrinkling of skin around a contracting 'scar'.

Many of the reasons for the differences between the latex finite element models and the experiments of Geminard *et al.* (2004) are also the basis of differences between the skin model and experiments in this study. It is unknown how significant the friction was in the experiments. In the present model it was ignored in the contact algorithm between the edge of the hole and the skin. Future models will determine how much of an effect it has on the results.

The skin itself was modelled as a single-layer, where the individual contribution of the stratum corneum was ignored. The role of each of the individual layers of skin on its overall mechanical behaviour was shown in the thesis. There were fewer wrinkles predicted by the finite element model compared to what was observed in the experiment (see Figure 5.16). It was shown in Chapter 4 that the presence of a stratum corneum layer in the model resulted in more wrinkles. It is reasonable to assume that there would be more wrinkles present in the 'scar' contraction model if the stratum corneum was included. Future developments of this model would include a multi-layer representation of skin.

Further differences between the model and the experiment may be due to the discrete attachment of loads and hooks to the skin in the experiment and the continuous distribution of loads along the edges of the skin in the model. It was shown that by applying discrete loads to the skin in the model, there was an almost homogeneous stress and strain-state in the area of interest where wrinkles would form. However, the loads applied at each attachment point in the experiment may not be constant due to friction between the fishing line and support plate or local differences in the skin sample. These factors could contribute to a non-homogeneous stress-state in the region of interest. A more uniform method of applying the load to the skin in the experiment would be needed in future developments.

The experiment analysing the behaviour of skin around a contracting 'scar' is a very simplified model of real scar contraction. Few scars are perfectly circular in shape. The connection of the skin to the underlying layers has been ignored. Skin is also, in general, not in equibiaxial tension. The tension is greatest in the direction of the Langer's lines. The contraction of the 'scar' in the experiments occurred over a time period on the order of minutes. In reality, scars contract over time periods on the order of weeks (Olsen *et al.*, 1995).

Despite these simplifications, the experiments provide a good test for validating a finite element model of scar contraction in skin. The proposed model replicated key

characteristics observed in the experiments, including the decreasing wrinkle range and length with increasing skin tension. Significantly, it is shown that an orthotropic material model is needed to accurately simulate the orientation of the wrinkles around the contracting scar. In conclusion, the simplified experimental and finite element models support the hypotheses that the pre-tension in skin plays an important role in the wrinkling of skin and it is important to include the orthotropic characteristics of skin in the model.

Chapter 7

Conclusions and future work

7.1 Conclusions

A multi-layer model of skin has been developed and validated against both published experimental data and experiments developed in this study. The results from this study provide support to the primary hypothesis that in order to accurately simulate the wrinkling of skin, it is necessary to have a multi-layer model representing the epidermis, dermis and hypodermis. Support was also given to the hypothesis that the pretension in skin is also an important parameter that may have a strong influence on the characteristics of the wrinkles. Specific outcomes of this research include:

1. The stress-strain relationship of the stratum corneum can be represented by the neo-Hookean strain energy function.

2. A wide variety of reported experimental tests on skin can be simulated by an orthotropic-viscoelastic constitutive function. This function can be used to represent the dermis in a multi-layer model of skin.

3. The hypodermis can be represented by the Yeoh hyperelastic function with a two-term Prony series used to model viscoelasticity.

4. A three-layer finite element skin model consisting of the stratum corneum, dermis and hypodermis was found to better simulate the wrinkling of skin between two displacing tabs than either a single-layer or two-layer skin model.

5. It was shown that the natural tension is an important parameter in a skin model – the larger the natural tension, the smaller the wrinkles.

6. Increasing the stiffness of the stratum corneum in the multi-layer model was shown to increase the size of the wrinkle – a phenomenon observed in real aging skin and shows the motivation for the use of cosmetic moisturisers.

7. It was further shown that increasing the density of collagen fibres in the dermis model increases the size of the wrinkle – a result supported by studies in the literature.

8. The maximum range and average roughness of the wrinkles predicted by the finite element model can be related to the variables of the analyses by relatively simple scaling laws:

$$\frac{R_{max}}{\left(B_{sc}/K_H\right)^{1/4}} \sim \left(\frac{\Delta}{W}\right)^{1/2}$$

$$\frac{Avg.\ Roughness}{\left(B_{sc}/K_H\right)^{1/4}} \sim \left(\frac{\Delta}{W}\right)^{1/2}$$

9. A single-layer finite element skin model successfully simulated an in-house experimental model of a contracting scar in real skin. The numerical and experimental models are a significant development over previous contracting scar models, where polymer membranes and linear-elastic isotropic models were used.

10. The orientation of the wrinkles around a contracting 'scar' is strongly influenced by the direction of the skin's Langer's lines. The orthotropic nature of the skin model allowed this phenomenon to be successfully simulated.

7.2 Future work

1. Conduct *in vivo* uniaxial/biaxial experiments on volunteers prior to wrinkling the skin. This would allow the generation of better material parameters for the models used in each layer. An estimation of the pre-stress in the skin may also be possible.

2. Use MRI, ultrasound or other suitable imaging technology to measure thickness of the skin layers of volunteers as well as measure the displacement of each layer while the skin is wrinkled. The interfaces between the skin layers and substrate could also be examined.

3. Improve the stability of the finite element model so that more realistic load boundary conditions can be used on all sides.

4. Extend the skin-tab experiment to measure an area of wrinkles so the length of the wrinkles can be measured as well as the range and roughness.

5. Use a more realistic anatomical shape of the arm in the finite element model.

6. Model the attachment of the hypodermis to underlying layers more realistically.

7. Apply the model to other skin surfaces on the body.

126

8. Remove the assumption of a perfectly smooth skin and model the surface features of stratum corneum.

9. Model the undulating interface between stratum corneum and dermis and investigate whether the flattening of this interface influences the wrinkling behaviour

10. Model the papillary and reticular parts of the dermis separately.

11. Develop the scaling laws for the maximum range and average roughness further to take into account the orthotropic nature of skin.

12. Perform biaxial stretch tests and indentation tests on the *in vitro* skin samples prior to the 'scar' contraction. More accurate material parameters could then be generated for the finite element model.

13. Develop the multi-layer model as applied to simulating 'scar' contraction.

References

Akazaki, S., Nakagawa, H., Kazama, H., Osanai, O., Kawai, M., Takema, Y., Imokawa, G., (2002), Age-related changes in skin wrinkles assessed by a novel three-dimensional morphometric analysis. The British Journal Of Dermatology, 147, 689-695.

Albrecht, I., Haber, J., Seidel, H. P., (2003), Construction and Animation of Anatomically Based Human Hand Models, ACM SIGGRAPH / Eurographics Symposium on Computer Animation (SCA '03), pp 98-109.

Alexander, H., Cook, T. H., (1977), Accounting for natural tension in the mechanical testing of human skin. The Journal of Investigative Dermatology, 69, 310-314.

Ankersen, J., Birkbeck, A. E., Thomson, R. D., Vanezis, P., (1999), Puncture resistance and tensile strength of skin simulants. Proceedings Of The Institution Of Mechanical Engineers.Part H, Journal Of Engineering In Medicine, 213, 493-501.

Atsu, S. S., Gokdemir, K., Kedici, P. S., Ikyaz, Y. Y., (1998), Bitemarks in forensic odontology. The Journal Of Forensic Odonto-Stomatology, 16, 30-34.

Bando, Y., Kuratate, T., Nishita T., (2002), A simple method for modeling wrinkles on human skin, Proceedings of the 10th Pacific Conference on Computer Graphics and Applications, Beijing, China, pp 166-175.

Barbenel, J. C., Evans, J. H., (1977), The time-dependent mechanical properties of skin. The Journal of Investigative Dermatology, 69, 318-320.

Barker, D. E., (1951), Skin thickness in the human. Plast Reconstr Surg, 7, 115-116.

Batisse, D., Bazin, R., Baldeweck, T., Querleux, B., Leveque, J. L., (2002), Influence of age on the wrinkling capacities of skin. Skin Research and Technology, 8, 148-154.

Bellamy, K., Limbert, G., Waters, M. G., Middleton, J., (2003), An elastomeric material for facial prostheses: synthesis, experimental and numerical testing aspects. Biomaterials, 24, 5061-5066.

Bergstrom, J. S., (2006), Experimental material data and constitutive models. Retrieved May 22nd 2006, from www.polymerfem.com.

Bergstrom, J. S., Boyce, M. C., (2001), Constitutive modeling of the time-dependent and cyclic loading of elastomers and application to soft biological tissues. Mechanics of Materials, 33, 523-530.

Bergstrom, J. S., Boyce, M. C., (1998), Constitutive modeling of the large strain time-dependent behavior of elastomers. Journal of the Mechanics and Physics of Solids, 46, 931-954.

Bezzant, J. L., (2000), Fibrous Septae. Retrieved 3rd April 2006, from http://medstat.med.utah.edu/kw/derm/.

Bischoff, J. E., (2006), Reduced parameter formulation for incorporating fiber level viscoelasticity into tissue level biomechanical models. Annals Of Biomedical Engineering, 34, 1164-1172.

Bischoff, J. E., Arruda, E. M., Grosh, K., (2004), A rheological network for the continuum anisotropic and viscoelastic behavior of soft tissue. Biomechanics and Modeling in Mechanobiology, 3, 56-65.

Bischoff, J. E., Arruda, E. M., Grosh, K., (2002a), A microstructurally based orthotropic hyperelastic constitutive law. Journal of Applied Mechanics, 69, 570-579.

Bischoff, J. E., Arruda, E. M., Grosh, K., (2002b), Finite element simulations of orthotropic hyperelasticity. Finite Elements in Analysis and Design, 38, 983-998.

Bischoff, J. E., (2001), Constitutive Modelling and Testing of Biological Soft Tissue. PhD Thesis, University of Michigan.

Bischoff, J. E., Arruda, E. M., Grosh, K., (2001), Measurement of Orthotropic Material Properties and Constitutive Modeling of Soft Tissue, Bioengineering Conference ASME, pp 415-416.

Borges, A. F., (1989), Relaxed skin tension lines. Dermatologic Clinics, 7, 169-177.

Boyce, M. C., Weber, G. G., Parks, D. M., (1989), On the kinematics of finite strain plasticity. Journal of the Mechanics and Physics of Solids, 37, 647-665.

Bro-Nielsen, M., (1998), Finite element modeling in surgery simulation, Proceedings of the IEEE, pp 490-503.

Brown, I. A., (1973), A scanning electron microscope study of the effects of uniaxial tension on human skin. The British Journal Of Dermatology, 89, 383-393.

Bucalo, B. D., Iriondo, M., (1995), Photoelastic models of wound closure stress. Dermatologic Surgery, 21, 210-212.

Cacou, C., Muir, I. F., (1995), Effects of plane mechanical forces in wound healing in humans. Journal Of The Royal College Of Surgeons Of Edinburgh, 40, 38-41.

Cerda, E., (2005), Mechanics of scars. Journal of Biomechanics, 38, 1598-1603.

Cerda, E., Mahadevan, L., (2003), Geometry and physics of wrinkling. Physical Review Letters, 90, 074302.

Chabanas, M., Luboz, V., Payan, Y., (2003), Patient specific finite element model of the face soft tissues for computer-assisted maxillofacial surgery. Medical Image Analysis, 7, 131-151.

Chynoweth, D. P., (2006), Skin schematic. Retrieved 4th April 2006, from http://www.agen.ufl.edu/~chyn/age2062/lect/lect_19/.

Cohen, B. J., Wood, D. L., (2000), The Skin in Health and Disease. The Human Body in Health and Disease. Lipponcott Williams and Wilkins, Philadelphia, pp. 78-90.

Daly, C. H., (1982), Biomechanical properties of dermis. The Journal of Investigative Dermatology, 79, 17s-20s.

Dandekar, K., Raju, B. I., Srinivasan, M. A., (2003), 3-D finite-element models of human and monkey fingertips to investigate the mechanics of tactile sense. Journal of Biomechanical Engineering, 125, 682-691.

Danielson, D. A., Natarajan, S., (1975), Tension field theory and the stress in stretched skin. Journal of Biomechanics, 8, 135-142.

Davis, S. P., Landis, B. J., Adams, Z. H., Allen, M. G., Prausnitz, M. R. M., (2004), Insertion of microneedles into skin: measurement and prediction of insertion force and needle fracture force. Journal of Biomechanics, 37, 1155-1163.

De Gennes, P. G., (1971), Reptation of a Polymer Chain in the Presence of Fixed Obstacles. Journal of Chemical Physics, 55, 572-579.

De Magalhaes Correia, J. P., Ferron, G., (2004), Wrinkling of anisotropic metal sheets under deep-drawing: analytical and numerical study. Journal of Materials Processing Technology, 155-156, 1604-1610.

Del Prete, Z., Antoniucci, S., Hoffman, A. H., Grigg, P., (2004), Viscoelastic properties of skin in Mov-13 and Tsk mice. Journal of Biomechanics, 37, 1491-1497.

Doi, M., Edwards, S. F., (1986), The Theory of Polymer Dynamics. Oxford University Press.

Dupuytren, G., (1834), Traite Theorique et Practique des Blessures par Armes de Guerre. Maison, Paris.

Ferguson, J., Barbenel, J. C., (1981), Skin surface patterns and the directional mechanical properties of the dermis. In: Payne, P. A., Marks, R. (Eds.), Bioengineering and the Skin. MTP Press, pp. 83-92.

Fischer, T. W., Wigger-Alberti, W., Elsner, P., (1999), Direct and non-direct measurement techniques for analysis of skin surface topography. Skin Pharmacology And Applied Skin Physiology, 12, 1-11.

Fung, Y. C., (1993), Biomechanics:Mechanical Properties of Living Tissues. Springer-Verlag, New York.

Fyhrie, D. P., Barone, J. R., (2003), Polymer dynamics as a mechanistic model for the flow-independent viscoelasticity of cartilage. Journal of Biomechanical Engineering, 125, 578-584.

Gadelmawla, E. S., Koura, M. M., Maksoud, T. M. A., Elewa, I. M., Soliman, H. H., (2002), Roughness parameters. Journal of Materials Processing Technology, 123, 133-145.

Gambino, H. J., (1992), Modern Esthetics: A Scientific Source for Estheticians. Milady.

Geminard, J. C., Bernal, R., Melo, F., (2004), Wrinkle formations in axi-symmetrically stretched membranes. The European Physical Journal.E, Soft Matter, 15, 117-126.

Gerling, G. J., Thomas, G. W., (2003), The Effect of Fingertip Microstructures on Tactile Edge Perception, First Joint Eurohaptics Conference and Symposium on Haptic Interfaces for Virtual Environment and Teleoperator Systems (WHC'05), Pisa, Italy, pp 63-72.

Gray, J., (1997), The world of skin care. Retrieved 26th April 2006, from http://www.pg.com/science/skincare/.

Har-Shai, Y., Bodner, S. R., Egozy-Golan, D., Lindenbaum, E. S., Ben-Izhak, O., Mitz, V., Hirshowitz, B., (1996), Mechanical properties and microstructure of the superficial musculoaponeurotic system. Plastic and Reconstructive Surgery, 98, 59-70.

Hatzis, J., (2004), The wrinkle and its measurement--: A skin surface Profilometric method. Micron, 35, 201-219.

Haughton, D. M., McKay, B. A., (1995), Wrinkling of annular discs subjected to radial displacements. International Journal of Engineering Science, 33, 335-350.

Hendriks, F. M., Brokken, D., Oomens, C. W. J., Bader, D. L., Baaijens, F. P. T., (2006), The relative contributions of different skin layers to the mechanical behavior of human skin in vivo using suction experiments. Medical Engineering & Physics, 28, 259-266.

Hendriks, F. M., (2005), Mechanical behaviour of human epidermal and dermal layers in vivo. PhD Thesis, Technische Universiteit Eindhoven.

Hendriks, F. M., Brokken, D., van Eemeren, J. T. W. M., Oomens, C. W. J., Baaijens, F. P. T., Horsten, J. B. A. M., (2003), A numerical-experimental method to characterize the non-linear mechanical behaviour of human skin. Skin Research and Technology, 9, 274-283.

Hibbitt, Karlsson, Sorensen, (2004), ABAQUS Analysis User's Manual Version 6.5. ABAQUS, Inc., Pawtucket, RI, USA.

Holzapfel, G. A., (2000), Nonlinear Solid Mechanics. John Wiley & Sons Ltd.

Holzapfel, G. A., Eberlein, R., Wriggers, P., Weizsacker, H. W., (1996), Large strain analysis of soft biological membranes: Formulation and finite element analysis. Computer Methods in Applied Mechanics and Engineering, 132, 45-61.

Igarashi, T., Nishino, K., Nayar, S. K., (2005), The Appearance of Human Skin. Columbia University, pp. 1-88.

Jacobi, U., Chen, M., Frankowski, G., Sinkgraven, R., Hund, M., Rzany, B., Sterry, W., Lademann, J., (2004), In vivo determination of skin surface topography using an optical 3D device. Skin Research and Technology, 10, 207-214.

Jing, F., Joneja, A., Tang, K., (2005), Modeling wrinkles on smooth surfaces for footwear design. Computer-Aided Design, 37, 815-823.

Jones, I., Currie, L., Martin, R., (2002), A guide to biological skin substitutes. British Journal of Plastic Surgery, 55, 185-193.

Kahler, K., Haber, J., Seidel, H. P., (2003), Reanimating the dead: Reconstruction of expressive faces from skull data. ACM Transactions on Graphics, 22, 554-561.

Kawka, M., Olejnik, L., Rosochowski, A., Sunaga, H., Makinouchi, A., (2001), Simulation of wrinkling in sheet metal forming. Journal of Materials Processing Technology, 109, 283-289.

Khatyr, F., Imberdis, C., Vescovo, P., Varchon, D., Lagarde, J. M., (2004), Model of the viscoelastic behaviour of skin in vivo and study of anisotropy. Skin Research and Technology, 10, 96-103.

133

Kirby, S. D., Wang, B., To, C. W., Lampe, H. B., (1998), Nonlinear, three-dimensional finite-element model of skin biomechanics. The Journal of Otolaryngology, 27, 153-160.

Kligman, A. M., Zheng, P., Lavker, R. M., (1985), The anatomy and pathogenesis of wrinkles. The British Journal Of Dermatology, 113, 37-42.

Koch, R. J., (1997), An overview of facial wrinkles. The Western Journal Of Medicine, 167, 428.

Koutroupi, K. S., Barbenel, J. C., (1990), Mechanical and failure behaviour of the stratum corneum. Journal of Biomechanics, 23, 281-287.

Kumar, S., (2005), Exploratory analysis of global cosmetic industry: major players, technology and market trends. Technovation, 25, 1263-1272.

Lacour, S. P., Jones, J., Suo, Z., Wagner, S., (2004), Design and performance of thin metal film interconnects for skin-like electronic circuits. IEEE Electron Device Letters, 25, 179-181.

Lagarde, J. M., Rouvrais, C., Black, D., Diridollou, S., Gall, Y., (2001), Skin topography measurement by interference fringe projection: a technical validation. Skin Research and Technology, 7, 112-121.

Langer, K., (1978), On the anatomy and physiology of the skin. III. The elasticity of the cutis By Professor K. Langer Presented at the meeting of 27th November 1861. British Journal of Plastic Surgery, 31, 185-199.

Langer, K., (1861), Zur Anatomie und Physiologie der Haut1. Ueber der Spaltbarkeit der Cutis. Sitzungsber.der Akademie der Wissenschaften in Wien, 44.

Lanir, Y., (1987), Skin Mechanics. In: Skalak, R., Shu, C. (Eds.), Handbook of Bioengineering. McGraw-Hill, New York, London, p. 11.1-11.25.

Lanir, Y., (1983), Constitutive equations for fibrous connective tissues. Journal of Biomechanics, 16, 1-12.

Lanir, Y., (1979a), The rheological behavior of the skin: experimental results and a structural model. Biorheology, 16, 191-202.

Lanir, Y., (1979b), A structural theory for the homogeneous biaxial stress-strain relationships in flat collagenous tissues. Journal of Biomechanics, 12, 423-436.

Lanir, Y., Fung, Y. C., (1974), Two-dimensional mechanical properties of rabbit skin--II. Experimental results. Journal of Biomechanics, 7, 171-182.

Larrabee, W. F., Jr., Galt, J. A., (1986), A finite element model of skin deformation. III. The finite element model. The Laryngoscope, 96, 413-419.

Leach, R. K., Harris, P. M., (2002), Ambiguities in the definition of spacing parameters for surface-texture characterization. Material Science and Technology, 13, 1924-1930.

Lee, Y., Hwang, K., (2002), Skin thickness of Korean adults. Surgical and Radiologic Anatomy, 24, 183-189.

Lehmuskallio, E., (2001), Cold protecting emollients and frostbite. PhD Thesis, University of Oulu.

Leider, M., Buncke, C. M., (1954), Physical dimensions of the skin; determination of the specific gravity of skin, hair, and nail. A.M.A.Archives of Dermatology and Syphilology, 69, 563-569.

Lemperle, G., Holmes, R. E., Cohen, S. R., Lemperle, S. M., (2001), A classification of facial wrinkles. Plastic And Reconstructive Surgery, 108, 1735-1750.

Leveque, J. L., (1999), EEMCO guidance for the assessment of skin topography. Journal of the European Academy of Dermatology and Venereology, 12, 103-114.

Lott-Crumpler, D. A., Chaudhry, H. R., (2001), Optimal patterns for suturing wounds of complex shapes to foster healing. Journal of Biomechanics, 34, 51-58.

Macura, M. J., Feller, B. K, Rye, N. L, Hwang, L., Anast, J. M, Brunner, M. E., and Kirkbride, T. M, (2005), Method of Analysis of Comfort for Virtual Prototyping System., WO2005088484.

Magnenat-Thalmann, N., Kalra, P., Leveque, J. L., Bazin, R., Batisse, D., Querleux, B., (2002), A computational skin model: fold and wrinkle formation. IEEE Transactions On Information Technology In Biomedicine, 6, 317-323.

Mahvash, M., Hayward, V., (2001), Haptic rendering of cutting: A fracture mechanics approach. Haptics-E, 2, 1-12.

Mathews, J. H., Kink, K. K., (2004), Numerical Methods Using Matlab. Prentice-Hall Inc., New Jersey.

Miller, K., (2000), Constitutive modelling of abdominal organs. Journal of Biomechanics, 33, 367-373.

Miller, R. K., Hedgepeth, J. M., Weingarten, V. I., Das, P., Kahyai, S., (1985), Finite element analysis of partly wrinkled membranes. Computers & Structures, 20, 631-639.

Miller-Young, J. E., Duncan, N. A., Baroud, G., (2002), Material properties of the human calcaneal fat pad in compression: experiment and theory. Journal of Biomechanics, 35, 1523-1531.

Miyamura, T., (2000), Wrinkling on stretched circular membrane under in-plane torsion: bifurcation analyses and experiments. Engineering Structures, 22, 1407-1425.

Moore, A., (2002), The biochemistry of beauty. The science and pseudo-science of beautiful skin. EMBO Reports, 3, 714-717.

Mota, A., Klug, W. S., Ortiz, M., Pandolfi, A., (2003), Finite-element simulation of firearm injury to the human cranium. Computational Mechanics, 31, 115-121.

Mow, V. C., Kuei, S. C., Lai, W. M., Armstrong, C. G., (1980), Biphasic creep and stress relaxation of articular cartilage in compression: Theory and experiments. Journal of Biomechanical Engineering, 102, 73-84.

Murrell, F., (2006), Application of finite element analysis in Proctor & Gamble to develop superior product performance of medical devices and incontinence products, 7th International Symposium on Computer Methods in Biomechanics and Biomedical Engineering, Juan Les Pins, France.

Oba, A., Edwards, C., (2006), Relationships between changes in mechanical properties of the skin, wrinkling, and destruction of dermal collagen fiber bundles caused by photoaging. Skin Research and Technology, 12, 283-288.

Odland, G., (1991), Structure of the skin. In: Goldsmith, L. A. (Ed.), Biology of the skin. Oxford University Press, pp. 3-62.

Olsen, L., Sherratt, J. A., Maini, P. K., (1995), A Mechanochemical Model for Adult Dermal Wound Contraction and the Permanence of the Contracted Tissue Displacement Profile. Journal of Theoretical Biology, 177, 113-128.

Oxlund, H., Manschot, J., Viidik, A., (1988), The role of elastin in the mechanical properties of skin. Journal of Biomechanics, 21, 213-218.

Pan, L., Zan, L., Foster, F. S., (1998), Ultrasonic and viscoelastic properties of skin under transverse mechanical stress in vitro. Ultrasound in Medicine & Biology, 24, 995-1007.

Park, A. C., Baddiel, C. B., (1972), Rheology of stratum corneum.-I:A molecular interpretation of the stress-strain curve. Journal of the Society of Cosmetic Chemists of Great Britain, 23, 3-12.

Park, S. I., Hodgins, J. K., (2006), Capturing and Animating Skin Deformation in Human Motion. ACM Transaction on Graphics (SIGGRAPH 2006), 25, 881-889.

Pereira, J. M., Mansour, J. M., Davis, B. R., (1991), Dynamic measurement of the viscoelastic properties of skin. Journal of Biomechanics, 24, 157-162.

Pierard, G. E., Uhoda, I., Pierard-Franchimont, C., (2003), From skin microrelief to wrinkles. An area ripe for investigation. Journal of Cosmetic Dermatology, 2, 21-28.

Pipkin, A. C., (1994), Relaxed energy densities for large deformations of membranes. IMA Journal of Applied Mathematics, 52, 297-308.

Price, E., (2005), Design and validation of a device to measure the cutting edge profile of osteotomes. Master of Engineering, Institute of Technology, Sligo.

Raible, T., Tegeler, K., Lohnert, S., Wriggers, P., (2005), Development of a wrinkling algorithm for orthotropic membrane materials. Computer Methods in Applied Mechanics and Engineering, 194, 2550-2568.

Ramos-e-Silva, M., Ribeiro de Castro, M. C., (2002), New dressings, including tissue-engineered living skin. Clinics in Dermatology, 20, 715-723.

Reihsner, R., Balogh, B., Menzel, E. J., (1995), Two-dimensional elastic properties of human skin in terms of an incremental model at the in vivo configuration. Medical Engineering & Physics, 17, 304-313.

Retel, V., Vescovo, P., Jacquet, E., Trivaudey, F., Varchon, D., Burtheret, A., (2001), Nonlinear model of skin mechanical behaviour analysis with finite element method. Skin Research and Technology, 7, 152-158.

Ridge, M. D., Wright, V., (1965), The rheology of skin. A bio-engineering study of the mechanical properties of human skin in relation to its structure. The British Journal Of Dermatology, 77, 639-649.

Roff, W. J., (1971), Fibres, Films, Plastics and Rubbers: A Handbook of Common Polymers. Butterworths, London.

Rubin, M. B., Bodner, S. R., (2002), A three-dimensional nonlinear model for dissipative response of soft tissue. International Journal of Solids and Structures, 39, 5081-5099.

Sanders, J. E., Goldstein, B. S., (2001), Collagen fibril diameters increase and fibril densities decrease in skin subjected to repetitive compressive and shear stresses. Journal of Biomechanics, 34, 1581-1587.

Sano, T., Kume, T., Fujimura, T., Kawada, H., Moriwaki, S., Takema, Y., (2005), The formation of wrinkles caused by transition of keratin intermediate filaments after repetitive UVB exposure. Archives Of Dermatological Research, 296, 359-365.

Scheinfeld, N. S., (2004), Obesity and dermatology. Clinics in Dermatology, 22, 303-309.

Schellander, F. A., Headington, J. T., (1974), The stratum corneum--some structural and functional correlates. The British Journal Of Dermatology, 91, 507-515.

Schneider, D., (1982), Viscoelasticity and tearing strength of the human skin. PhD Thesis, University of California, San Diego.

Serina, E. R., Mockensturm, E., Mote, J., Rempel, D., (1998), A structural model of the forced compression of the fingertip pulp. Journal of Biomechanics, 31, 639-646.

Shergold, O. A., Fleck, N. A., Radford, D., (2006), The uniaxial stress versus strain response of pig skin and silicone rubber at low and high strain rates. International Journal of Impact Engineering, 32, 1384-1402.

Shoemaker, P. A., Schneider, D., Lee, M. C., Fung, Y. C., (1986), A constitutive model for two-dimensional soft tissues and its application to experimental data. Journal of Biomechanics, 19, 695-702.

Silver, F. H., Freeman, J. W., DeVore, D., (2001), Viscoelastic properties of human skin and processed dermis. Skin Research and Technology, 7, 18-23.

Silver, F. H., Kato, Y. P., Ohno, M., Wasserman, A. J., (1992), Analysis of mammalian connective tissue: Relationship between hierarchical structures and mechanical properties. Journal of Long-Term Effects of Medical Implants, 2, 165-198.

Sivamani, R. K., Goodman, J., Gitis, N. V., Maibach, H. I., (2003), Friction coefficient of skin in real-time. Skin Research and Technology, 9, 235-239.

Smalls, L. K., Lee, C. Y., Whitestone, J., Kitzmiller, W. J., Wickett, R. R., Visscher, M. O., (2005), Quantitative model of cellulite: three-dimensional skin surface topography, biophysical characterization, and relationship to human perception. International Journal of Cosmetic Science, 27, 253.

Stadelmann, W. K., Digenis, A. G., Tobin, G. R., (1998), Physiology and healing dynamics of chronic cutaneous wounds. The American Journal of Surgery, 176, 26S-38S.

Stanuszek, M., (2003), FE analysis of large deformations of membranes with wrinkling. Finite Elements in Analysis and Design, 39, 599-618.

139

Steigmann, D. J., (1990), Tension field theory. Proceedings of the Royal Society of London, Series A (Mathematical and Physical Sciences), 429, 141-173.

Subke, J., Schmeltzpfenning, T., Kinn, U., (2006), Digital Three-Dimensional Facial Reconstruction Including Typical Signs of Ageing, Proceedings of the 7th International Symposium on Computer Methods in Biomechanics and Biomedical Engineering, Juan Les Pins, France.

Takahashi, M., Kawasaki, K., Tanaka, M., Ohta, S., Tsuda, Y., (1980), The mechanism of stratum corneum plasticization with water. In: Payne, P. A. (Ed.), Bioengineering and the Skin. MTP Press, Hingham, MA, pp. 67-73.

Terzopoulos, D., Waters, K., (1990), Physically-Based Facial Modeling, Analysis, and Animation. Journal of Visualization and Computer Animation, 1, 73-80.

Tessler, A., Sleight, D., Wang, J., (2005), Effective modeling and nonlinear shell analysis of thin membranes exhibiting structural wrinkling. Journal of Spacecraft and Rockets, 42, 287-298.

Thali, M. J., Braun, M., Markwalder, T., Brueschweiler, W., Zollinger, U., Malik, N. J., Yen, K., Dirnhofer, R., (2003), Bite mark documentation and analysis: the forensic 3D/CAD supported photogrammetry approach. Forensic Science International, 135, 115-121.

Thali, M. J., Kneubuehl, B. P., Zollinger, U., Dirnhofer, R., (2002a), A study of the morphology of gunshot entrance wounds, in connection with their dynamic creation, utilizing the "skin-skull-brain model". Forensic Science International, 125, 190-194.

Thali, M. J., Kneubuehl, B. P., Zollinger, U., Dirnhofer, R., (2002b), The "Skin-skull-brain model": a new instrument for the study of gunshot effects. Forensic Science International, 125, 178-189.

Thali, M. J., Kneubuehl, B. P., Dirnhofer, R., (2002c), A "skin-skull-brain model" for the biomechanical reconstruction of blunt forces to the human head. Forensic Science International, 125, 195-200.

Tong, P., Fung, Y. C., (1976), The stress-strain relationship for the skin. Journal of Biomechanics, 9, 649-657.

Tsang, W., Singh, K., Fiume, E., (2005), Helping Hand: An Anatomically Accurate Inverse Dynamics, ACM SIGGRAPH / Eurographics Symposium on Computer Animation (SCA '05), pp 319-328.

Tsukahara, K., Moriwaki, S., Hotta, M., Fujimura, T., Kitahara, T., (2004), A study of diurnal variation in wrinkles on the human face. Archives Of Dermatological Research, 296, 169-174.

U.S.Department of Health and Human Services, (2005), Guidance for Industry and FDA Staff - Menstrual Tampons and Pads: Information for Premarket Notification Submissions (510(k)s).

Wan Abas, W. A., (1994), Biaxial tension test of human skin in vivo. Bio-Medical Materials and Engineering, 4, 473-486.

Wang, C.-T., (1953), Applied Elasticity. McGraw-Hill, New York.

Wang, J., Chen, T., Sleight, D., Tessler, A., (2004), Simulating Nonlinear Deformations of Solar Sail Membranes Using Explicit Time Integration, Proceedings of the 45th AIAA/ASME/ASCE/AHS/ASC Structures, Structural Dynamics and Materials Conference, pp 1-15

Weili, X., Huibao, W., Yuying, Y., Wang, Z. R., (2002), A simplified method of wrinkling simulation. Journal of Materials Processing Technology, 121, 19-22.

Wilkes, G. L., Brown, I. A., Wildnauer, R. H., (1973), The biomechanical properties of skin. CRC Critical Reviews In Bioengineering, 1, 453-495.

William, A. C., (2003), Transdermal and topical drug delivery - From theory to clinical practice. Pharmaceutical Press, London.

Wong, Y. W., Pellegrino, S., (2006a), Wrinkled membranes III: numerical simulations. Journal of Mechanics of Materials and Structures, 1, 61-94.

Wong, Y. W., Pellegrino, S., (2006b), Wrinkled membranes II: analytical models. Journal of Mechanics of Materials and Structures, 1, 25-59.

Wu, J. Z., Cutlip, R. G., Welcome, D., Dong, R. G., (2006a), Estimation of the viscous properties of skin and subcutaneous tissue in uniaxial stress relaxation tests. Bio-Medical Materials and Engineering, 16, 53-66.

Wu, J. Z., Dong, R. G., (2005), Analysis of the contact interactions between fingertips and objects with different surface curvatures. Proceedings of the I MECH E Part H Journal of Engineering in Medicine, 219, 89-103.

Wu, K. S., van Osdol, W. W., Dauskardt, R. H., (2006b), Mechanical properties of human stratum corneum: Effects of temperature, hydration, and chemical treatment. Biomaterials, 27, 785-795.

Yoshida, H., Tsutsumi, S., Mizunuma, M., Yanai, A., (2001), A surgical simulation system of skin sutures using a three-dimensional finite element method. Clinical Biomechanics, 16, 621-626.

Yoshida, H., Tsutsumi, S., Mizunuma, M., Yanai, A., (2000), Three-dimensional finite element analysis of skin suture: Part 1: Spindle model and S-shaped modified model. Medical Engineering & Physics, 22, 481-485.

Yuan, Y., Verma, R., (2006), Measuring microelastic properties of stratum corneum. Colloids and Surfaces B: Biointerfaces, 48, 6-12.

Zhang, Q., Zicheng, L., Guo, B., Terzopoulos, D., Shum, H. Y., (2006), Geometry-Driven Photorealistic Facial Expression Synthesis. IEEE Transactions on Visualisation and Computer Graphics, 12, 48-60.

Zhang, Y., Prakash, E. C., Sung, E., (2004), Face alive. Journal of Visual Languages & Computing, 15, 125-160.

Zheng, Y. P., Mak, A. F., (1996), An ultrasound indentation system for biomechanical properties assessment of soft tissues in-vivo. IEEE Transactions On Bio-Medical Engineering, 43, 912-918.

Appendix A

Skin Accessories

A.1 Blood vessels

The skin is supplied by blood from branches of the subcutaneous arteries (Odland, 1991). These branches form a small vessel plexus lying deep in the reticular dermis parallel to the interface with the hypodermis (Figure A.1). Further interconnected vessels branch off this plexus towards the surface of the skin. These arterioles are about 50 μm in diameter (Wilkes *et al.*, 1973). At the papillary dermis, there is further branching into smaller arterioles and a formation of a second horizontal plexus. Capillary loops offshoot from this plexus toward the epidermis. No capillaries enter the epidermis (Igarashi *et al.*, 2005). The capillaries drain into venous networks, which in turn drain into increasingly larger vessels, eventually connecting with the subcutaneous venous system. The venous system is connected to the arterial system at every level by a series of shunts (Wilkes *et al.*, 1973). The body controls temperature by dilating the blood vessels, thus allowing an increase in blood flow close to the skin surface. The blood transfers heat to the sweat on the surface, which evaporates and the cooled blood circulates to the core of the body. Blood pressure is regulated in part by controlling the blood flow in the capillaries. If the blood pressure rises, flow is by-passed around the capillaries directly into the venous system.

A.2 Lymphatic vessels

Lymphatic vessels drain excess fluid and particulate matter such as proteins from the dermal tissues. Superficial lymphatic vessels lie immediately below the surface of the skin next to the veins (Cohen and Wood, 2000). They terminate in the papillary layer of the dermis and descend to the hypodermis.

143
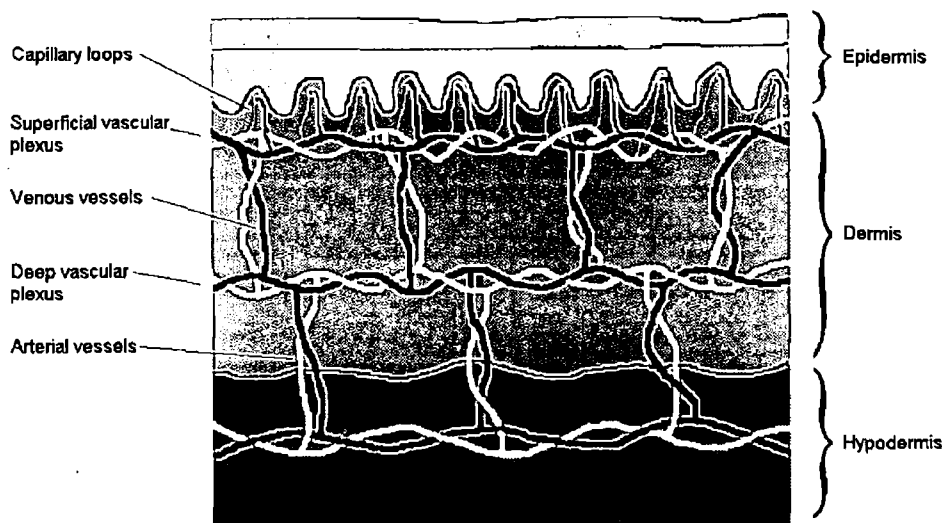
Figure A.1: Simplified schematic of the blood supply to the skin. Arterial vessels are shown in white and veins in black. Adapted from Lehmuskallio (2001)

A.3 Glands

Glands produce and secrete liquids to the skin surface via ducts. Glands differ in terms of their function and structure. Eccrine sweat glands originate as coiled structures in the deep dermis or hypodermis and extend through the epidermis to the skin surface. These sweat glands secrete a watery substance containing sodium chloride onto the skin surface. Evaporation of this substance aids in body temperature regulation as described earlier. The apocrine glands occupy the lower dermis and upper hypodermis and are about ten times larger than the eccrine glands. The apocrine gland is activated by mental stress and sexual stimuli and secretes a turbid milky substance into the hair follicles giving off body odours. Sebaceous glands also secrete directly into the hair follicle. They are located 200 µm to 500 µm beneath the skin surface and are most numerous on the scalp, face and forehead. The greasy sebum it secretes helps maintain a supple stratum corneum.

A.4 Hair

Hairs are keratinous fibres and are produced in hair follicles. These follicles are distributed all over the skin surface except the soles of the feet and palms of the hands. They are tube-like structures that extend from the deep dermis to the surface in a slanting manner. The base of the follicle is an indented bulb above which cells are

divided and pushed along the follicle to be compacted and keratinised into hair. There are two types of hair in humans – (a) terminal hair, which is located on the scalp and trunk (to a greater degree in males than females); (b) and vellus hair, which is fine hair that rarely, grows to lengths greater than 1cm. The arrector pili muscle is connected between the sheath of the hair follicle and the papillary dermis. When the body wishes to retain body heat this muscle contracts and the hair stands erect, producing the "goose-pimple" effect on the skin surface. This action serves to trap an insulating layer of air next to the skin surface but is almost ineffectual in humans due to the lack of body hair.

A.5 Nerves

Human skin is supplied with an extensive nerve network that allows sensations such as touch, pain, warmth and cold. Nerves branch off from the spinal column to form cutaneous nerves lying in the hypodermis. From these nerves, a plexus is formed parallel to the skin surface in the deep dermis. Branches ascend through the dermis to another tangled plexus in the upper dermis. From either plexus, further branches may form specialised receptors or may remain as basic axonal units known as free nerve endings and associated with pain and itch. There are several different types of specialised receptor. Merkel cells are slowly adapting mechanoreceptors for touch. They are found mainly in the epidermis lying at the base of a ridge. Meissner's touch corpuscles are located in the dermal papillae of the palm or sole. Pacinian corpuscles occur in the deep dermis and hypodermis of palmar tissues. These receptors can signal local changes in blood flow and also detect vibrations. Krause's end-bulbs are thermoreceptors located in the dermis and hypodermis that register the sensation of cold. Thermoreceptors that register the sensation of heat are Ruffini's corpuscles (Gambino, 1992).

Appendix B

Implementing user materials into finite element models

B.1 ABAQUS/Explicit implementation

The implementation of the constitutive law into ABAQUS/Explicit is achieved via the VUMAT user subroutine. Coding of a VUMAT is more straightforward than a UMAT as it does not require the definition of the Jacobian matrix. The Cauchy stress tensor is given by

$$T = \frac{1}{J}F\frac{\partial W}{\partial E}F^T \tag{B.1}$$

The Cauchy stress tensor is defined in terms of a corotational coordinate system, i.e. a coordinate system that rotates with the material. The corotated Cauchy stress tensor is related to T by

$$T_{corot} = RTR^T \tag{B.2}$$

where R is the rotation tensor.

Substituting Equation B.1 into Equation B.2 gives

$$T_{corot} = \frac{1}{J}R^TF\frac{\partial W}{\partial E}F^TR \tag{B.3}$$

The deformation gradient F is related to the right symmetric stretch tensor U by

$$F = RU \tag{B.4}$$

As R is orthogonal, it follows that $R^T = R^{-1}$ and therefore

$$U = R^TF \tag{B.5}$$

$$U^T = F^TR \tag{B.6}$$

B.5 uses the relationships $(AB)^T = B^TA^T$ and $(A^T)^T = A$. Substituting Equations B.5 and B.6 into Equation B.3 gives

$$\mathbf{T}_{corot} = \frac{1}{J} \mathbf{U} \frac{\partial W}{\partial \mathbf{E}} \mathbf{U}^{\mathrm{T}} \qquad \text{(B.7)}$$

The right symmetric stretch tensor $\mathbf{U}$ is passed into the user subroutine VUMAT. Therefore, Equation B.7 provides a convenient method to calculate the corotational Cauchy stress tensor without having to explicitly account for the rotation.

The code for the VUMAT is contained in Appendix C.

B.2 Verification of the finite element user subroutines

The implementation of the VUMAT user subroutine into ABAQUS/Explicit were verified by comparing finite element results for simple homogeneous deformations with results obtained numerically by solving the system of equations described in Section 3.3.2 of Chapter 3. The deformations used in the verification are the uniaxial and biaxial stretch tests of the rabbit skin and the uniaxial compression tests of the monkey liver described in Section 3.3.2.

B.2.1 Uniaxial and biaxial rabbit skin tests

Single-element finite element analyses of the rabbit skin tests described in Section 3.3.2 were performed and the results compared with those of Figure 3.7. The material parameters were the same as those listed in Figure 3.7. The results of the Finite Element Analyses are shown in Figure B.1. It is clearly seen that all the results match each other demonstrating that the VUMAT subroutine are correctly implemented. Analyses were also run where the single element was rotated to various orientations in space and the results were identical to those obtained in Figure B.1. Multi-element simulations were also run and the results were the same for all cases.

B.2.2 Uniaxial compression monkey liver tests

To verify the user subroutines under compressive deformations, single-element finite element analyses of the monkey liver tests (Bergstrom and Boyce, 2001) described in Section 3.3.2 were run and the results compared with those in Figure 3.15. The results of the finite element analyses along with the numerical results are shown in Figure B.2. As in the rabbit skin tests, analyses were run with the single-element rotated to various orientations in space and also multi-element simulations were run. All the results agree with each other, demonstrating the correct implementation of the VUMAT user subroutine.
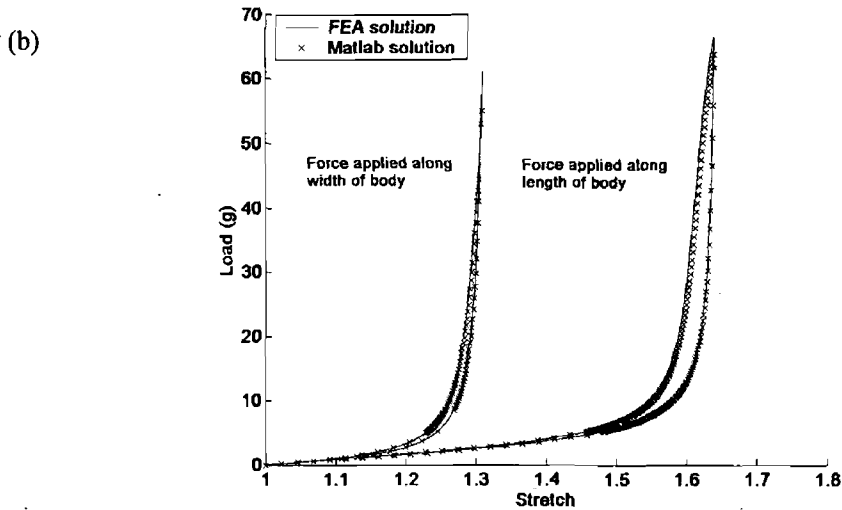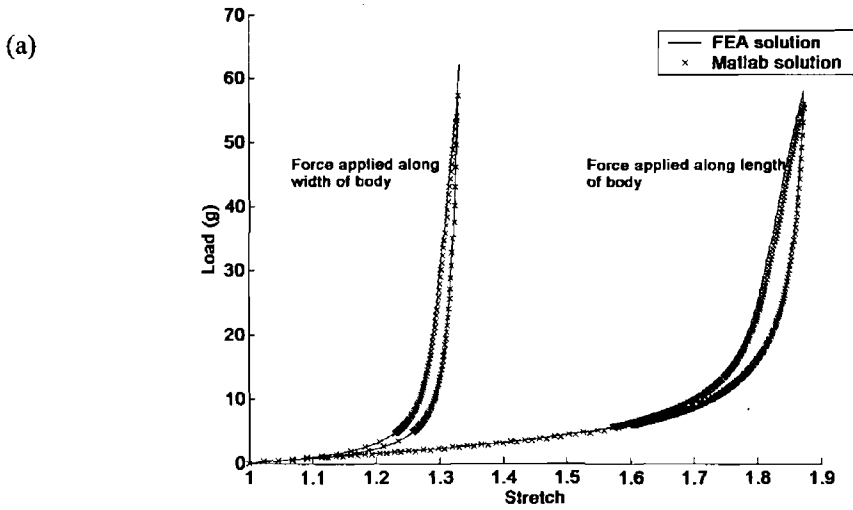
Figure B.1: Verification of VUMAT subroutine by comparison of Finite Element Analyses of rabbit skin tests with numerical results of Figure 3.7(a) and Figure 3.7(b).
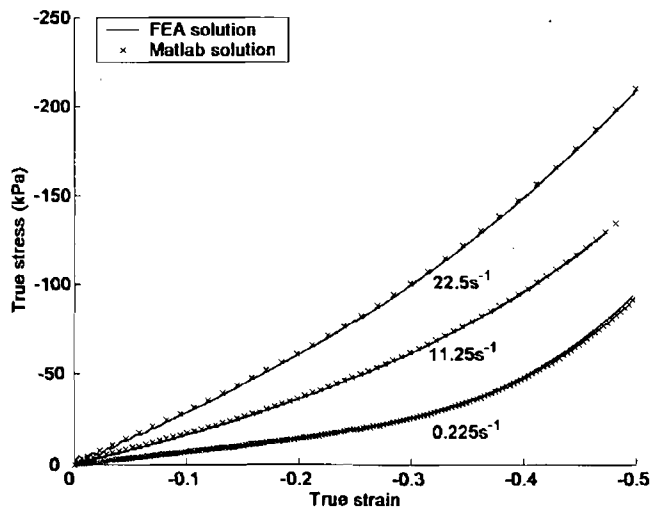
Figure B.2: Verification of VUMAT subroutines by comparison of Finite Element Analyses of monkey liver tests with numerical results of Figure 3.15.

148

Appendix C

VUMAT User subroutine

```fortran
      subroutine vumat(
1    nblock, ndir, nshr, nstatev, nfieldv, nprops, lanneal,
2    stepTime, totalTime, dt, cmname, coordMp, charLength,
3    props, density, strainInc, relSpinInc,
4    tempOld, stretchOld, defgradOld, fieldOld,
5    stressOld, stateOld, enerInternOld, enerInelasOld,
6    tempNew, stretchNew, defgradNew, fieldNew,
7    stressNew, stateNew, enerInternNew, enerInelasNew )
C
     include 'vaba_param.inc'
C
     dimension props(nprops), density(nblock), coordMp(nblock,*),
1    charLength(nblock), strainInc(nblock,ndir+nshr),
2    relSpinInc(nblock,nshr), tempOld(nblock),
3    stretchOld(nblock,ndir+nshr),
4    defgradOld(nblock,ndir+nshr+nshr),
5    fieldOld(nblock,nfieldv), stressOld(nblock,ndir+nshr),
6    stateOld(nblock,nstatev), enerInternOld(nblock),
7    enerInelasOld(nblock),tempNew(nblock),
8    stretchNew(nblock,ndir+nshr),
8    defgradNew(nblock,ndir+nshr+nshr),
9    fieldNew(nblock,nfieldv),
1    stressNew(nblock,ndir+nshr), stateNew(nblock,nstatev),
2    enerInternNew(nblock), enerInelasNew(nblock)
C
     character*80 cmname
C
     call material_ortho_visco(nblock,ndir,nshr, nstatev, nfieldv,
2    nprops, lanneal, stepTime, totalTime, dt, cmname, charLength,
3    props, density, strainInc, relSpinInc, tempOld, stretchOld,
4    defgradOld, fieldOld, stressOld, stateOld, enerInternOld,
5    enerInelasOld, tempNew, stretchNew, defgradNew, fieldNew,
6    stressNew, stateNew, enerInternNew, enerInelasNew )
     return
     end
C
     END
!DEC$ FREEFORM

! ****************************************************************

subroutine material_ortho_visco(nblock, ndir, nshr, nstatev, nfieldv,
nprops, lanneal, stepTime, totalTime, dt, cmname,          &
```

```fortran
     charLength, props, density, strainInc, relSpinInc, tempOld,     &
     stretchOld, defgradOld, fieldOld, stressOld, stateOld,          &
     enerInternOld, enerInelasOld, tempNew, stretchNew, defgradNew, &
     fieldNew, stressNew, stateNew, enerInternNew, enerInelasNew )
     implicit none

     ! Declare variables that are passed into this routine
     integer, intent(in) :: nstatev ! No. of solution dependent state
     integer, intent(in) :: nblock  ! variables
     integer, intent(in) :: nprops  ! No. of material constants
     integer, intent(in) :: ndir    ! No. of direct stress components
     integer, intent(in) :: nshr    ! No. of shear stress components
     integer, intent(in) :: nfieldv !
     integer, intent(in) :: lanneal


     real, intent(in)      :: charLength
     real, intent(in)      :: stepTime
     real, intent(in)      :: totalTime
     real, intent(in)      :: dt


     real, intent(in), dimension(nblock)               :: density
     real, intent(in), dimension(nblock)               :: tempOld
     real, intent(in), dimension(nblock)               :: tempNew
     real, intent(in), dimension(nblock,ndir+nshr)     :: stretchOld
     real, intent(in), dimension(nblock,ndir+nshr)     :: stretchNew
     real, intent(in), dimension(nblock,ndir+2*nshr)   :: defgradOld
     real, intent(in), dimension(nblock,ndir+2*nshr)   :: defgradNew
     real, intent(in), dimension(nblock, nfieldv)      :: fieldOld
     real, intent(in), dimension(nblock, nfieldv)      :: fieldNew
     real, intent(in), dimension(nblock,ndir+nshr)     :: stressOld
     real, intent(in), dimension(nblock, nstatev)      :: stateOld
     real, intent(in), dimension(nblock)               :: enerInternOld
     real, intent(in), dimension(nblock)               :: enerInelasOld
     real, intent(in), dimension(nprops)               :: props
     real, intent(in), dimension(nblock, ndir+nshr)    :: strainInc
     real, intent(in), dimension(nblock, nshr)         :: relSpinInc
     real, intent(inout), dimension(nblock, ndir+nshr) :: stressNew
     real, intent(inout), dimension(nblock, nstatev)   :: stateNew
     real, intent(inout), dimension(nblock)            :: enerInternNew
     real, intent(inout), dimension(nblock)            :: enerInelasNew

     character(len=80), intent(in)                     :: cmname

     ! Declare variables that originate in this routine
     integer             :: iblock
     real                :: stressPower
     real                :: trace_cauchy_stressB_prev
     real                :: tauB
     real                :: lBp_chain
     real                :: creep_rateB
     real                :: trace_Bv
     real, dimension(3,3) :: cauchy_stress          ! Cauchy stress Tensor
     real, dimension(3,3) :: cauchy_stressB         ! Cauchy stress Tensor
     real, dimension(3,3) :: cauchy_stressB_prev ! Cauchy stress Tensor
     real, dimension(3,3) :: dfgrd1                  ! from previous time-step
     real, dimension(3,3) :: dfgrd1Be
     real, dimension(3,3) :: dfgrd1Be_inverse
     real, dimension(3,3) :: dfgrd1BpOld            ! From two time-steps ago
     real, dimension(3,3) :: dfgrd1Bp               ! From previous time-step
     real, dimension(3,3) :: dfgrd1Bp_new
     real, dimension(3,3) :: dfgrd1Bp_inverse
```

150

```fortran
real, dimension(3,3) :: dfgrd1Bp_transpose
real, dimension(3,3) :: dfgrd1Bpdt
real, dimension(3,3) :: Bv
real, dimension(3,3) :: Tprime
real, dimension(3,3) :: Tprime2
real, dimension(3,3) :: Direction
real, dimension(3,3) :: real_matrix
real, dimension(3,3) :: real_matrix2
logical              :: error

! Following are the material parameters for the model
real :: n  ! Cross-link density
real :: nB ! Cross-link density of Network B
real :: a  ! Dimension of orthotropic cell
real :: b  !             "
real :: c  !             "
real :: aB ! Dimension of orthotropic cell of Network B
real :: bB !             "
real :: cB !             "
real :: BM ! Bulk modulus
real :: C1 ! Viscoelastic parameters
real :: C2 !             "
real :: m  !             "

integer :: locnum,jrcd
character(len=80) :: cpname

n  = props(1)
nB = props(2)
a  = props(3)
b  = props(4)
c  = props(5)
aB = props(6)
bB = props(7)
cB = props(8)
BM = props(9)
C1 = props(10)
C2 = props(11)
m  = props(12)

do iblock = 1, nblock

  dfgrd1Bp(1,1) = stateOld(iblock,1)
  dfgrd1Bp(1,2) = stateOld(iblock,2)
  dfgrd1Bp(1,3) = stateOld(iblock,3)

  dfgrd1Bp(2,1) = stateOld(iblock,2)
  dfgrd1Bp(2,2) = stateOld(iblock,4)
  dfgrd1Bp(2,3) = stateOld(iblock,5)

  dfgrd1Bp(3,1) = stateOld(iblock,3)
  dfgrd1Bp(3,2) = stateOld(iblock,5)
  dfgrd1Bp(3,3) = stateOld(iblock,6)

  dfgrd1BpOld(1,1) = stateOld(iblock,7)
  dfgrd1BpOld(1,2) = stateOld(iblock,8)
  dfgrd1BpOld(1,3) = stateOld(iblock,9)

  dfgrd1BpOld(2,1) = stateOld(iblock,8)
  dfgrd1BpOld(2,2) = stateOld(iblock,10)
  dfgrd1BpOld(2,3) = stateOld(iblock,11)
```

```
dfgrd1BpOld(3,1) = stateOld(iblock,9)
dfgrd1BpOld(3,2) = stateOld(iblock,11)
dfgrd1BpOld(3,3) = stateOld(iblock,12)

cauchy_stressB_prev(:,:) = 0.0
cauchy_stressB_prev(1,1) = stateOld(iblock,13)
cauchy_stressB_prev(2,2) = stateOld(iblock,14)
cauchy_stressB_prev(3,3) = stateOld(iblock,15)

trace_cauchy_stressB_prev = cauchy_stressB_prev(1,1) + &
                            cauchy_stressB_prev(2,2) + &
                            cauchy_stressB_prev(3,3)

dfgrd1(1,1) = stretchNew(iblock,1)
dfgrd1(1,2) = stretchNew(iblock,4)
dfgrd1(1,3) = stretchNew(iblock,6)

dfgrd1(2,1) = stretchNew(iblock,4)
dfgrd1(2,2) = stretchNew(iblock,2)
dfgrd1(2,3) = stretchNew(iblock,5)

dfgrd1(3,1) = stretchNew(iblock,6)
dfgrd1(3,2) = stretchNew(iblock,5)
dfgrd1(3,3) = stretchNew(iblock,3)

call calculate_stress(dfgrd1,a,b,c,n,BM,cauchy_stress,error)

call matrix_inverse(dfgrd1Bp,dfgrd1Bp_inverse)

call matrix_product(dfgrd1,dfgrd1Bp_inverse,dfgrd1Be,3,3,3)

! Calculate plastic length of chain in Network B
call matrix_transpose(dfgrd1Bp,dfgrd1Bp_transpose,3,3)

call matrix_product(dfgrd1Bp,dfgrd1Bp_transpose,Bv,3,3,3)

trace_Bv = Bv(1,1) + Bv(2,2) + Bv(3,3)

lBp_chain = sqrt( trace_Bv / 3.0 )

Tprime = cauchy_stressB_prev
Tprime(1,1) = Tprime(1,1) - 1.0 / 3.0 * trace_cauchy_stressB_prev
Tprime(2,2) = Tprime(2,2) - 1.0 / 3.0 * trace_cauchy_stressB_prev
Tprime(3,3) = Tprime(3,3) - 1.0 / 3.0 * trace_cauchy_stressB_prev

! Equivalent effective shear stress of Network B
call matrix_product(Tprime,Tprime,Tprime2,3,3,3)

tauB = sqrt( 0.5 * ( Tprime2(1,1)+Tprime2(2,2)+Tprime2(3,3) ) )

! Creep rate of Network B
creep_rateB = C1 * ( lBp_chain - 1.0 + 1e-3 )**C2 * tauB**m

! Calculate direction of driving stress in Network B
if ( tauB < 1e-10 ) then
  Direction(:,:) = 0.0
else
  ! Gives the direction of the driving stress
  Direction = 1.0 / sqrt(2.0) / tauB * Tprime
end if
```

```fortran
! Calculate rate of change of principle plastic stretches of
! Network B
call matrix_product(dfgrd1Be,dfgrd1Bp(:,:),real_matrix,3,3,3)
call matrix_product(Direction,real_matrix,real_matrix2,3,3,3)

call matrix_inverse(dfgrd1Be,dfgrd1Be_inverse)

call matrix_product(dfgrd1Be_inverse,real_matrix2,real_matrix, &
                 3,3,3)
dfgrd1Bpdt = creep_rateB * real_matrix

dfgrd1Bpdt(2,1) = dfgrd1Bpdt(1,2)
dfgrd1Bpdt(3,1) = dfgrd1Bpdt(1,3)
dfgrd1Bpdt(3,2) = dfgrd1Bpdt(2,3)

! Update principle plastic stretches. Use Backward Euler
dfgrd1Bp_new = dfgrd1Bp(:,:) + dt * dfgrd1Bpdt

! Calculate updated principle elastic stretches of Network B
call matrix_inverse(dfgrd1Bp_new,dfgrd1Bp_inverse)

call matrix_product(dfgrd1,dfgrd1Bp_inverse,dfgrd1Be,3,3,3)

call calculate_stress(dfgrd1Be,aB,bB,cB,nB,BM,cauchy_stressB,&
                  error)

cauchy_stressB_prev(1,1) = cauchy_stressB(1,1)
cauchy_stressB_prev(2,2) = cauchy_stressB(2,2)
cauchy_stressB_prev(3,3) = cauchy_stressB(3,3)

stressNew(iblock,1) = cauchy_stress(1,1) + cauchy_stressB(1,1)
stressNew(iblock,2) = cauchy_stress(2,2) + cauchy_stressB(2,2)
stressNew(iblock,3) = cauchy_stress(3,3) + cauchy_stressB(3,3)
stressNew(iblock,4) = cauchy_stress(1,2) + cauchy_stressB(1,2)
stressNew(iblock,5) = cauchy_stress(2,3) + cauchy_stressB(2,3)
stressNew(iblock,6) = cauchy_stress(3,1) + cauchy_stressB(3,1)

stressPower = 0.5 * ( ( stressNew(iblock,1) + &
              stressOld(iblock,1) ) * strainInc(iblock,1) + &
                 ( stressNew(iblock,2) + &
              stressOld(iblock,2) ) * strainInc(iblock,2) + &
                 ( stressNew(iblock,3) + &
              stressOld(iblock,3) ) * strainInc(iblock,3) + &
             2.0 * ( stressNew(iblock,4) + &
              stressOld(iblock,4) ) * strainInc(iblock,4) )

enerInternNew(iblock) = enerInternOld(iblock) + stressPower /  &
                  density(iblock)

! Update state variables
stateNew(iblock,1) = dfgrd1Bp_new(1,1)
stateNew(iblock,2) = dfgrd1Bp_new(1,2)
stateNew(iblock,3) = dfgrd1Bp_new(1,3)

stateNew(iblock,2) = dfgrd1Bp_new(2,1)
stateNew(iblock,4) = dfgrd1Bp_new(2,2)
stateNew(iblock,5) = dfgrd1Bp_new(2,3)

stateNew(iblock,3) = dfgrd1Bp_new(3,1)
stateNew(iblock,5) = dfgrd1Bp_new(3,2)
```

153

```fortran
      stateNew(iblock,6) = dfgrd1Bp_new(3,3)

      stateNew(iblock,7) = dfgrd1Bp(1,1)
      stateNew(iblock,8) = dfgrd1Bp(1,2)
      stateNew(iblock,9) = dfgrd1Bp(1,3)

      stateNew(iblock,8)  = dfgrd1Bp(2,1)
      stateNew(iblock,10) = dfgrd1Bp(2,2)
      stateNew(iblock,11) = dfgrd1Bp(2,3)

      stateNew(iblock,9)  = dfgrd1Bp(3,1)
      stateNew(iblock,11) = dfgrd1Bp(3,2)
      stateNew(iblock,12) = dfgrd1Bp(3,3)

      stateNew(iblock,13) = cauchy_stressB_prev(1,1)
      stateNew(iblock,14) = cauchy_stressB_prev(2,2)
      stateNew(iblock,15) = cauchy_stressB_prev(3,3)
    end do
    return

  end subroutine material_ortho_visco

  ! ****************************************************************

  subroutine calculate_stress(dfgrd1, a, b, c, n, BM, cauchy_stress,
  error)
    implicit none
    real, intent(in) :: a
    real, intent(in) :: b
    real, intent(in) :: c
    real, intent(in) :: n
    real, intent(in) :: BM
    real, intent(in), dimension(3,3)    :: dfgrd1
    real, intent(inout), dimension(3,3) :: cauchy_stress
    logical, intent(out) :: error
    ! Declare variables that originate in this routine
    integer              :: i
    integer              :: j
    integer              :: k
    real                 :: N_links ! Number of links
    real                 :: Pmag    ! Normalised undeformed length
    real                 :: Beta_P  ! Langevin inverse of normalised
                                    ! undeformed length
    real                 :: DetF    ! Ratio of current volume to
original volume (Determinant of the deformation gradient)
    real, dimension(3,4) :: P       ! Normalised undeformed fibre
                            ! vectors in local coordinate system (a,b,c)
    real, dimension(4)   :: rho     ! Normalised deformed fibre lengths
    real, dimension(4)   :: Beta_rho ! Inverse Langevin of the
                            ! normalised deformed fibre lengths
    real                 :: lambda_a ! Stretch along material axis a
    real                 :: lambda_b ! Stretch along material axis b
    real                 :: lambda_c ! Stretch along material axis c
    real, dimension(3,3) :: RCGT     ! Right Cauchy-Green Tensor
    real, dimension(3,3) :: dJdE     ! Slope of determinant wrt strain
    real, dimension(3,3) :: second_piola_kirchoff_stress  ! Second
                                    ! Piola Kirchoff stress Tensor
    real, dimension(3,3) :: kirchoff_stress ! Kirchoff stress Tensor
    real                 :: real_number
    real, dimension(1,3) :: real_array
    real, dimension(3,3) :: real_matrix
```

154

```fortran
real, dimension(1,3)  :: Pt
real                  :: Langevin_Inverse ! Function
real                  :: first_term
real                  :: second_term
real                  :: third_term
real, dimension(3,3)  :: dfgrd1_transpose ! Deformation gradient at
real, dimension(1,3)  :: avect            ! the start of the increment
real, dimension(1,3)  :: bvect
real, dimension(1,3)  :: cvect

! Set constant values
real, parameter :: k_boltz  = 1.3807e-29 ! Boltzman's constant
real, parameter :: theta    = 298.0      ! Temperature in kelvin
real, parameter :: smallnum = 1e-10

! Orientation of cell with respect to the material axes
real, parameter, dimension(3) :: avec = (/1.0, 0.0, 0.0/)
real, parameter, dimension(3) :: bvec = (/0.0, 1.0, 0.0/)
real, parameter, dimension(3) :: cvec = (/0.0, 0.0, 1.0/)

! Initialise variables
lambda_a    = 0.0
lambda_b    = 0.0
lambda_c    = 0.0
rho(:)      = 0.0
RCGT(:,:)   = 0.0
N_links     = (a**2 + b**2 + c**2) / 4.0
Pmag        = sqrt(N_links)
error       = .false.

P(:,1) = (/ a/2.0 * ( avec(1) + bvec(1) + cvec(1) ),     &
            b/2.0 * ( avec(2) + bvec(2) + cvec(2) ),     &
            c/2.0 * ( avec(3) + bvec(3) + cvec(3) ) /)
P(:,2) = (/ a/2.0 * ( avec(1) + bvec(1) + cvec(1) ),     &
            b/2.0 * ( avec(2) + bvec(2) + cvec(2) ),     &
           -c/2.0 * ( avec(3) + bvec(3) + cvec(3) ) /)
P(:,3) = (/ a/2.0 * ( avec(1) + bvec(1) + cvec(1) ),     &
           -b/2.0 * ( avec(2) + bvec(2) + cvec(2) ),     &
            c/2.0 * ( avec(3) + bvec(3) + cvec(3) ) /)
P(:,4) = (/ a/2.0 * ( avec(1) + bvec(1) + cvec(1) ),     &
           -b/2.0 * ( avec(2) + bvec(2) + cvec(2) ),     &
           -c/2.0 * ( avec(3) + bvec(3) + cvec(3) ) /)

call matrix_determinant(dfgrd1,DetF)
! Check determinant is real and non-zero

! Calculate Right Cauchy-Green Tensor C=F^T*F
call matrix_transpose(dfgrd1,dfgrd1_transpose,3,3)
call matrix_product(dfgrd1_transpose,dfgrd1,RCGT,3,3,3)

! Calculate stretch along the material axes
call matrix_transpose(avec,avect,3,1)
call matrix_product(avect,RCGT,real_array,1,3,3)
call matrix_product(real_array,avec,real_number,1,3,1)
lambda_a = sqrt(real_number)

call matrix_transpose(bvec,bvect,3,1)
call matrix_product(bvect,RCGT,real_array,1,3,3)
call matrix_product(real_array,bvec,real_number,1,3,1)
lambda_b = sqrt(real_number)
```

```
      call matrix_transpose(cvec,cvect,3,1)
      call matrix_product(cvect,RCGT,real_array,1,3,3)
      call matrix_product(real_array,cvec,real_number,1,3,1)
      lambda_c = sqrt(real_number)

      ! Calculate normalised undeformed fibre lengths, rho
      do i = 1, 4
         call matrix_transpose(P(:,i),Pt,3,1)
         call matrix_product(Pt,RCGT,real_array,1,3,3)
         call matrix_product(real_array,P(:,i),real_number,1,3,1)
         rho(i) = sqrt(real_number)
      end do

   ! Calculate Langevin inverse of normalised deformed fibre lengths,rho
      do i = 1, 4
         Beta_rho(i) = Langevin_Inverse(rho(i) / N_links)
         if (Beta_rho(i) == -999.0) then
            write(6,*) "Error in calculating the Langevin; rho(i), N_links",
   & rho(i), N_links
            error = .true.
            return
         end if
      end do

   ! Calculate Langevin inverse of normalised undeformed fibre lengths,
   rho
      Beta_P = Langevin_Inverse(Pmag / N_links)
      if (Beta_P == -999.0) then
         write(6,*) "Error in calculating the Langevin; Pmag, N_links",
   Pmag, N_links
         error = .true.
         return
      end if

      ! First precalculate dJ/dEjk
      dJdE(1,1)= ( RCGT(2,2) * RCGT(3,3) - RCGT(3,2) * RCGT(2,3) ) / DetF
      dJdE(1,2)= ( RCGT(3,1) * RCGT(2,3) - RCGT(2,1) * RCGT(3,3) ) / DetF
      dJdE(1,3)= ( RCGT(2,1) * RCGT(3,2) - RCGT(3,1) * RCGT(2,2) ) / DetF

      dJdE(2,1)= ( RCGT(3,2) * RCGT(1,3) - RCGT(1,2) * RCGT(3,3) ) / DetF
      dJdE(2,2)= ( RCGT(1,1) * RCGT(3,3) - RCGT(3,1) * RCGT(1,3) ) / DetF
      dJdE(2,3)= ( RCGT(3,1) * RCGT(1,2) - RCGT(1,1) * RCGT(3,2) ) / DetF

      dJdE(3,1)= ( RCGT(1,2) * RCGT(2,3) - RCGT(2,2) * RCGT(1,3) ) / DetF
      dJdE(3,2)= ( RCGT(2,1) * RCGT(1,3) - RCGT(1,1) * RCGT(2,3) ) / DetF
      dJdE(3,3)= ( RCGT(1,1) * RCGT(2,2) - RCGT(2,1) * RCGT(1,2) ) / DetF

      do j = 1, 3
        do k = 1, 3

          first_term = 0.0
          do i = 1, 4
            first_term= first_term + P(j,i)*P(k,i) / rho(i) * Beta_rho(i)
          end do

          second_term = Beta_P/Pmag*(a**2*avec(j)*avec(k)/lambda_a**2+  &
                                     b**2*bvec(j)*bvec(k)/lambda_b**2+  &
                                     c**2*cvec(j)*cvec(k)/lambda_c**2 )

          third_term = BM * sinh(detF - 1) * dJdE(j,k)
```

156

```fortran
      second_piola_kirchoff_stress(j,k) = n * k_boltz * theta/4.0 * &
                              ( first_term - second_term ) + third_term
    end do
  end do

  ! Calculate Cauchy Stress
  call
matrix_product(dfgrd1,second_piola_kirchoff_stress,real_matrix,3,3,3)
  call
matrix_product(real_matrix,dfgrd1_transpose,kirchoff_stress,3,3,3)
  cauchy_stress = 1.0 / detF * kirchoff_stress

end subroutine calculate_stress

! ****************************************************************

! Function to calculate the Inverse Langevin Function
real function Langevin_Inverse(x)
  implicit none

  ! Declare variables passed in to function
  real, intent(in) :: x

  real :: sign_x
  integer            :: i
  real, dimension(15) :: c
  real              :: sum
  logical            :: exact_form

  exact_form = .true.

  if ( exact_form ) then
    if ( abs(x) < 0.81436 ) then
      Langevin_Inverse = 1.31446 * tan(1.58986 * x) + 0.91209 * x
    else if ( abs(x) >= 0.81436 .and. abs(x) < 1.0 ) then
      sign_x = x / abs(x)
      langevin_inverse = 1.0 / (sign_x - x)
    else
      langevin_inverse = -999.0
    end if
  else
    c(1) = 3.0;
    c(2) = 1.8;
    c(3) = 1.697;
    c(4) = 1.759;
    c(5) = 1.872;
    c(6) = 1.997;
    c(7) = 2.113;
    c(8) = 2.202;
    c(9) = 2.253;
    c(10) = 2.256;
    c(11) = 2.206;
    c(12) = 2.106;
    c(13) = 1.964;
    c(14) = 1.796;
    c(15) = 1.625;

    sum = 0.0
    do i = 1, 15
      sum = sum + c(i) * x**(2.0*float(i)-1.0);
    end do
```

```fortran
    langevin_inverse = sum

  end if

end function Langevin_Inverse

! ****************************************************************

! Subroutine finds the product of A(m,n)*B(n,p) and returns C(m,p)
subroutine matrix_product(A,B,C,m,n,p)
  implicit none

  ! Declare variables passed into this routine
  integer, intent(in)                    :: m
  integer, intent(in)                    :: n
  integer, intent(in)                    :: p
  real, intent(in),  dimension(m,n) :: A
  real, intent(in),  dimension(n,p) :: B
  real, intent(out), dimension(m,p) :: C

  ! Declare variables that originate in this routine
  integer :: i
  integer :: j
  integer :: k

  ! Initialise variables
  C(:,:) = 0.0

  do k = 1, p
    do i = 1, m
      do j = 1, n
        C(i,k) = C(i,k) + A(i,j) * B(j,k)
      end do
    end do
  end do

end subroutine matrix_product

! ****************************************************************

! Subroutine finds the transpose of a matrix A(m,n) and returns B(n,m)
subroutine matrix_transpose(A,B,m,n)
  implicit none

  ! Declare variables passed into this routine
  integer, intent(in) :: m
  integer, intent(in) :: n
  real, intent(in),  dimension(m,n)  :: A
  real, intent(out), dimension(n,m) :: B

  ! Declare variables that originate in this routine
  integer :: i
  integer :: j

  ! Initialise variables
  B(:,:) = 0.0

  do i = 1, m
    do j = 1, n
      B(j,i) = A(i,j)
```

```fortran
      end do
    end do

  end subroutine matrix_transpose

  ! ***************************************************************

  ! Subroutine finds the determinant of a matrix A(3,3)
  subroutine matrix_determinant(A,determinant)
    implicit none

    ! Declare variables passed into this routine
    real, intent(in), dimension(3,3) :: A
    real, intent(out)                :: determinant

    ! Initialise variables
    determinant = 0.0

    determinant = A(1,1) * ( A(2,2) * A(3,3) - A(2,3) * A(3,2) ) - &
                  A(1,2) * ( A(2,1) * A(3,3) - A(2,3) * A(3,1) ) + &
                  A(1,3) * ( A(2,1) * A(3,2) - A(2,2) * A(3,1) )

  end subroutine matrix_determinant

  ! ***************************************************************

  ! Subroutine finds the inverse of a matrix A(3,3)
  subroutine matrix_inverse(A,inverse)
    implicit none

    ! Declare variables passed into this routine
    real, intent(in), dimension(3,3)  :: A
    real, intent(out), dimension(3,3) :: inverse

    ! Declare variables originating in this routine
    real :: determinant

    ! Initialise variables
    determinant  = 0.0
    inverse(:,:) = 0.0

    call matrix_determinant(A,determinant)

    inverse(1,1) = A(2,2) * A(3,3) - A(2,3) * A(3,2)
    inverse(1,2) = A(1,3) * A(3,2) - A(1,2) * A(3,3)
    inverse(1,3) = A(1,2) * A(2,3) - A(2,2) * A(1,3)

    inverse(2,1) = A(2,3) * A(3,1) - A(2,1) * A(3,3)
    inverse(2,2) = A(1,1) * A(3,3) - A(1,3) * A(3,1)
    inverse(2,3) = A(1,3) * A(2,1) - A(2,3) * A(1,1)

    inverse(3,1) = A(2,1) * A(3,2) - A(2,2) * A(3,1)
    inverse(3,2) = A(1,2) * A(3,1) - A(1,1) * A(3,2)
    inverse(3,3) = A(1,1) * A(2,2) - A(2,1) * A(1,2)

    inverse(:,:) = 1.0 / determinant * inverse(:,:)

  end subroutine matrix_inverse
```

Appendix D

The Nelder-Mead Method

The Nelder-Mead method is an algorithm for finding the minimum of a function of several variables (Mathews and Kink, 2004). It operates by computing the values of the function at each vertex of a simplex. The vertices are compared and the one with the largest function value is discarded and a new vertex is found. A simplex is a generalised triangle in N-dimensions. For a two dimensional function, the simplex is a triangle; for a three-dimensional function, the simplex is a tetrahedron and so on.

To illustrate the algorithm, consider a function $f(x,y)$ whose location of minimum is to be found.

The algorithm commences with a simplex of three vertices V_1, V_2 and V_3. The function is evaluated at each of the three vertices and their values compared. The vertex with the lowest value is labelled B; the next lowest G; and the vertex with the highest function value W. The latter is the worst vertex and needs to be replaced with a new vertex. This is done by following one or more of the following actions:

Reflection

Firstly, the mid-point of the line segment between B and G is found – this is labelled M. The line segment between W and M is reflected through BG to get a new vertex R as seen in Figure D.1. The function is evaluated at R and if it is lower than the value at W then the vertices are moving in the correct direction towards the minimum.

Extension

Next it is investigated whether the minimum is further along the line segment MR by extending it to E such that R is the midpoint of ME (Figure D.2). If the function value at E is lower than at R then the triangle BGE is better than BGR.
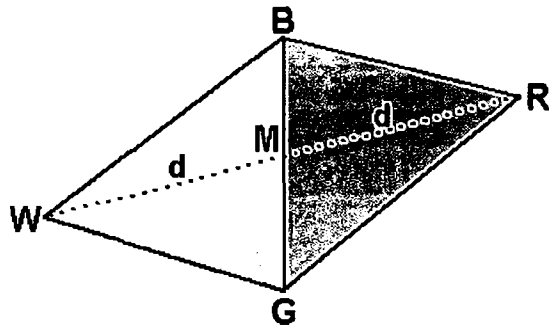
160

Figure D.1: Reflection: A new vertex **R** is found by reflecting **WM** through **BG**
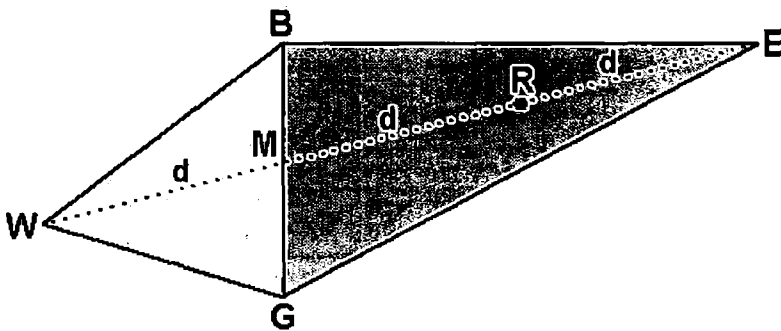

Figure D.2: Extension: The point **E** is found by extending **MR** a distance **d**. The function value at **E** is compared with the function value at **R** – if it is lower then **E** is an improved vertex over **R**

Contraction

If the function value at **R** was greater than at **W**, another action is needed to find a new vertex. The mid-points of the line-segments **WM** and **MR** (**C1** and **C2**) are found and the function values at each are calculated and compared (Figure D.3). The mid-point with the lower value forms the new vertex of the triangle.

Shrinking of the triangle

If neither function value at the mid-points is lower than at **W**, then the triangle **BGW** is shrunk by moving both **G** and **W** towards **B**. The point **G** is replaced by **M** and **W** is replaced by **S**, which is the midpoint of the line segment between **B** and **W** (Figure D.4).

When a new vertex is found and a new triangle formed, the iteration is complete and a new one begins. The iterations are repeated until the location of the function minimum is found within specified tolerances. Figure D.5 shows the vertices of the
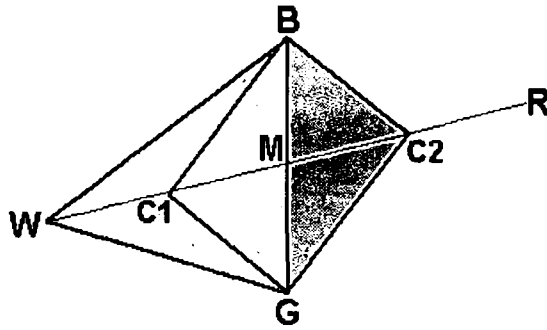
Figure D.3: Contraction: **C1** and **C2** are the mid-points of **WM** and **MR**. If the function value at **C1** is lower than the function value at **C2** then the new triangle is **BGC1**. Otherwise, the new triangle is **BGC2**.
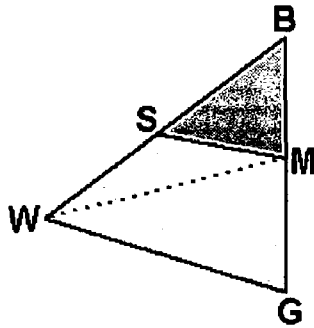

Figure D.4: Shrinkage: A new triangle is formed by replacing **G** with **M** and **W** with **S**, which is the mid-point of **BW**.
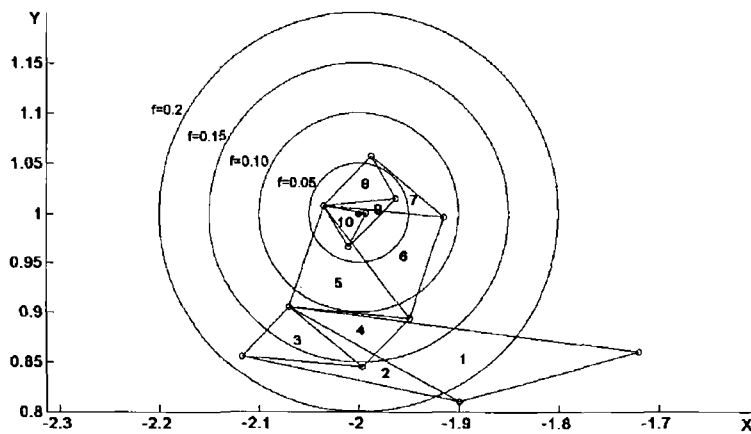

Figure D.5: The sequence of triangles converging to the point (-2, 1), which is the location of the minimum of $f(x, y) = (x + 2)^2 + (y - 1)^2$.

triangles after each iteration of the Nelder-Mead method when searching for the location of the minimum of the function $f(x, y) = (x + 2)^2 + (y - 1)^2$. The triangles converge on the point (-2, 1).

162

Appendix E

Load boundary condition problems

It was mentioned in Section 4.2.2, when modelling the wrinkling of skin between the displaced tabs that it was not possible to place a load boundary condition in the Z-direction along the length of the model indicated in Figure E.1.

During the second step when a load was applied along the length of the model and the tab was being displaced, the analysis would fail before any wrinkling occurred. Error messages indicated that, for an element in the dermal layer, the ratio of the normalised deformed fibre length to the number of freely joined rigid links was greater than one, i.e. $\rho/N > 1$. The inverse Langevin function is undefined for values greater than one so the analysis failed. To investigate the problem further, an Ogden model was substituted in place of the orthotropic-viscoelastic model to represent the dermis. This was done in order to determine whether the cause of the analysis failure
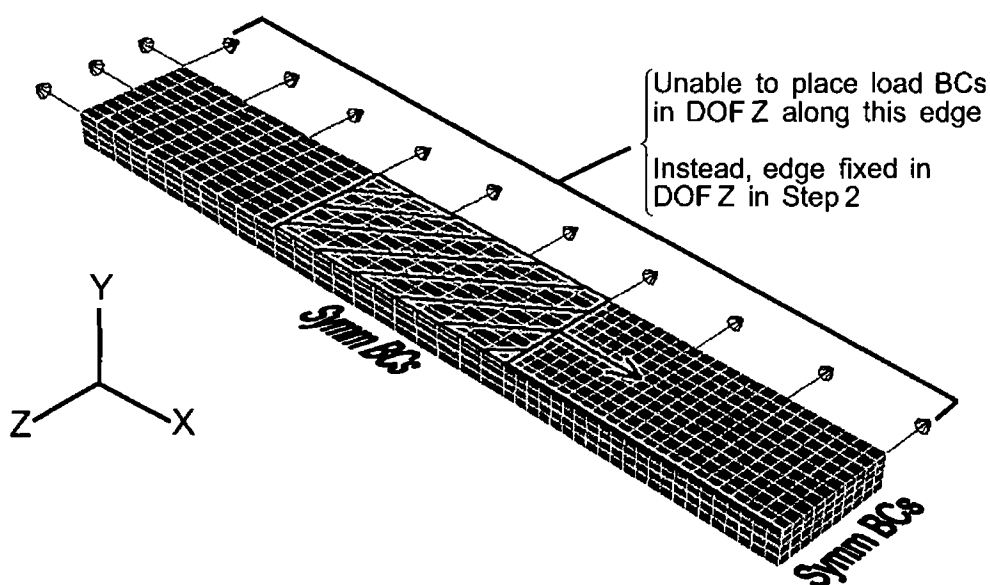

Figure E.1: Applying boundary conditions along the edge of the finite element model

was due to the orthotropic-viscoelastic model. With the Ogden model in place, the analysis failed at a similar point. Error messages indicated the stability limit was exceeded and so the solution became numerically unstable. The problem, therefore, was not solely due to the orthotropic-viscoelastic model. Fixing certain rotational degrees of freedom on the edge of the stratum corneum layer improved things slightly. The analysis ran further than before but still failed before any wrinkling occurred.

The difficulties were possibly due to the large stress difference between the stratum corneum and the dermal layers. While the stress in the dermis was 2 kPa, the stress in the stratum corneum varied between 10 and 65 MPa depending on its relative humidity. The problem may disappear if a larger model is considered so that the boundary conditions are removed from the zone of wrinkling as shown in Figure E.2. Unfortunately, time and resource constraints prevent larger models from being run.

The solution taken, as detailed in Section 4.4.2, was to stretch the skin in the first step to apply the pre-tension and, in the second step, fix the long edge of the model from moving in the Z-direction. It was desirable to find out how much of a difference fixing the edge of the model had on the maximum range and roughness of the wrinkles compared to applying a load boundary condition along the edge. Two three-layer models were run with no pre-tension applied in either of them. In one model, no
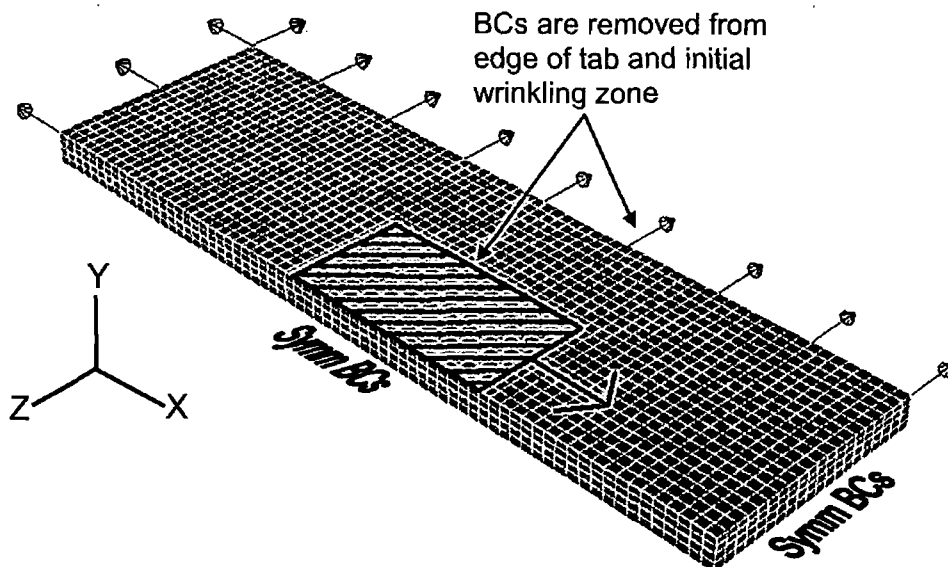

Figure E.2: Possible solution to problem - Finite element model extended in width so that the boundary conditions along the edge are removed from the edge of the tab and initial wrinkling zone

164

boundary conditions were placed on the long edge in the Z-direction. In the other model, the long edge was fixed in the Z-direction. The tabs were displaced in both models and the maximum range and average roughness calculated in the usual manner. The results of both models are shown in Figure E.3(a) and Figure E.3(b). The maximum ranges predicted by both models were very similar up to tab displacements of 2.5 mm. Thereafter, the maximum range predicted by the model with the fixed edge was higher than the maximum range predicted by the model with the free edge (9% higher at a tab displacement of 3.5 mm). This trend was expected. As the tabs displaced, the skin in between was compressed. In the model with no boundary conditions in the Z-direction on the long edge the material was free to displace in the Z-direction as well as the Y-direction. In the model with the long edge fixed in the Z-direction, the material was only free to displace in the vertical direction and so the maximum ranges were higher. The average roughness predicted by both models was very similar.

To summarise, Figure E.3 shows the differences in the maximum range and average roughness between two zero-pre-tensioned models – one with no boundary condition in the Z-direction applied along the edge and the other with its edge fixed in the Z-direction. It is assumed that similar differences would be observed between pre-tensioned models that have load boundary conditions applied in the Z-direction along the edge and pre-tensioned models with their edges fixed in the Z-direction. Future work will be focussed on overcoming the numerical problems discussed in this section.
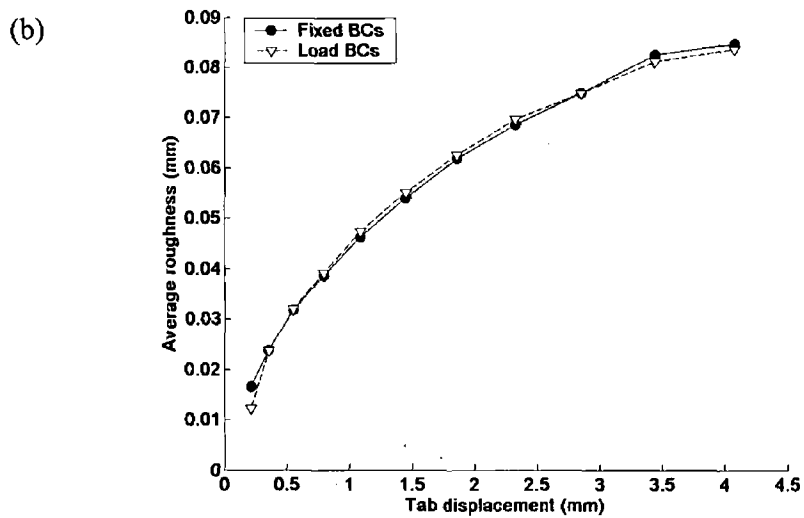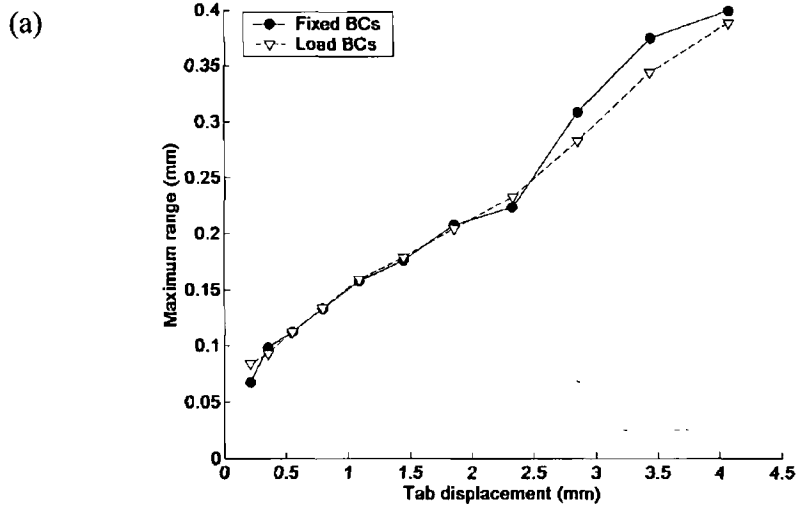
(a)

(b)

Figure E.3: Comparing the maximum range and average roughness of the wrinkles formed when the a load boundary condition was placed along the side of the model and when a the side was fixed in position. There was no pre-tension in the model before the tabs were displaced.

166